JETP Letters, Vol. 79, No. 6, 2004, pp. 241–244. Translated from Pis'ma v Zhurnal Éksperimental'noĭ i Teoreticheskoĭ Fiziki, Vol. 79, No. 6, 2004, pp. 299–302.

Formation of the 255-keV Annihilation Line near the Magnetic Poles of Pulsars

V. M. Kontorovich[1, 2] and A. B. Flanchik[2]

[1] *Institute of Radio Astronomy, National Academy of Sciences of Ukraine, Kharkov, 61002 Ukraine*

[2] *Kharkov State University, Kharkov, 61077 Ukraine*

Received December 22, 2003; in final form, February 17, 2004

The possibility of existance is discussed for pulsars emitting soft γ radiation near their magnetic poles upon the annihilation of ultrarelativistic positrons from the magnetosphere and electrons from the surface of a star. With an increase in the energy of incident positrons, the photon energy of this backward radiation tends to a constant value $m_e c^2/2 = 255$ keV. This radiation is shown to be directed opposite to the positron flux direction. © *2004 MAIK "Nauka/Interperiodica".*

PACS numbers: 97.60.Gb; 97.10.Ld; 98.70.Rz

1. A pulsar is a source of electromagnetic radiation over a wide range from radio waves to hard γ radiation up to a photon energy of 10^8 MeV. As is known, γ rays can be emitted due to both ultrarelativistic electrons and positrons moving in a strong magnetic field and various collision processes between charged particles. In the former and latter cases, this radiation is called bend radiation and collisional bremsstrahlung, respectively. In this work, we analyze the possibility of generating soft γ radiation caused by the annihilation line formed due to the annihilation of ultrarelativistic positrons from the magnetosphere and electrons from the pulsar surface. Since the electron velocities in the pulsar surface are much lower than the speed of light, we consider electrons to be at rest. As is known [1], charged particles in the pulsar magnetosphere move along magnetic lines of force, because the motion in the plane perpendicular to the magnetic field rapidly becomes impossible due to synchrotron radiation. Positrons can be accelerated in the pulsar magnetosphere by an electric field. However, this acceleration is not possible over the entire magnetosphere, because, in plasma-filled regions rotating with the pulsar, the condition $\mathbf{E} \cdot \mathbf{B} = 0$ for electric **E** and magnetic **B** fields is fulfield [2]. Positrons are accelerated toward the pulsar surface in a gap, i.e., in the region over the magnetic pole of the pulsar, where $\mathbf{E} \cdot \mathbf{B} \neq 0$ and an electric field directed along the magnetic field exists. In this work, the electric field of the pulsar is treated in the Arons model [3, 4]. In this model, the longitudinal electric field in the gap is represented in the form

$$E_\parallel(h) = \frac{1}{2}A(h^2 - Hh), \qquad (1)$$

and, with allowance for the general-relativity effects, the coefficient A is given by the formula [5, 6]

$$A = \frac{3}{2}\frac{\Omega B_0}{cR}\left(4\frac{\omega}{\Omega}\cos\alpha + \varepsilon_0\cos\phi_m\sin\alpha\right). \qquad (2)$$

Here, $h < H$ is the altitude over the pulsar surface, H is the gap altitude determined by the condition for generating the secondary component of e^-e^+ plasma, Ω is the angular velocity of the pulsar, R is the pulsar radius, B_0 is the magnetic field at the pulsar surface, $\varepsilon_0 = \sqrt{\Omega R/c}$ is the pulsar geometric factor, α is the angle between the magnetic and rotation axes, $\omega = \Omega R_g^3/r^3$, and ϕ_m is the azimuth angle measured from the direction of the northern magnetic semiaxis of the pulsar. The mechanism considered for generating γ radiation can be realized only if $E_\parallel < 0$. According to Eq. (2), there are magnetic lines of force on which the inequality $E_\parallel < 0$ is satisfied. Such lines were previously called preferable. Since the second term in Eq. (2) is small, preferable lines are most magnetic lines of force on which positrons moving along them are accelerated by field (1) toward the pulsar surface.

The mechanism of forming the 255-keV annihilation line is shown in the figure. When moving along the magnetic lines of force, ultrarelativistic positrons from the magnetosphere are incident on the pulsar surface, and γ radiation arises due to their annihilation with electrons. Radiation in the direction of positron motion, i.e., forward radiation, carries almost the entire positron energy to the pulsar interior, and a soft backward γ radiation with an energy of 255 keV is emitted opposite to the positron beam. The spectrum and angular distribution of this radiation will be discussed below.

2. The formation of the annihilation line is primarily determined by the two- and three-photon electron–

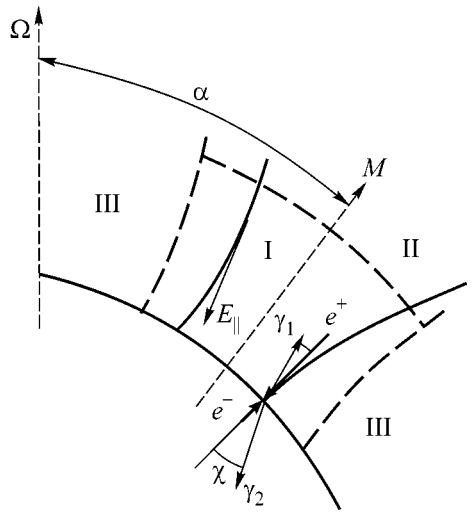

Mechanism of the formation of annihilation line: I is the gap region, where $E_\parallel \neq 0$; II is the region of open field lines, where $E_\parallel = 0$; and III is the corotation region. The annihilation of a positron from the pulsar magnetosphere and a surface electron is accompanied by the backward emission of the 255-keV line.

positron annihilation events. In this work, three-photon annihilation affecting the width and wings of the annihilation line [7] is disregarded.

Let us consider the two-photon annihilation kinematics in the laboratory frame, where an electron is at rest. We use the standard kinematic invariants [8]

$$\begin{aligned} s &= (p_- - k_1)^2 = (k_2 - p_+)^2, \\ t &= (p_- + p_+)^2 = (k_1 + k_2)^2, \\ u &= (p_- - k_2)^2 = (k_1 - p_+)^2, \end{aligned} \tag{3}$$

where p_-, p_+, k_1, and k_2 are the 4-momenta of the electron, positron, and annihilation photons, respectively. Let us express the frequencies of annihilation photons through the angle χ between the direction of positron motion and the photon 3-momentum $\mathbf{k}_2$ (figure). In the laboratory frame, the electron and positron have 4-momenta $p_- = (m, 0)$ and $p_+ = (\varepsilon_+, \mathbf{p}_+)$, respectively. Therefore, from Eqs. (3) and the 4-momentum conservation law $p_- + p_+ = k_1 + k_2$, we obtain

$$\begin{aligned} s &= (p_- - k_1)^2 = (k_2 - p_+)^2, \\ m^2 - 2m\omega_1 &= m^2 - 2p_+k_2, \end{aligned} \tag{4}$$

$$m\omega_1 = \varepsilon_+\omega_2 - |\mathbf{p}_+|\omega_2\cos\chi = \omega_2(\varepsilon_+ - |\mathbf{p}_+|\cos\chi).$$

From these relations, the desired energies of annihilation photons are expressed as

$$\begin{aligned} \omega_1 &= (\varepsilon_+ + m)\frac{\varepsilon_+ - |\mathbf{p}_+|\cos\chi}{\varepsilon_+ + m - |\mathbf{p}_+|\cos\chi}, \\ \omega_2 &= \frac{m(\varepsilon_+ + m)}{\varepsilon_+ + m - |\mathbf{p}_+|\cos\chi}. \end{aligned} \tag{5}$$

3. Photon energies (5) are functions of two parameters: the energy of an incident positron and the emission angle χ. To determine the angular distribution of annihilation photons, we use the following general formula for the differential cross section for two-photon annihilation [8]:

$$\begin{aligned} \frac{d\sigma}{ds} &= \frac{8\pi r_e^2 m^2}{t(t-4m)^2}\left\{\left(\frac{m^2}{s-m^2} + \frac{m^2}{u-m^2}\right)^2\right. \\ &\left. + \left(\frac{m^2}{s-m^2} + \frac{m^2}{u-m^2}\right) - \frac{1}{4}\left(\frac{s-m^2}{u-m^2} + \frac{u-m^2}{s-m^2}\right)\right\}, \end{aligned} \tag{6}$$

where s, t, and u are the standard kinematic invariants given by Eqs. (3) and r_e is the classical electron radius. Let us calculate expression (6) in the laboratory frame, where the electron is at rest. Using the expressions $t = 2m(m + \varepsilon_+)$ and $u - m^2 = -2m\omega_2$ and differentiating the expression $s - m^2 = -2\omega_2(\varepsilon_+ - |\mathbf{p}_+|\cos\chi)$, we obtain

$$\begin{aligned} ds &= -2d\omega_2(\varepsilon_+ - |\mathbf{p}_+|\cos\chi) + 2\omega_2|\mathbf{p}_+|d\cos\chi \\ &= 2\left(\omega_2|\mathbf{p}_+| - \frac{\partial\omega_2}{\partial\cos\chi}(\varepsilon_+ - |\mathbf{p}_+|\cos\chi)\right)d\cos\chi \\ &= -|\mathbf{p}_+|\left(\frac{m(\varepsilon_+ + m)}{\varepsilon_+ + m - |\mathbf{p}_+|\cos\chi}\right. \\ &\left. - \frac{m(\varepsilon_+ + m)(\varepsilon_+ - |\mathbf{p}_+|\cos\chi)}{(\varepsilon_+ + m - |\mathbf{p}_+|\cos\chi)^2}\right)\frac{do}{\pi}, \\ do &= 2\pi\sin\chi d\chi. \end{aligned} \tag{7}$$

Substitution of Eq. (7) into general expression (6) gives

$$d\sigma = \frac{r_e^2 G(\varepsilon_+, \chi)}{2|\mathbf{p}_+|}F(\varepsilon_+, \chi)do, \tag{8}$$

where

$$\begin{aligned} G(\varepsilon_+, \chi) &= \frac{m(\varepsilon_+ + m)}{\varepsilon_+ + m - |\mathbf{p}_+|\cos\chi} \\ &- \frac{m(\varepsilon_+ + m)(\varepsilon_+ - |\mathbf{p}_+|\cos\chi),}{[(\varepsilon_+ + m) - |\mathbf{p}_+|\cos\chi]^2} \\ F(\varepsilon_+, m) &= \frac{\varepsilon_+ - |\mathbf{p}_+|\cos\chi}{m} + \frac{m}{\varepsilon_+ - |\mathbf{p}_+|\cos\chi} \end{aligned} \tag{9}$$

$$+\frac{2m^2}{\omega_2}\left(\frac{1}{m}+\frac{1}{\varepsilon_+-|\mathbf{p}_+|\cos\chi}\right)$$

$$-\frac{m^4}{\omega_2^2}\left(\frac{1}{m}+\frac{1}{\varepsilon_+-|\mathbf{p}_+|\cos\chi}\right)^2.$$

Since the denominators in expressions (9) contain $\varepsilon_+ + m - |\mathbf{p}_+|\cos\chi$ and $\varepsilon_+ - |\mathbf{p}_+|\cos\chi$, cross section (8) is nonzero only for small angles χ. This property is a manifestation of the general property (relativistic aberration) of radiation from an ultrarelativistic particle [9]. Almost the entire positron energy is emitted along its direction of motion. It follows from Eqs. (9) that there are two small-angle regions: the region $\chi < m/\varepsilon_+$, where $m/(\varepsilon_+ - |\mathbf{p}_+|\cos\chi) \gg 1$, and the region $\chi < \sqrt{m/\varepsilon_+}$, where $m/(\varepsilon_+ + m - |\mathbf{p}_+|\cos\chi) \gg 1$.

(i) In the region $\chi < m/\varepsilon_+$, the product

$$G(\varepsilon_+, \chi)F(\varepsilon_+, \chi) = m\left(\frac{m^2}{2\varepsilon_+^2}+\frac{\chi^2}{2}\right)^{-1} \quad (10)$$

increases with an increase in the positron energy.

(ii) In the region $m/\varepsilon_+ < \chi < \sqrt{m/\varepsilon_+}$, Eqs. (9) take the form

$$G(\varepsilon_+, \chi) = \frac{m}{1+\varepsilon_+\chi^2/2m}, \quad F(\varepsilon_+, \chi) = \frac{2m}{\varepsilon_+\chi^2}. \quad (11)$$

An increase in the product GF stops due to a decrease in the quantity $m/(\varepsilon_+ - |\mathbf{p}_+|\cos\chi)$ for these angles.

4. Taking into account the expression obtained for the angular distribution, we now analyze expressions (5) for the energies of annihilation photons in the high-energy limit. For $\chi \le m/\varepsilon_+$, one can set $\chi = 0$ in expressions (5). For $\varepsilon_+ \gg m$, the energy in this case takes the limiting value

$$\omega_1 = \frac{m}{2} = 255 \text{ keV} \quad (12)$$

and the asymptotic value is

$$\omega_2 \approx \varepsilon_+. \quad (13)$$

In the angular region $m/\varepsilon_+ < \chi \le \sqrt{m/\varepsilon_+}$, we retain contributions $\sim\chi^2$ in the expansions of expressions (5) and obtain the photons energies in the form

$$\omega_1 = \frac{\varepsilon_+^2\chi^2}{2m+\varepsilon_+\chi^2}, \quad \omega_2 = \frac{\varepsilon_+}{1+\varepsilon_+\chi^2/2m}. \quad (14)$$

According to Eqs. (12) and (13), photons with energies ω_1 form the 255-keV annihilation line and γ-ray photons with energy ω_2 have continuous energy spectrum reflecting the positron energy spectrum. The existence of a limiting energy of 255 keV in the process under consideration is the basic result of this work. Photons with an energy of 255 keV are emitted opposite to the positron beam incident on the surface. Indeed, as was mentioned above, a photon with momentum $\mathbf{k}_2$ is emitted at a small angle to the direction of positron motion. Let us calculate the angle ϕ between the momenta of annihilation photons. From the relation $t = 2m(m + \varepsilon_+) = 2k_1k_2 = 2\omega_1\omega_2(1 - \cos\phi)$, we obtain

$$\cos\phi = 1-\frac{m(m+\varepsilon_+)}{\omega_1\omega_2}. \quad (15)$$

In view of limiting expressions (12)–(14), formula (15) yields

$$\cos\phi = \begin{cases} -1, & \chi \le m/\varepsilon_+, \\ 1-2\dfrac{m^2}{\varepsilon_+^2\chi^2}-\dfrac{2m}{\varepsilon_+}-\dfrac{\chi^2}{2}, & \dfrac{m}{\varepsilon_+} < \chi \le \sqrt{\dfrac{m}{\varepsilon_+}}. \end{cases} \quad (16)$$

The limiting value of $\cos\phi$ for $\chi \longrightarrow 0$ is equal to –1; i.e., photons move in the opposite directions. Therefore, the annihilation line is emitted backward, i.e., opposite to the positron beam.

5. The intensity of the 255-keV annihilation line is estimated by expressing it through the quantities referring to the positron component of plasma. To this end, we consider a monoenergetic positron beam incident with energy ε_+ on the pulsar surface. The probability of positron capture per unit time is $dw(\varepsilon_+, t) = j(\varepsilon_+, t)d\sigma_{\gamma\gamma}$, where $j(\varepsilon_+, t)$ is the flux density of positrons with energy ε_+ and $d\sigma_{\gamma\gamma}$ is the cross section for two-photon annihilation given by Eq. (8). Multiplying the probability $dw(\varepsilon_+, t)$ by the photon energy $\omega_1(\varepsilon_+, \chi)$ and the number of electrons N_e, we obtain the intensity dI of 255-keV line radiation in the form

$$dI = N_e\omega_1(\varepsilon_+, \chi)j(\varepsilon_+, t)\frac{d\sigma_{\gamma\gamma}}{do}do. \quad (17)$$

Integrating this expression with respect to the angles, one obtains the total intensity of annihilation line. We take into account only the contribution from the region $\chi < m/\varepsilon_+$. According to Eq. (12), $\omega_1(\varepsilon_+, \chi) = m/2$. Then, the integration of Eq. (17) with respect to the angles yields

$$I(\varepsilon_+, t) = \frac{m}{2}N_e j(\varepsilon_+, t)\sigma_{\gamma\gamma}(\varepsilon_+), \quad (18)$$

where $\sigma_{\gamma\gamma}$ is the total cross section for two-photon annihilation. The total intensity of annihilation line is obtained by summing contributions (18) over the entire energy spectrum of positrons. Therefore,

$$I^{(\text{tot})}(t) = \frac{N_e m}{2}\int_{\varepsilon_{\min}}^{\infty} f(\varepsilon_+, t)j(\varepsilon_+, t)\sigma_{\gamma\gamma}(\varepsilon_+)d\varepsilon_+, \quad (19)$$

where $\varepsilon_{\min}$ is the lower limit of the positron energy spectrum and $f(\varepsilon_+, t)$ is the positron energy distribution

function. We treat N_e in Eqs. (18) and (19) as the number of electrons in a layer from which γ radiation can be emitted outside. Therefore, $N_e \sim n_e SL$, where n_e is the electron density in the pulsar surface, S is the area of annihilation region, and $L \sim 1/\mu$ is the thickness of this layer, where $\mu \sim \sigma_C n_e$ is the scattering coefficient of γ radiation per unit length (σ_C is the Compton scattering cross section). Therefore, $N_e \sim S/\sigma_C$. The intensity of the 255-keV annihilation line is preliminarily estimated as follows. Let us take the positron flux density in the form $j(\varepsilon_+, t) \sim \xi J_{GJ}$, where $J_{GJ} = \Omega B/2\pi e$ is the Goldreich–Julian density and ξ is a certain dimensionless parameter. The cross section σ_C is estimated as the Thompson cross section $\sigma_T \sim 10^{-26}$ cm^2. In this case, the intensity of 255-keV radiation arising upon the annihilation of a positron beam with energy ε_+ for a pulsar with rotation frequency $\Omega \sim 1$ Hz is equal to $I(\varepsilon_+) \sim \xi \frac{m}{\varepsilon_+} \times 10^{20}$ erg/s. This estimate is obtained without regard for the absorption and scattering of γ radiation in the pulsar magnetosphere.

6. In this work, we predict the possibility of forming the 255-keV annihilation line in the γ spectrum of a pulsar. As was shown above, this line arises due to the annihilation of ultrarelativistic positrons and surface electrons. Annihilation-induced γ radiation must be characterized by a sharply anisotropic angular distribution. High-energy γ-ray photons carry almost the entire energy of positrons to the pulsar interior. However, soft γ radiation from the surface must be observed. For high energies of incident positrons, the photon energy of this radiation approaches 255 keV. Analysis of this line provides important information about the gap structure and processes of particle acceleration in the gap. The annihilation line under consideration must undergo a large (about 20%) gravitational redshift (see, e.g., [10]), which can provide valuable information about the relation between the masses and radii of neutron stars. The effect of suppressing the annihilation line by a strong magnetic field [11] weakens significantly in this case, because the suppression effect is absent for photons propagating along the magnetic field and is very weak for photons propagating at small angles to the field.

We are grateful to V.S. Beskin, B.M. Morozhenko, and the referee for stimulating discussions.

REFERENCES

1. V. S. Beskin, Usp. Fiz. Nauk **169**, 1169 (1999) [Phys. Usp. **42**, 1071 (1999)].
2. P. Goldreich and W. H. Julian, Astrophys. J. **157**, 869 (1969).
3. J. Arons and E. T. Scharlemann, Astrophys. J. **231**, 854 (1979).
4. E. T. Scharlemann, W. M. Fawley, and J. Arons, Astrophys. J. **222**, 297 (1978).
5. V. S. Beskin, Pis'ma Astron. Zh. **16**, 665 (1990) [Sov. Astron. Lett. **16**, 286 (1990)].
6. A. G. Muslimov and A. I. Tsygan, Astron. Zh. **67**, 263 (1990) [Sov. Astron. **34**, 133 (1990)].
7. Yung-Su Tsai, Phys. Rev. **137**, B730 (1965).
8. V. B. Berestetskiĭ, E. M. Lifshitz, and L. P. Pitaevskiĭ, *Quantum Electrodynamics*, 2nd ed. (Nauka, Moscow, 1979; Pergamon Press, Oxford, 1982).
9. L. D. Landau and E. M. Lifshitz, *The Classical Theory of Fields*, 6th ed. (Nauka, Moscow, 1979; Pergamon Press, Oxford, 1975).
10. M. P. Ulmer, S. M. Matz, J. E. Grove, *et al.*, Astrophys. J. **551**, 244 (2001).
11. M. G. Baring, Mon. Not. R. Astron. Soc. **262**, 20 (1993).

Translated by R. Tyapaev

JETP Letters, Vol. 79, No. 6, 2004, pp. 245–248. From Pis'ma v Zhurnal Éksperimental'noĭ i Teoreticheskoĭ Fiziki, Vol. 79, No. 6, 2004, pp. 303–306.

On Projection (In)dependence of the Dual Superconductor Mechanism of Confinement¶

V. A. Belavin, M. N. Chernodub*, and M. I. Polikarpov

Institute of Theoretical and Experimental Physics, Moscow, 117259 Russia

**e-mail: Maxim.Chernodub@itep.ru*

Received January 29, 2004; in final form, February 19, 2004

We study the temperature dependence of the monopole condensate in different Abelian projections of the $SU(2)$ gauge theory on the lattice. Using the Fröhlich–Marchetti monopole creation operator, we show numerically that the monopole condensate depends on the choice of the Abelian projection. © *2004 MAIK "Nauka/Interperiodica".*

PACS numbers: 12.38.Gc; 11.15.Ha

The confinement of color in QCD is one of the most interesting issues in the modern quantum field theory. Numerical simulations of non-Abelian gauge theories on the lattice show [1] that the confinement of quarks happens due to the formation of the chromoelectric strings spanning between quarks and antiquarks. Although an analytical derivation of the color confinement is not available, the physical reason of the emergence of the string seems to be known. According to the dual superconductor model [2], the vacuum of a non-Abelian gauge model may be regarded as media of condensed Abelian monopoles. The monopole condensate squeezes the chromoelectric flux (coming from the quarks) into a flux tube due to the dual Meissner effect. This flux tube is an analogue of the Abrikosov vortex in an ordinary superconductor.

The basic element of the dual superconductor is the Abelian monopole. This object does not exist on the classical level in QCD, but it can be identified with a particular configuration of the gluon fields with the help of the so-called Abelian projection [3]. The Abelian projection uses a partial gauge fixing of the $SU(N)$ gauge symmetry up to an Abelian subgroup. In the Abelian projection, the Abelian monopoles appear naturally due to compactness of the residual Abelian group.

Many numerical simulations show that the Abelian degrees of freedom in an Abelian projection are likely to be responsible for the confinement of quarks (for a review, see, e.g., [4]). For example [5], the Abelian gauge fields provide a dominant contribution to the tension of the fundamental chromoelectric string ("Abelian dominance"). Moreover, the internal structure of the string energy, such as energy profile and the field distribution, are described very well by the dual superconductor model [1].

Since the qualitative features of the confinement mechanism in the real QCD with the $SU(3)$ gauge group and in the $SU(2)$ gauge theory are the same, in this letter, we restrict ourselves to the simplest case of the $SU(2)$ gluodynamics. The most convincing results supporting the dual superconductor scenario were obtained in the so-called maximal Abelian (MA) projection [6]. This gauge is defined by the maximization of the lattice functional (σ_i are the Pauli matrices),

$$\max_{\Omega} R_{MA}[U^{\Omega}],$$
$$R_{MA}[U] = \sum_{s,\tilde{\mu}} \mathrm{Tr}(\sigma_3 U(s,\mu)\sigma_3 U^{\dagger}(s,\mu)), \quad (1)$$

with respect to the gauge transformations, $U(s,\mu) \longrightarrow U^{\Omega}(s,\mu) = \Omega(s)U(s,\mu)\Omega^{\dagger}(s+\hat{\mu})$. In the continuum limit, condition (1) corresponds to the minimization of the functional $\int d^4x((A^1_\mu)^2 + (A^2_\mu)^2)$. A local condition of the MA gauge can be written in the form of a differential equation, $(\partial_\mu + igA^3_\mu)(A^1_\mu - iA^2_\mu) = 0$, which is invariant under the residual $U(1)$ gauge transformations, $\Omega^{\mathrm{Abel}}(\omega) = \mathrm{diag}(e^{i\omega}, e^{-i\omega})$, where ω is an arbitrary scalar function.

The MA gauge is a good candidate for a realization of the dual superconductor scenario because the MA gauge makes the off-diagonal gluon fields as small as possible, reducing their role. Thus, the Abelian dominance [5] is a natural effect in the MA gauge. According to numerical simulations [7–9], the monopole condensate in the MA gauge is formed in the low-temperature (confinement) phase and it disappears in the high-temperature (deconfinement) phase, in perfect agreement with the dual superconductor scenario.

Besides the MA gauge, there are also various gauges which are defined by a diagonalization of certain $SU(2)$

¶ This article was submitted by the authors in English.

functionals $X[U]$ with respect to the gauge transformations

$$X_x[U] \longrightarrow X_x[U^{(\Omega)}] \equiv \Omega^\dagger X_x[U]\Omega = \mathrm{diag}(\lambda_1, \lambda_2). \quad (2)$$

To define an Abelian gauge, the functional $X[U]$ must transform into an adjoint representation of the $SU(2)$ gauge group [3]. After the Abelian projection is fixed, the matrix $X[U]$ becomes diagonal and the theory possesses the (residual) $U(1)$ gauge symmetry. The most popular examples of the diagonalization gauges are the Abelian Polyakov (AP) gauge and the Abelian field strength gauge (F_{12} gauge). The Polyakov gauge corresponds to the diagonalization of the Polyakov line,

$$X_x[U] \equiv U_{\mathbf{x}, x_4, 0} U_{\mathbf{x}, x_4+1, 0} \ldots U_{\mathbf{x}, x_4-1.0},$$

where $x = \{\mathbf{x}, x_4\}$. The F_{12} gauge is defined by the diagonalization of the 12-plaquette, $X_x[U] \equiv U_{x, 12}$, where $U_{x, \mu\nu} = U_{x, \mu} U_{x+\tilde{\mu}, \nu} U^\dagger_{x+\tilde{\nu}, \mu} U^\dagger_{x, \nu}$.

There are conflicting reports on the gauge independence of the dual superconductor mechanism of the color confinement (a review of the current literature on this subject can be found in [10]). Needless to say, this question is important for understanding of the properties of the QCD vacuum. It is natural to think that the confinement—as a gauge-invariant phenomenon—cannot be described by a gauge-dependent model. On the other hand, the Abelian projection by itself can be considered as just a gauge-dependent tool to associate the confining gluon configurations with the Abelian monopoles. This tool may work well in one gauge and may not work in another gauge.

Analytical considerations of [10] show that, in the AP gauge (contrary to the MA gauge), the dual superconductor mechanism cannot be realized. It was concluded that the Abelian projection mechanism is projection-dependent. However, the projection (in)dependence of the monopole condensate could not be proven within an analytical approach. To check this issue, we study below the condensate of the Abelian monopoles in the finite temperature $SU(2)$ gauge theory in the AP and the F_{12} projections and compare it with the condensate in the MA gauge.

We study numerically the $SU(2)$ gauge theory with the standard Wilson action, $S[U] = -\beta \sum_P \mathrm{Tr}\, U_P$, where the sum goes over the plaquettes P and β is the lattice bare gauge coupling related to the continuum gauge coupling g, $\beta = 1/4g^2$. The $SU(2)$ link field is parametrized in the standard way:

$$U_{x\mu} = \begin{pmatrix} \cos\phi_{x\mu} e^{i\theta_{x\mu}} & \sin\phi_{x\mu} e^{i\chi_{x\mu}} \\ -\sin\phi_{x\mu} e^{-i\chi_{x\mu}} & \cos\phi_{x\mu} e^{-i\theta_{x\mu}} \end{pmatrix}.$$

In an Abelian projection, the allowed gauge transformations have a diagonal form. Under these transformations, the diagonal field θ transforms into an Abelian gauge field, the off-diagonal field χ changes into a double charged matter field, and the field ϕ remains intact:

$$\theta_{x\mu} \longrightarrow \theta_{x\mu} + \omega_x - \omega_{x+\hat{\mu}},$$

$$\chi_{x\mu} \longrightarrow \chi_{x\mu} + \omega_x + \omega_{x+\hat{\mu}},$$

$$\phi_{x\mu} \longrightarrow \phi_{x\mu}.$$

The $SU(2)$ plaquette action contains [11] various interactions between these fields as well as the action for the Abelian gauge field θ:

$$S[U] = -\sum_P \beta_P[\phi] \cos\theta_P + \ldots. \quad (3)$$

Here, $\theta_P = \theta_1 + \theta_2 - \theta_3 - \theta_4$ is a lattice analogue of the Abelian field strength tensor and $\beta_P[\phi]$ is an effective coupling constant dependent of the fields ϕ [11].

Following [7], we apply the monopole creation operator of Fröhlich and Marchetti [12] to the Abelian part of non-Abelian action (3). Effectively, this operator shifts the Abelian plaquette variable θ_P as follows:

$$\Phi_{\mathrm{mon}}(x) = \exp\left\{\sum_P \beta_P[\phi][\cos(\theta_P + W_P(x)) - \cos(\theta_P)]\right\}, \quad (4)$$

where the tensor W_P can be written in a compact way with the help of the differential form formalism on the lattice [4]. In this formalism, the δ– (d–) operator is the backward (forward) derivative on the lattice which decreases (increases) by one the rank of the form on which it is acting. The rank of the form is determined by the dimensionality of the lattice cell on which this form is defined. For example, a scalar function is a 0-form, the vector function is a 1-form, etc. Suppose that A is a lattice vector, then δA is a scalar (a lattice analogue of the divergence, $\partial_\mu A_\mu$), while dA is an antisymmetric tensor (a lattice analogue of the curl, $\partial_{[\mu,} A_{\nu]}$). The lattice Laplacian is $\Delta = \delta d + d\delta$, and Δ^{-1} denotes the inverse Laplacian. The lattice Kronecker symbol is denoted as δ_x: it is a scalar function, which is equal to unity at the site x and zero otherwise. The *-operator relates the forms on the dual and original lattice. For example, if B is a scalar function (0-form) on the original lattice, then $*B$ is a 4-form on the dual lattice.

The plaquette function W in Eq. (4) is defined as follows:[1] $W = 2\pi\delta\Delta^{-1}(D_x - \omega_x)$. Here, the lattice 1-form $*\omega_x$ represents the Dirac string attached to the monopole on the dual lattice (thus, ω_x is a 3-form on the original lattice). The form $*\omega_x$ is zero outside the string position, and it is equal to plus or minus unity (depending on the orientation) on the string. The three-dimen-

[1] We omit a lengthy derivation of the tensor W and refer an interested reader to [12].

sional form D_x is called the "Dirac cloud" because it represents a lattice analogue of the radially symmetric (Coulomb) magnetic field of a monopole. This form satisfies the equation $\delta^* D_x = {}^*\delta_x$, which is a lattice analogue of the Maxwell equation in continuum, $\mathrm{div}\mathbf{H}(x) = \rho(x)$. Here, $\rho(x)$ is the density of the monopoles. In our case, we introduce one monopole at the origin of the lattice; therefore, the lattice monopole density is just a Kronecker symbol, $\rho = \delta_x$.

A partition function of any compact $U(1)$ model can be rewritten as a sum over closed monopole trajectories [4, 7]. The quantum average of the operator $\Phi_{\mathrm{mon}}(x)$ can be represented as a sum over all closed monopole trajectories plus one open trajectory, which begins at point x. Thus, this operator does create a monopole at the point x. The operator is invariant under local gauge transformations. Another property of operator (4) is that it is defined up to a complex phase: the operator $e^{i\alpha}\Phi_{\mathrm{mon}}(x)$ also creates a monopole at the point x. For the sake of definiteness, we study the positively defined operator (4) with $\mathrm{Im}\,\Phi_{\mathrm{mon}}$ and $\mathrm{Re}\,\Phi_{\mathrm{mon}} \geq 0$.

The object of our interest in this paper is the effective potential on the monopole field. According to [7], this potential is defined as follows:

$$V(\Phi) = -\ln\langle\delta(\Phi - \Phi_{\mathrm{mon}}(x))\rangle. \qquad (5)$$

The minimum of $V(\Phi)$ corresponds to the monopole condensate.

We simulate the $SU(2)$ on the lattice $16^3 \times 4$ with C-periodic boundary conditions in space directions [13]. The C periodicity corresponds to the antiperiodicity for the Abelian gauge fields, which is required by the Gauss law [7]. In the case of $SU(2)$ gauge group, the C-periodic boundary conditions are almost trivial: on the boundary, we have $U_{x,\mu} \longrightarrow \Omega^+ U_{x,\mu}\Omega$, $\Omega = i\sigma_2$.

To get the effective potential, we use 400 configurations of the $SU(2)$ gauge fields. On each configuration, the distribution of the monopole creation operator is evaluated at 20 points. The logarithm of the distribution provides us with effective potential (5). To evaluate the errors of the potential, we use the bootstrap method.

In Fig. 1, we show the effective potential $V(\Phi)$ (Eq. (5)) at various values of the gauge coupling β in the MA, AP, and F_{12} gauges. The potential is shown for positive real values of the field Φ: $\mathrm{Re}\Phi \geq 0$, $\mathrm{Im}\Phi = 0$. The minimum of the effective potential corresponds to the value of the monopole condensate (in lattice units). The results for the MA gauge (quoted below) are taken from [7]. The critical gauge coupling corresponding to the temperature phase transition at chosen lattice geometry is $\beta_c \approx 2.3$. Thus, Figs. 1a–1c correspond to the confinement phase, while Fig. 1d is plotted for the deconfinement phase.

First of all, we note that, for all considered values of β, (i) the minima of the potentials in the AP and F_{12} gauges coincide with each other within numerical errors and (ii) the potential in the MA gauge is different

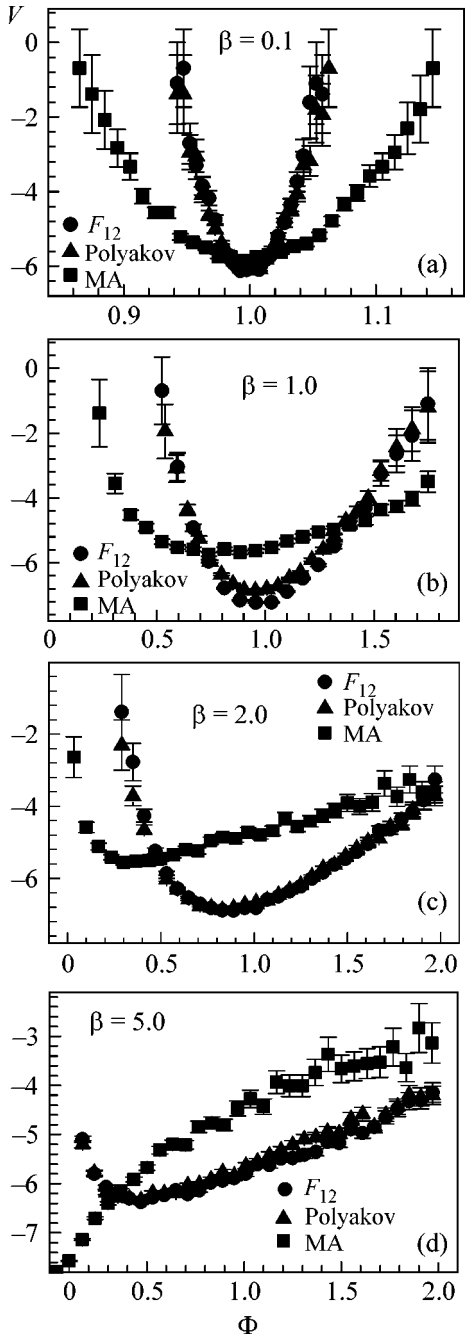

Fig. 1. The potential on the monopole field in the MA, AP, and F_{12} gauges at various values of the gauge coupling β. The data for the MA gauge are taken from [7].

from AP and F_{12} potentials. According to Fig. 1a, in the strong coupling limit ($\beta = 0.1$), the minima of the monopole potential in all three gauges are located at the same point, $\Phi_{\mathrm{min}} \approx 1$. However, as one can see from other figures, this coincidence is lifted as we increase β. As we increase the value of β, the difference in the monopole condensates in the MA gauge and in the AP and F_{12} gauges appears evident (Figs. 1b, 1c). Moreover, in the deep deconfinement phase (Fig. 1d), the

monopole condensate vanishes in the MA gauge, while in the AP and F_{12} gauges, the condensate is nonzero.

Summarizing, we have presented evidence that the monopole condensates in different Abelian projections coincide with each other only in the (unphysical) strong coupling region. Generally, the condensate depends on the choice of the Abelian projection. Our results are in contradiction with conclusions of [14], where condensate was found to be projection-independent. Since our results are based on the well-justified theory of the Fröhlich–Marchetti operator, we suggest that the difference between the results of our paper and [14] originates in the improper choice of the monopole creation operator in [14].

This work was supported by the Russian Foundation for Basic Research (grant nos. 02-02-17308 and 01-02-17456), by RFBR–DFG (grant no. 03-02-04016), by INTAS (grant no. 00-00111), by CRDF award RPI (grant no. 2364-MO-02), and by MK (grant no. 4019.2004.2).

REFERENCES

1. V. Singh, D. A. Browne, and R. W. Haymaker, Phys. Lett. B **306**, 115 (1993); G. S. Bali, K. Schilling, and C. Schlichter, Phys. Rev. D **51**, 5165 (1995); G. S. Bali, C. Schlichter, and K. Schilling, Prog. Theor. Phys. Suppl. **131**, 645 (1998); F. V. Gubarev, E. M. Ilgenfritz, M. I. Polikarpov, and T. Suzuki, Phys. Lett. B **468**, 134 (1999); Y. Koma, M. Koma, E. M. Ilgenfritz, and T. Suzuki, hep-lat/0308008.
2. G.'t Hooft, in *High Energy Physics: EPS International Conference*, Ed. by A. Zichichi (Palermo, 1975); S. Mandelstam, Phys. Rep. **23**, 245 (1976).
3. G.'t Hooft, Nucl. Phys. B **190**, 455 (1981).
4. M. N. Chernodub and M. I. Polikarpov, in *Confinement, Duality, and Nonperturbative Aspects of QCD*, Ed. by P. van Baal (Plenum, New York, 1998), p. 387; hep-th/9710205.
5. T. Suzuki and I. Yotsuyanagi, Phys. Rev. D **42**, 4257 (1990); H. Shiba and T. Suzuki, Phys. Lett. B **333**, 461 (1994); G. S. Bali, V. Bornyakov, M. Müller-Preussker, and K. Schilling, Phys. Rev. D **54**, 2863 (1996).
6. A. S. Kronfeld, M. L. Laursen, G. Schierholz, and U. J. Wiese, Phys. Lett. B **198**, 516 (1987); A. S. Kronfeld, G. Schierholz, and U. J. Wiese, Nucl. Phys. B **293**, 461 (1987).
7. M. N. Chernodub, M. I. Polikarpov, and A. I. Veselov, Phys. Lett. B **399**, 267 (1997); Nucl. Phys. (Proc. Suppl.) **49**, 307 (1996).
8. V. A. Belavin, M. N. Chernodub, and M. I. Polikarpov, Pis'ma Zh. Éksp. Teor. Fiz. **75**, 263 (2002) [JETP Lett. **75**, 217 (2002)]; Phys. Lett. B **554**, 146 (2003).
9. A. Di Giacomo and G. Paffuti, Phys. Rev. D **56**, 6816 (1997).
10. M. N. Chernodub, hep-lat/0308031.
11. M. N. Chernodub, M. I. Polikarpov, and A. I. Veselov, Phys. Lett. B **342**, 303 (1995).
12. J. Fröhlich and P. A. Marchetti, Commun. Math. Phys. **112**, 343 (1987).
13. U. J. Wiese, Nucl. Phys. B **375**, 45 (1992).
14. A. Di Giacomo, B. Lucini, L. Montesi, and G. Paffuti, Phys. Rev. D **61**, 034503 (2000); Phys. Rev. D **61**, 034504 (2000).

JETP Letters, Vol. 79, No. 6, 2004, pp. 249–252. From Pis'ma v Zhurnal Éksperimental'noĭ i Teoreticheskoĭ Fiziki, Vol. 79, No. 6, 2004, pp. 307–310.

Neutrino Flavor Relaxation or Neutrino Oscillations?¶

I. N. Machulin and S. V. Tolokonnikov

Russian Research Centre Kurchatov Institute, Moscow, 123182 Russia

e-mail: machulin@in2p3.fr, tolkn@mbslab.kiae.ru

Received December 22, 2003; in final form, January 17, 2004

We propose the new mechanism of neutrino flavor relaxation to explain the experimentally observed changes of initial neutrino flavor fluxes. The test of neutrino relaxation hypothesis is presented using the data of modern reactor, solar, and accelerator experiments. The final choice between the standard neutrino oscillations and the proposed neutrino flavor relaxation model can be done in future experiments. © *2004 MAIK "Nauka/Interperiodica".*

PACS numbers: 14.60.Pq; 13.15.+q

Now, the phenomena of changes in initial neutrino flavor flux are observed in different neutrino experiments. The SNO experiment [1] evidently detects only one-third of the initial electron neutrino flux from the Sun and two-thirds of muon and (or) tau neutrino fluxes. The KamLAND reactor experiment [2] detected only 61% of expected electron antineutrino events from different reactors at a mean distance of 180 km. Convincing evidence of initial neutrino flavor flux changes is also observed in Super-K [3] and MACRO [4] atmospheric neutrino data and the K2K [5] accelerator experiment with muon neutrinos.

The standard way of interpreting these results lies in the neutrino oscillation hypothesis, first proposed by Pontecorvo [6] and developed in further works [7].

Here, we discuss the alternative mechanism of neutrino flavor relaxation, which can also describe the observed changes of initial neutrino flavor fluxes with distance.

The proposed model is similar to the mechanism [8] of spin relaxation in random fluctuating magnetic field **B** with zero average $\langle \mathbf{B}(t) \rangle = 0$ and mean square fluctuating field value $\langle \mathbf{B}^2(t) \rangle \neq 0$. The spin relaxation process is described by the Pauli master equation [9].

Let us assume the existence of some small random fluctuating vacuum field $\hat{V}$, causing the transitions between different lepton flavors. The field $\hat{V}$ can have mean zero value, with $\langle \hat{V}^2(t) \rangle$ different from 0 and $\Gamma = \langle \hat{V}^2(t) \rangle^{1//2} > m_{\nu_e}, m_{\nu_\mu}, m_{\nu_\tau}$. Interactions of neutrino flavors with such vacuum field should lead to flavor relaxation process.

The time evolution of the neutrino states are governed by the Schrödinger equation:

$$i\frac{d}{dt}|\nu(t)\rangle = \hat{H}(t)|\nu(t)\rangle, \tag{1}$$

where $|\nu(t)\rangle$ is the neutrino vector of state and $H(t)$ is the time-dependent Hamiltonian of the system, whose form depends on in what basis it is given.

In flavor basis, the total Hamiltonian in the random fluctuating vacuum field for rest reference frame can be written as

$$\hat{H}_f(t) = \hat{H}_m + \hat{V}_f(t), \tag{2}$$

where

$$\hat{H}_m = \begin{pmatrix} m_1 & 0 & 0 \\ 0 & m_2 & 0 \\ 0 & 0 & m_3 \end{pmatrix},$$
$$\hat{V}_f(t) = \begin{pmatrix} V_{ee}(t) & V_{e\mu}(t) & V_{e\tau}(t) \\ V_{\mu e}(t) & V_{\mu\mu}(t) & V_{\mu\tau}(t) \\ V_{\tau e}(t) & V_{\tau\mu}(t) & V_{\tau\tau}(t) \end{pmatrix}. \tag{3}$$

Here, H_m is the free Hamiltonian in mass basis. Note that, in this model, the neutrino flavor states are assumed to be the same as their massive states (or, in other words, the mixing mass matrix is diagonal).

$V_{\alpha\alpha'}$ ($\alpha = e, \mu, \tau$) is the vacuum field potential with mean value $\langle V_{\alpha\alpha'}(t) \rangle = 0$ and $\langle (V_{\alpha\alpha'}(t))^2 \rangle \neq 0$.

The neutrino flavor evolution in time can be obtained from Eqs. (1)–(3), using the density matrix

¶ This article was submitted by the authors in English.

approach [10], and is given by the Pauli master equation:

$$\frac{d}{dt}\begin{pmatrix} n_{\nu_e} \\ n_{\nu_\mu} \\ n_{\nu_\tau} \end{pmatrix} = \begin{pmatrix} -(W_{\mu e} + W_{\tau e}) & W_{e\mu} & W_{e\tau} \\ W_{\mu e} & -(W_{e\mu} + W_{\tau\mu}) & W_{\mu\tau} \\ W_{\tau e} & W_{\tau\mu} & -(W_{e\tau} + W_{\mu\tau}) \end{pmatrix} \times \begin{pmatrix} n_{\nu_e} \\ n_{\nu_\mu} \\ n_{\nu_\tau} \end{pmatrix}, \quad (4)$$

where $n_\alpha(t)$ ($\alpha = \nu_e, \nu_\mu, \nu_\tau$) are the probability of observing a neutrino with electron, muon, or tau flavor, $W_{\alpha\alpha'}$ corresponds to the neutrino transition rates from flavor α' to flavor α, and

$$\sum_{\alpha = \nu_e, \nu_\mu, \nu_\tau} n_\alpha(t) = 1.$$

The general solution of Eq. (4) is given by the sum of two exponents and a constant:

$$\begin{pmatrix} n_{\nu_e}(t) \\ n_{\nu_\mu}(t) \\ n_{\nu_\tau}(t) \end{pmatrix} = \begin{pmatrix} a_1 \\ a_2 \\ a_3 \end{pmatrix} + \begin{pmatrix} b_1 \\ b_2 \\ b_3 \end{pmatrix} e^{-t/T_1} + \begin{pmatrix} c_1 \\ c_2 \\ c_3 \end{pmatrix} e^{-t/T_2}, \quad (5)$$

with

$$\sum_{i=1}^{3} a_i = 1, \quad \sum_{i=1}^{3} b_i = 0, \quad \sum_{i=1}^{3} c_i = 0. \quad (6)$$

To illustrate the possibilities of the relaxation model, the particular "simple" solution can be found under the following assumptions:

(a) $W_{e\mu} = W_{\mu e}$, $W_{e\tau} = W_{\tau e}$, $W_{\mu\tau} = W_{\tau\mu}$,

(b) $W_{\mu\tau} \gg W_{e\mu}, W_{e\tau}$.

Now, Eq. (5) appears as

$$\begin{pmatrix} n_{\nu_e}(t) \\ n_{\nu_\mu}(t) \\ n_{\nu_\tau}(t) \end{pmatrix} = \begin{pmatrix} 1/3 \\ 1/3 \\ 1/3 \end{pmatrix} + b\begin{pmatrix} 0 \\ 1 \\ -1 \end{pmatrix} e^{-2W_{\mu\tau}t} + c\begin{pmatrix} -1 \\ 1/2 \\ 1/2 \end{pmatrix} e^{-3/2(W_{e\mu} + W_{e\tau})t}. \quad (7)$$

For $\gamma = E_\nu/m_\nu \gg 1$, the probability P of observing the neutrino flavor with energy E_ν at distance r from the source is given by

$$\begin{pmatrix} P_{\nu_e}(r) \\ P_{\nu_\mu}(r) \\ P_{\nu_\tau}(r) \end{pmatrix} = \begin{pmatrix} 1/3 \\ 1/3 \\ 1/3 \end{pmatrix} + b\begin{pmatrix} 0 \\ 1 \\ -1 \end{pmatrix} e^{-t/\Lambda_0 E_\nu} + c\begin{pmatrix} -1 \\ 1/2 \\ 1/2 \end{pmatrix} e^{-r/\Lambda_1 E_\nu}, \quad (8)$$

where we use the new notation $\Lambda_0 = (2W_{\mu\tau}m_\nu)^{-1}$ and $\Lambda_1 = 2/3[(W_{e\mu} + W_{e\tau})m_\nu]^{-1}$.

Equation (8) can be solved for different initial experimental conditions of neutrino flavor fluxes.

For initial pure electron neutrino or antineutrino flux (the case of solar or reactor experiments), $P_{\nu_e}(0) = 1$, $P_{\nu_\mu}(0) = P_{\nu_\tau}(0) = 0$, the solution is

$$P_{\nu_e}(r) = 1/3[1 + 2e^{-r/\Lambda_1 E_\nu}],$$
$$P_{\nu_\mu}(r) = 1/3[1 - e^{-r/\Lambda_1 E_\nu}], \quad (9)$$
$$P_{\nu_\tau}(r) = 1/3[1 - e^{-r/\Lambda_1 E_\nu}].$$

From KamLAND experiment data [2], it is possible to estimate the value of parameter Λ_1. Taking the effective energy of reactor antineutrino flux to be equal to 4.8 MeV (here, we take into account the threshold of the KamLAND detector $E_{\tilde{\nu}_e} > 3.4$ MeV), mean reactor distance 180 km, and $R = P_{\tilde{\nu}_e(\text{measured})}/P_{\tilde{\nu}_e(\text{expected})} = 0.61$, we obtain

$$\Lambda_1 = 43 \text{ km/MeV}.$$

Figure 1 illustrates the distance dependence of reactor antineutrino fluxes (for $E_{\tilde{\nu}} = 4.8$ MeV).

The final flavor survival probability 1/3 is consistent with the SNO [1] experimental data with the ratio of measured neutrino flavor fluxes

$$\frac{CC}{NC} = 0.306 \pm 0.026(\text{stat}) \pm 0.024(\text{syst}), \quad (10)$$

and with the absence of distortion in measured neutrino spectrum at low energies, while such distortion is predicted by LMA solution [11].

It also agrees with the Homestake results [12] for the ratio R of observed and predicted by standard solar model (SSM) [13] neutrino rates: $R = 0.34 \pm 0.03$.

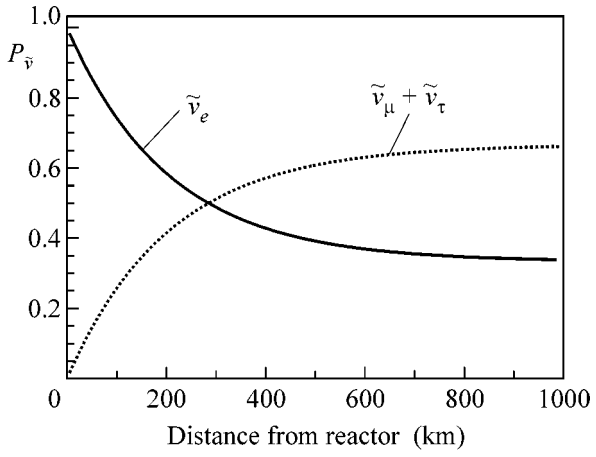

Fig. 1. Probability of observing different flavors from a reactor for $E_{\tilde{\nu}} = 4.8$ MeV.

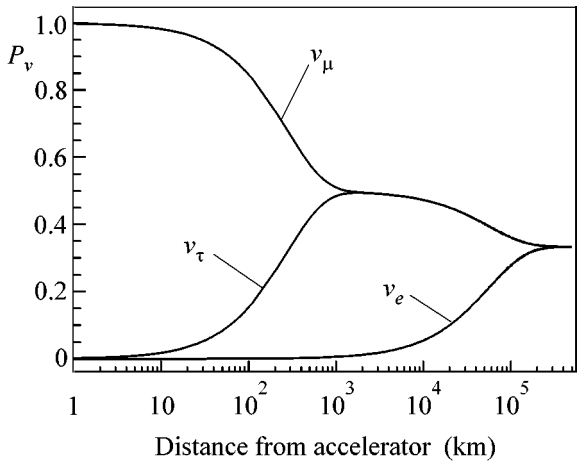

Fig. 2. Probability of observing different flavors from an accelerator muon neutrino beam for $E_\nu = 1.3$ GeV.

The deviation from the "simple" relaxation model exists for Gallium experiments [14, 15] with $R = 0.553 \pm 0.034$. But it is worth mentioning that the R value depends on the accuracy of SSM theoretical predictions.

For the case of pure initial muon neutrino or antineutrino flux (like in accelerator experiments), $P_{\nu_\mu}(0) = 1$, $P_{\nu_e}(0) = P_{\nu_\tau}(0) = 0$, the solution of Eq. (8) is

$$P_{\nu_e}(r) = 1/3[1 - e^{-r/\Lambda_1 E_\nu}],$$

$$P_{\nu_\mu}(r) = 1/3 + 1/2e^{-r/\Lambda_0 E_\nu} + 1/6e^{-r/\Lambda_1 E_\nu}, \qquad (11)$$

$$P_{\nu_\tau}(r) = 1/3 - 1/2e^{-r/\Lambda_0 E_\nu} + 1/6e^{-r/\Lambda_1 E_\nu}.$$

Preliminary estimation of parameter Λ_0 can be done using K2K accelerator experiment data [5]. Taking the mean energy of muon neutrino flux $E_\nu = 1.3$ GeV, distance $r = 250$ km,

$$R = P_{\nu_\mu(\text{measured})}/P_{\nu_\mu(\text{expected})} = 0.70$$

we obtain

$$\Lambda_0 = 0.21 \text{ km/MeV}.$$

Figure 2 illustrates the distance dependence of neutrino fluxes from muon neutrino beam ($E_\nu = 1.3$ GeV).

It is necessary to note that the estimations of neutrino relaxation parameters Λ_0 and Λ_1 are very preliminary and were made for illustration of the relaxation model. More precise calculations can be done also taking into account atmospheric neutrino data.

Finally, we would like to emphasize the main difference between the standard oscillation theory and the relaxation model proposed here: the dependence of neutrino flavor fluxes on the distance is described by the sum of a constant and two relaxation exponents, instead of the oscillation case. Figure 3 illustrates this difference for reactor antineutrino experiments.

Forthcoming reactor and accelerator neutrino experiments can provide the data necessary to choose between the neutrino oscillations and the proposed flavor relaxation model. Of course, the possibility of having a mixture of neutrino oscillation and relaxation processes also exists.

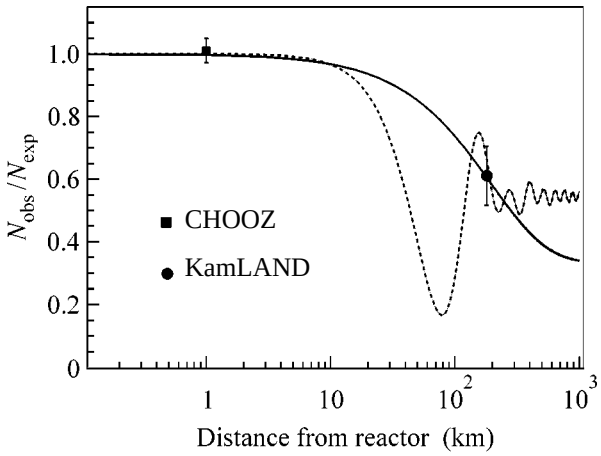

Fig. 3. The ratio of measured to expected $\tilde{\nu}_e$ flux from KamLAND [2] and CHOOZ [16] reactor experiments: (dotted curve) predictions of the oscillation model with $\sin^2 2\theta = 0.91$ and $\delta m^2 = 6.9 \times 10^{-5}$ (eV)^2 best-fit parameters from [2]; (solid curve) predictions of the "simple" relaxation model.

The authors would like to thank Academician S.T. Belyaev and Prof. M.I. Katsnelson for fruitful discussions.

REFERENCES

1. Q. R. Ahmad, R. C. Allen, T. C. Andersen, *et al.* (SNO Collab.), Phys. Rev. Lett. **89**, 011301 (2002); S. N. Ahmed, A. E. Anthony, E. W. Beier, *et al.* (SNO Collab.), nucl-ex/0309004 (2003).
2. K. Eguchi, S. Enomoto, K. Furuno, *et al.* (KamLAND Collab.), Phys. Rev. Lett. **90**, 021802 (2003).
3. Y. Fukida, T. Hayakawa, E. Ichihara, *et al.* (SK Collab.), Phys. Rev. Lett. **81**, 1562 (1998).
4. M. Ambrosio, R. Antolini, G. Auriemma, *et al.* (MACRO Collab.), Phys. Lett. B **517**, 59 (2001).
5. M. H. Ahn, S. Aoki, H. Bhang, *et al.* (K2K Collab.), Phys. Rev. Lett. **90**, 041801 (2003).
6. B. Pontecorvo, Zh. Éksp. Teor. Fiz. **34**, 247 (1957) [Sov. Phys. JETP **7**, 172 (1958)].
7. Z. Maki, M. Nakagava, and S. Sakata, Prog. Theor. Phys. **28**, 870 (1962); B. Pontecorvo, Zh. Éksp. Teor. Fiz. **53**, 1717 (1967) [Sov. Phys. JETP **26**, 984 (1968)].
8. C. P. Slichter, *Principles of Magnetic Resonance*, 3rd ed. (Springer, Berlin, 1989; Mir, Moscow, 1967); M. H. Levitt, *Spin Dynamics: Basics of Nuclear Magnetic Resonance* (Wiley, Chichester, 2001).
9. W. Pauli, *Collected Scientific Papers*, Ed. by R. Kronig and V. F. Weisskopf (Interscience, New York, 1964), Vol. 1.
10. K. Blum, *Density Matrix Theory and Its Applications* (Plenum, New York, 1981; Mir, Moscow, 1983).
11. A. Y. Smirnov, hep-ph/0311259 (2003).
12. B. T. Cleveland, T. Daily, R. Davis, *et al.*, Astrophys. J. **496**, 505 (1998).
13. J. N. Bahcal, M. H. Pinsonneault, S. Basu, *et al.*, Astrophys. J. **555**, 990 (2001).
14. J. N. Abdurashitov, V. N. Gavrin, S. V. Girin, *et al.* (SAGE Collab.), Phys. Rev. C **60**, 055801 (1999); J. N. Abdurashitov, V. N. Gavrin, S. V. Girin, *et al.*, Nucl. Phys. (Proc. Suppl.) **110**, 315 (2002).
15. M. Altmann, M. Balata, P. Belli, *et al.* (GNO Collab.), Phys. Lett. B **490**, 16 (2000); M. Altmann, M. Balata, P. Belli, *et al.*, Nucl. Phys. (Proc. Suppl.) **91**, 44 (2001).
16. M. Apollonio, A. Baldini, C. Bemporad, *et al.* (CHOOZ Collab.), Eur. Phys. J. C **27**, 331 (2003).

JETP Letters, Vol. 79, No. 6, 2004, pp. 253–256. Translated from Pis'ma v Zhurnal Éksperimental'noĭ i Teoreticheskoĭ Fiziki, Vol. 79, No. 6, 2004, pp. 311–314.

Entangled Photon States in Consecutive Nonlinear Optical Interactions

A. V. Rodionov and A. S. Chirkin*

Faculty of Physics, Moscow State University, Vorob'evy gory, Moscow, 119992 Russia

**e-mail: chirkin@squeez.phys.msu.su; aschirkin@pisem.net*

Received January 27, 2004

Quantum theory of two consecutive light-wave parametric interactions with aliquant frequencies produced by a common pump wave in a crystal is developed. Using the differentiation method, the unitary evolution operator of the system is reduced to an ordered form that allows the calculation of the field state and the statistical characteristics of interacting waves. It is shown that, for the initial vacuum field state, the created photons obey the super-Poisson statistics at the interacting frequencies and are in a multiparticle entangled state. © *2004 MAIK "Nauka/Interperiodica".*

PACS numbers: 42.50.Dv; 42.65.Ky; 03.67.Mn; 03.65.Ud

The object of this letter is to develop the quantum theory of consecutive nonlinear optical interactions of waves with aliquant frequencies and analyze the states of the generated photons. It will be shown that the type of interaction considered in this work can be the source of multiparticle (multiphoton) entangled states.

In quantum optics, one distinguishes between the entanglement of individual photons [1], quadrature field components [2], and Stokes parameters [3] characterizing the polarization state. Entangled quantum states are finding use both in the experiments on checking the quantum mechanical principles and in various applications of quantum information science [4].

At present, two-photon entangled states arising in the course of spontaneous parametric down-conversion (SPDC) in homogeneous nonlinear crystals lie at the basis of many applications of entangled states [5]. At the same time, for a number of reasons, the multiphoton entangled states are of special interest for applications. For example, when checking the Bell's inequalities [6] with two-particle entangled states, the contradiction with local realism takes place only for statistical predictions [7], whereas, in the case of multiparticle entanglement, it arises for determinate predictions [8]. By now, the methods of creating three- [9] and four-photon [10] entangled states using two independent pairs of polarization-entangled photon states and four-photon entangled states arising as a result of the action of a high-intensity short pump pulse in the course of SPDC have been suggested [11], together with the method of creating multiphoton entanglement in optical solitons [12].

In this work, a new source of multiphoton entangled states is considered based on two consecutive three-frequency interactions of waves with aliquant frequencies ω_1, ω_2, and ω_3 in the field of intense classical pumping with frequency ω_p. These interactions consist of the parametric process in the field of low-frequency pumping

$$\omega_p = \omega_1 + \omega_2 \quad (1)$$

and the parametric frequency summation

$$\omega_1 + \omega_p = \omega_3. \quad (2)$$

Processes (1) and (2) can simultaneously proceed during the collinear wave interaction in periodically poled nonlinear crystals, e.g., in an $LiNbO_3$ crystal [13]. In such crystals, the condition for the efficient energy exchange between the interacting waves (quasi-phase-matching condition) can simultaneously be met for processes (1) and (2) by choosing the poling period, i.e., the modulation period for the nonlinear wave-coupling coefficient [14].

In the approximation of an undepleted pump field, the simultaneous occurrence of processes (1) and (2) can be described by the interaction Hamiltonian of the form

$$H_{\text{int}} = i\hbar\{\beta_1(a_1^+a_2^+ - a_1a_2) + \beta_2(a_3^+a_1 - a_2a_1^+)\}, \quad (3)$$

where a_j^+ (a_j) is the creation (annihilation) operator for a photon with frequency ω_j, $\hbar$ is the Planck's constant, and β_j is the effective nonlinear coefficient proportional to the crystal quadratic susceptibility and pump-wave amplitude. The boson operators a_k^+ and a_j satisfy the standard commutation rules $[a_j, a_k^+] = \delta_{jk}$, where δ_{jk} is Kronecker delta. The terms containing the coefficient β_1 in Eq. (3) account for process (1), and the terms containing the coefficient β_2 account for process (2).

0021-3640/04/7906-0253$26.00 © 2004 MAIK "Nauka/Interperiodica"

The field state $|\Psi(z)\rangle$ at the output of a nonlinear crystal is determined by the unitary evolution operator $U(z) \equiv \exp[-iH_{\text{int}}z/\hbar]$:

$$|\Psi(z)\rangle = U(z)|\Psi(0)\rangle, \tag{4}$$

where $|\Psi(0)\rangle$ is the initial field state.

However, the general form of a direct action of the unitary operator on the initial state cannot be calculated without the preliminary transformation of this operator. For this reason, we introduce the anti-Hermitian operators

$$\begin{aligned}\sigma_d &= (a_1^+ a_2^+ - a_1 a_2),\\ \sigma_u &= \varepsilon(a_3^+ a_1 - a_3 a_1^+),\\ \sigma_a &= -\varepsilon(a_2^+ a_3^+ - a_2 a_3),\end{aligned} \tag{5}$$

where the coefficient $\varepsilon = \beta_2/\beta_1$ is chosen to be real without loss of generality. The auxiliary operator σ_a formally describes the generation process for frequencies ω_2 and ω_3 in a pump field with frequency $\omega_2 + \omega_3$. The operators σ_d, σ_u, and σ_a obey the SH(3) algebra [15]; i.e., they form a closed set with respect to the commutation operations:

$$\begin{aligned}[\sigma_d, \sigma_u] &\equiv \sigma_d\sigma_u - \sigma_u\sigma_d = \sigma_a,\\ [\sigma_a, \sigma_d] &= -\sigma_u, \quad [\sigma_u, \sigma_a] = \varepsilon^2\sigma_d.\end{aligned} \tag{6}$$

In the new notation, the unitary operator can be represented in two equivalent forms:

$$\begin{aligned}U(\zeta) &= e^{\zeta(\sigma_d + \sigma_u)}\\ &= \exp[\alpha(\zeta)\sigma_d]\exp[\eta(\zeta)\sigma_a]\exp[\xi(\zeta)\sigma_u],\end{aligned} \tag{7}$$

where $\zeta \equiv \beta_1 z$ and $\alpha(\zeta)$, $\eta(\zeta)$, and $\xi(\zeta)$ are the unknown functions to be determined by the differentiation method [16]. In this method, the differentiation of both sides of the equality with respect to ζ is followed by the operator transformations of $U(\zeta)$ to set it off on the right-hand side of the equality and by equating the coefficients of operators σ_d, σ_a, and σ_u. Note that the sequence of exponential operators on the right-hand side of Eq. (7) is dictated by the convenience of solving the problem.

To determine the functions $\alpha(\zeta)$, $\eta(\zeta)$, and $\xi(\zeta)$, we obtain the following system of nonlinear differential equations:

$$\begin{aligned}&\alpha'(\zeta) - \varepsilon\xi'(\zeta)\sinh(\eta(\zeta)\varepsilon) = 1,\\ &\eta'(\zeta)\cosh(\alpha(\zeta)) + \xi'(\zeta)\cosh(\eta(\zeta)\varepsilon)\sinh(\alpha(\zeta)) = 0,\\ &\eta'(\zeta)\sinh(\alpha(\zeta)) + \xi'(\zeta)\cosh(\eta(\zeta)\varepsilon)\cosh(\alpha(\zeta)) = 1\end{aligned} \tag{8}$$

with the initial conditions $\alpha(0) = \eta(0) = \xi(0) = 0$.

One can verify that the solution to Eq. (8) for $\varepsilon < 1$ is given by the functions

$$\begin{aligned}\alpha(\zeta) &= \operatorname{arctanh}\frac{\theta\sinh\theta\zeta}{\cosh\theta\zeta - \varepsilon^2},\\ \eta(\zeta) &= \varepsilon^{-1}\operatorname{arcsinh}\varepsilon\theta^{-2}(1 - \cosh\theta\zeta),\\ \xi(\zeta) &= \int_0^\zeta \frac{\cosh[\alpha(x)]}{\cosh[\varepsilon\eta(x)]}dx,\end{aligned} \tag{9}$$

where $\theta \equiv \sqrt{1 - \varepsilon^2}$. The particular form of the function $\xi(\zeta)$ is immaterial to our analysis.

Next, we apply the ordering procedure to each exponential operator in Eq. (7). The ordered form of the operator $\exp[\alpha(\xi)\sigma_d]$ is presented, e.g., in [17]. As a result, we obtain the following final ordered expression for the unitary evolution operator:

$$\begin{aligned}U(\zeta) &= \exp[\tanh(\alpha)a_1^+ a_2^+]\\ &\times \exp[-\ln(\cosh(\alpha))(1 + a_1^+ a_1 + a_2^+ a_2)]\\ &\times \exp[-\tanh(\varepsilon\eta)a_2^+ a_3^+]\exp[-\tanh(\alpha)a_1 a_2]\\ &\times \exp[\tanh(\varepsilon\eta)\tanh(\alpha)a_3^+ a_1]\\ &\times \exp[-\ln(\cosh(\varepsilon\eta))(1 + a_2^+ a_2 + a_3^+ a_3)]\\ &\times \exp[\tanh(\varepsilon\xi)a_3^+ a_1]\\ &\times \exp[\tanh(\varepsilon\eta)a_2 a_3]\exp[\tanh(\varepsilon\eta)\tan(\varepsilon\xi)a_1 a_2]\\ &\times \exp[-\ln(\cos(\varepsilon\xi))(a_1^+ a_1 - a_3^+ a_3)]\\ &\times \exp[-\tan(\varepsilon\xi)a_1^+ a_3],\end{aligned} \tag{10}$$

where $\alpha \equiv \alpha(\zeta)$, $\eta \equiv \eta(\zeta)$, and $\xi \equiv \xi(\zeta)$.

Assume that only the intense pump wave is fed into a nonlinear crystal, while the initial states of the ω_1, ω_2, and ω_3 fields are the vacuum states; i.e., the initial state vector is $|\Psi(0)\rangle = |0\rangle_1|0\rangle_2|0\rangle_3 \equiv |0, 0, 0\rangle$. According to Eq. (10), the state at the crystal output is

$$\begin{aligned}|\Psi(\zeta)\rangle &= \frac{1}{\cosh\alpha(\zeta)}\frac{1}{\cosh(\varepsilon\eta(\zeta))}\sum_{m,n=0}^{\infty}(\tanh\alpha(\zeta))^m\\ &\times\left(-\frac{\tanh(\varepsilon\eta(\zeta))}{\cosh\alpha(\zeta)}\right)^n\sqrt{\frac{(m+n)!}{m!n!}}|m, m+n, n\rangle.\end{aligned} \tag{11}$$

Here, m is the number of photons with frequency ω_1, $m + n$ is the number of photons with frequency ω_2, and n is the number of photons with frequency ω_3. The states $|m, m + n, n\rangle$ form the orthogonal basis in the space of Fock's states. In fact, Eq. (11) fully determines the solution to our problem. Using state vector (11), one can write the expression for the density matrix $\rho = |\Psi(\zeta)\rangle\langle\Psi(\zeta)|$ and calculate the statistical characteristics of the generated radiation at the crystal output.

The photon-number distribution functions $P_j(N) = \mathrm{Sp}(\rho_j \hat{N})$, where $\hat{N}$ is the photon-number operator and ρ_j is the density matrix of the field ω_j, are given by the expressions

$$P_1(N) = \frac{\tanh^{2N}(\alpha(\zeta))}{\cosh^2(\varepsilon\eta(\zeta))},$$

$$P_2(N) = \frac{1}{\cosh^2(\alpha(\zeta))\cosh^2(\varepsilon\eta(\zeta))} \times\left(1 + \frac{\tanh^2(\varepsilon\eta(\zeta))}{\sinh^2(\alpha(\zeta))}\right)^N \tanh^{2N}(\alpha(\zeta)), \quad (12)$$

$$P_3(N) = \frac{\tanh^{2N}(\varepsilon\eta(\zeta))}{\cosh^2(\varepsilon\eta(\zeta))}.$$

It follows that the statistics of generated photons has, in the general case, a super-Poisson character (the photon-number variance is much greater than the mean photon number). However, for small interaction lengths ($\beta_1 z < 1$), it is close to the Poisson statistics.

One has for the mean photon numbers

$$\langle n_1(\zeta)\rangle = \sinh^2\alpha(\zeta)\cosh^2(\varepsilon\eta(\zeta)),$$
$$\langle n_3(\zeta)\rangle = \sinh^2(\varepsilon\eta(\zeta)), \quad (13)$$
$$\langle n_2(\zeta)\rangle = \langle n_1(\zeta)\rangle + \langle n_3(\zeta)\rangle.$$

Taking into account Eq. (9), one obtains

$$\langle n_1(\zeta)\rangle = \theta^{-2}\sinh^2(\theta\zeta),$$
$$\langle n_3(\zeta)\rangle = \varepsilon^2\theta^{-2}(\cosh(\theta\zeta) - 1)^2. \quad (14)$$

According to Eq. (13), the mean number of photons increases exponentially at $\varepsilon < 1$ (θ is real). In this case, $\beta_1 > \beta_2$; i.e., the pump-photon decay into the photons with frequencies ω_1 and ω_2 is more efficient than the photon creation at frequency ω_3. In the opposite case ($\beta_1 < \beta_2$, $\varepsilon > 1$), the hyperbolic functions in Eqs. (9) should be replaced by the trigonometric functions ($\sinh \longrightarrow \sin$, $\cosh \longrightarrow \cos$, and $\theta^2 \longrightarrow (\varepsilon^2 - 1)$), while the statistical parameters depend on the interaction length in an oscillatory manner.

According to Eq. (11), the field at the crystal output is in the entangled state [18], because it cannot be represented in the factorized form $|\Psi\rangle \neq |\Psi_1\rangle \otimes |\Psi_2\rangle \otimes |\Psi_3\rangle$, where $|\Psi_j\rangle$ is the field state at frequency ω_j. Assume that one can set off, e.g., a field with two photons with frequency ω_2. Then, the normalized vector of the corresponding state is

$$|\Psi(\zeta)\rangle_{\mathrm{cond}} = \mathcal{N}\{q_{20}(\zeta)|2, 2, 0\rangle + q_{11}(\zeta)|1, 2, 1\rangle + q_{02}(\zeta)|0, 2, 2\rangle\}. \quad (15)$$

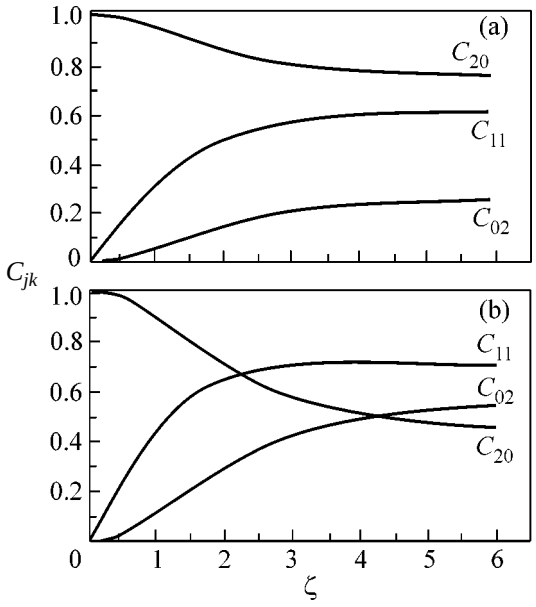

Fig. 1. Probability amplitudes C_{jk} of two-photon generation at frequency ω_2 and j and k photons at frequencies ω_1 and ω_3, respectively, as functions of the reduced interaction length $\zeta = \beta_1 z$ for $\varepsilon = \beta_2/\beta_1$ = (a) 0.5 and (b) 0.75.

The coefficients q_{ij} are determined from Eq. (11), and $\mathcal{N}^2 \equiv (q_{20}^2(\zeta) + q_{11}^2(\zeta) + q_{02}^2(\zeta))^{-1}$ is the normalization factor. For the frequencies ω_1 and ω_3, we have an analogue of a three-level system for this set of photon numbers. Such field states can probably be used as qutrits. An alternative method of obtaining qutrits is considered in [19].

The probability amplitudes $C_{jk}(\zeta) = \mathcal{N}q_{jk}(\zeta)$ are shown in Fig. 1 as functions of the interaction length. One can see that the probability amplitudes for the field configurations considered differ only slightly at some interaction lengths. Estimates show that the value $\zeta = \beta_1 z = 1$ in an $LiNbO_3$ crystal of length 1 cm is achieved for the pump intensity $I \sim 10^6$ W/cm^2 ($e \longrightarrow ee$ interaction type).

To characterize the coupling of the ω_1, ω_2, and ω_3 photons, the three-photon correlation coefficient

$$g^{(3)}(n_1, n_2, n_3) \equiv \frac{\langle n_1 n_2 n_3\rangle}{\langle n_1\rangle\langle n_2\rangle\langle n_3\rangle} = \frac{2[2 + 3\sinh^2\alpha(\zeta) + \tanh^2(\varepsilon\eta(\zeta))]}{\sinh^2\alpha(\zeta) + \tanh^2(\varepsilon\eta(\zeta))} \quad (16)$$

was calculated, which can be measured in a triple-coincidence scheme. The typical dependence of $g^{(3)}$ on the interaction length is shown in Fig. 2. It follows from this figure that there is a strong nonclassical correlation between the ω_1, ω_2, and ω_3 photons at the initial interaction stage, and this correlation weakens as the interaction length increases. Indeed, $g^{(3)} = 1$ for the coherent

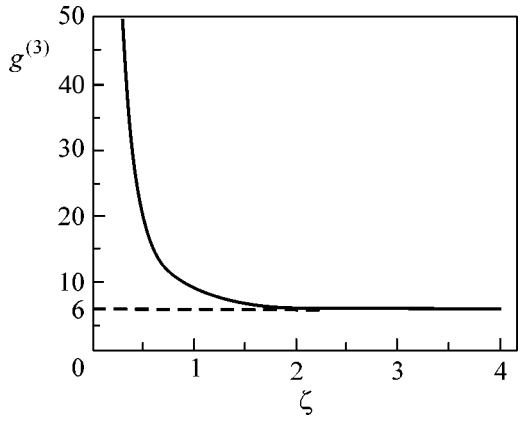

Fig. 2. Three-photon correlation coefficient $g^{(3)}(n_1, n_2, n_3)$ as a function of the reduced interaction length $\zeta = \beta_1 z$ for $\varepsilon = \beta_2/\beta_1 = 0.5$.

and statistically independent fields. At the same time, $g^{(3)} = 6$ for the fully statistically dependent fields obeing Gaussian statistics [20]. With an increase in the interaction length, the coefficient $g^{(3)}$ approaches this value from its larger values.

In conclusion, it should be emphasized that the main result of our theory consists in the derivation of the ordered expression for unitary evolution operator (10) describing consecutive nonlinear optical interactions with aliquant frequencies and in the derivation of Eq. (11) for the field-state vector at the output of a nonlinear crystal with the vacuum initial state. Equation (11) clearly demonstrates that the created photons are in the entangled state. For the photon numbers m and M at, respectively, frequencies ω_1 and ω_2, n photons are generated at the frequency ω_3, with $n = M - m$, and the numbers m and n can take values from 0 to M. Thus, the nonlinear optical interactions considered in this work can serve as a source of multiphoton entangled states.

We are grateful to S.P. Kulik for helpful discussion of the results and to V.I. Man'ko for the fruitful discussion on the group theory. This work was supported by the Russian Foundation for Basic Research (project no. 04-02-17554) and INTAS (grant no. 01-2097).

REFERENCES

1. L. Mandel and E. Wolf, *Optical Coherence and Quantum Optics* (Cambridge Univ. Press, Cambridge, 1995; Nauka, Moscow, 2000).
2. M. D. Reid and P. D. Drummond, Phys. Rev. Lett. **60**, 2731 (1988); M. D. Reid, Phys. Rev. A **40**, 913 (1989).
3. N. Korolkova, G. Leuchs, R. Loudon, *et al.*, Phys. Rev. A **65**, 052306 (2002); R. Schnabel, W. P. Bowen, N. Treps, *et al.*, Phys. Rev. A **67**, 012316 (2003).
4. *The Physics of Quantum Information: Quantum Cryptography, Quantum Teleportation, Quantum Computation*, Ed. by D. Bouwmeester, A. K. Ekert, and A. Zeilinger (Springer, Berlin, 2000; Postmarket, Moscow, 2002).
5. D. N. Klyshko, *Photons and Nonlinear Optics* (Nauka, Moscow, 1980).
6. J. S. Bell, Physics (Long Island City, N.Y.) **1**, 195 (1964).
7. S. J. Freedman and J. S. Clauser, Phys. Rev. Lett. **28**, 938 (1972).
8. D. M. Greenberger, M. A. Horne, A. Shimony, *et al.*, Am. J. Phys. **58**, 1131 (1990); D. M. Greenberger, M. A. Horne, and A. Zeilinger, Phys. Today **46** (8), 22 (1993).
9. D. Bouwmeester, J.-W. Pan, M. Daniell, *et al.*, Phys. Rev. Lett. **82**, 1345 (1999).
10. J.-W. Pan, M. Daniell, S. Gasparoni, *et al.*, Phys. Rev. Lett. **86**, 4435 (2001).
11. M. Eibl, S. Gaertner, M. Bourennane, *et al.*, Phys. Rev. Lett. **90**, 200403 (2003).
12. N. Korolkova and G. Leuchs, in *Coherence and Statistics of Photons and Atoms*, Ed. by J. Perina (Wiley, New York, 2001), p. 111.
13. E. Yu. Morozov and A. S. Chirkin, J. Opt. A: Pure Appl. Opt. **5**, 233 (2003).
14. A. S. Chirkin, V. V. Volkov, G. D. Laptev, *et al.*, Kvantovaya Élektron. (Moscow) **30**, 847 (2000).
15. N. Ya. Vilenkin, *Special Functions and the Theory of Group Representations* (Nauka, Moscow, 1965; American Mathematical Society, Providence, R.I., 1968).
16. J. Wei and E. Norman, J. Math. Phys. **4**, 575 (1963).
17. M. J. Collett, Phys. Rev. A **38**, 2233 (1988).
18. I. V. Bargatin, B. A. Grishanin, and V. N. Zadkov, Usp. Fiz. Nauk **171**, 625 (2001) [Phys. Usp. **44**, 597 (2001)].
19. A. V. Burlakov, M. V. Chekhova, O. A. Karabutova, *et al.*, Phys. Rev. A **60**, R4209 (1999); L. A. Krivitskiĭ, S. P. Kulik, A. N. Penin, *et al.*, Zh. Éksp. Teor. Fiz. **124**, 943 (2003) [JETP **97**, 846 (2003)].
20. S. A. Akhmanov, Yu. E. D'yakov, and A. S. Chirkin, *Introduction to Statistical Radio Physics and Optics* (Nauka, Moscow, 1981).

Translated by V. Sakun

JETP Letters, Vol. 79, No. 6, 2004, pp. 257–261. Translated from Pis'ma v Zhurnal Éksperimental'noĭ i Teoreticheskoĭ Fiziki, Vol. 79, No. 6, 2004, pp. 315–319.

Transformation of Director Configuration upon Changing Boundary Conditions in Droplets of Nematic Liquid Crystal

O. O. Prischepa, A. V. Shabanov, and V. Ya. Zyryanov*

Kirenskiĭ Institute of Physics, Siberian Division, Russian Academy of Sciences, Akademgorodok, Krasnoyarsk, 660036 Russia

**e-mail: zyr@iph.krasn.ru*

Received December 31, 2003; in final form, February 12, 2004

The transformation of the director configuration upon changing boundary conditions from planar to homeotropic for bipolar nematic droplets dispersed in a polymeric matrix was studied. The characteristic textural patterns are presented for droplets with different concentrations of homeotropic surfactants, and their orientational structure is identified. The scenario predicted earlier by G.E. Volovik and O.D. Lavrentovich (ZhETF 85, 1997 (1983)) for the transformation of orientational structure of nematic droplets from bipolar to radial, without the formation of additional disclinations, is revealed. It is shown that, by using the computational method of minimization of the director elastic-strain energy in the droplet bulk and by introducing the inhomogeneous boundary conditions, one can obtain orientational structures that are analogous to the observed ones.

PACS numbers: 61.30.Gd; 61.30.Eb

INTRODUCTION

Topological analysis is a rather efficient tool for studying spatially inhomogeneous structures in orientationally ordered systems, including various director and disclination configurations in liquid crystals (LCs). The classification of the topologically stable defects in nematic LC droplets has shown [1, 2] that the planar (tangential) orientation of nematic molecules at the interface is characterized by the bipolar direction configuration, with two point defects (boojums) arranged at the opposite sides of the droplet surface. In the case of a normal (homeotropic) nematic anchoring, the radial director ordering with a point defect (hedgehog) at the droplet center is the equilibrium structure, in accordance with the experimental observations [3, 4].

The theoretical analysis [2] of nematic droplets with varying boundary conditions suggests two possible scenarios for the interconversion of the bipolar and radial configurations. In the first case, one of the boojums in the bipolar structure gradually disappears and another transforms to a hedgehog, which subsequently breaks away from the surface and moves to the droplet center. In the second case, both boojums undergo changes in a similar manner, but the structure interconversion is accompanied by the formation of additional, including linear, disclinations.

In [2], a nematic with a lecithin impurity was dispersed in glycerol and taken for the experimental study. The surface anchoring of LC molecules in this system could be varied from homeotropic to planar by varying temperature in the range of nematic phase. In this case, the second structure-transformation scenario was realized with the formation of additional disclinations. However, considering that this composite consists of spherical LC droplets dispersed in an isotropic liquid matrix [2], one cannot assert that the observed scenario for the interconversion of orientational structures is universal for other objects as well, e.g., for the films of polymer-dispersed liquid crystal (PDLC) films that have been intensively studied in the last years. At the same time, a change in the boundary conditions by varying temperature is not the only approach to the study of this problem; a direct method is also possible. Namely, one can fabricate a set of samples with different concentrations of the required surface-active material and perform comparative analysis of their structural organization. This work was aimed at the detailed study of the director configurations in nematic droplets dispersed in a polymeric matrix, with the boundary condition varying as a result of varying concentration of the corresponding surfactant.

EXPERIMENTAL

The well-known 4-*n*-pentyl-4'-cyanobiphenyl (5CB) nematic liquid crystal with the transition temperatures "crystal $\overset{22^\circ C}{\longleftrightarrow}$ nematic $\overset{35^\circ C}{\longleftrightarrow}$ isotropic liquid" was chosen for the study. At T = 22°C and λ =

0021-3640/04/7906-0257$26.00

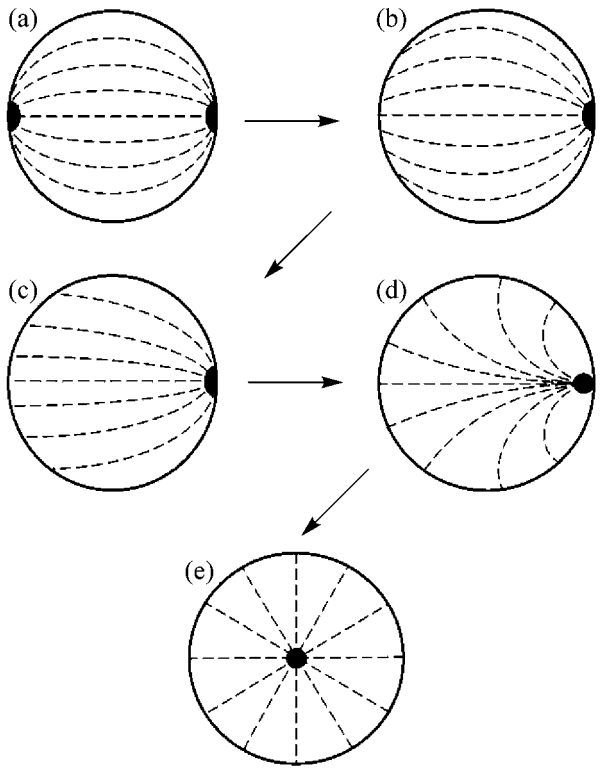

Fig. 1. The sequence of director configurations in nematic droplets with different lecithin content. The arrows are directed toward the increase in the surfactant content. (a) Bipolar droplet; (b) droplet with a destructed left boojum; (c) monopolar droplet; (d) surface hedgehog structure; and (e) radial structure.

0.589 μm, the refractive indices of 5CB are $n_{\parallel} = 1.725$ and $n_{\perp} = 1.534$ [5]. Poly(vinyl butyral) (PVB) of the 1PP type was used as a polymeric matrix. This polymer is transparent in the visible region and provides planar anchoring to the molecules of mesomorphic alkylcyanobiphenyl derivatives [6]. The refractive index of PVB is $n_p = 1.492$ at $T_c = 22°C$ and $\lambda = 0.589$ μm.

The homeotropic LC orientation at the interface was produced using lecithin—surface-active substance relating to the class of phospholipids. In the LC droplets with lecithin impurity, the long axes of surfactant molecules are arranged perpendicular to the surface in such a way that their polar groups are directed toward the interface, while the nonpolar fragments (flexible alkyl chains) are directed toward the bulk of the LC. As a result of such structural ordering, the lecithin molecules provide the homeotropic orientation of LC molecules at the interface.

Using a common solvent (ethyl alcohol) for all components, a set of samples with an LC content of 55% were prepared by the solvent-induced phase-separation method with the PVB and lecithin concentrations varying within 41.5–45.0 and 0–3.5 wt %, respectively. The ethanol evaporation rate was controlled so as to provide the same morphological parameters for the samples of composite film studied. The LC droplets formed a monolayer with a size dispersion of 4–16 μm.

The textural patterns of PDLC films were studied using a polarizing microscope both in the geometry of crossed polarizers and in the linearly polarized light with a switched-off analyzer. Observations showed that the textures of all droplets in a composite film without lecithin are typical for the bipolar director configuration (Fig. 1a). In the crossed polarizers, two symmetrically arranged hyperbola-shaped extinction bands are seen (Fig. 2a) that emanate from the droplet poles (point defects) and are gradually expanded. In the geometry with one polarizer, point defects are clearly seen as dark spots because of a strong optical inhomogeneity and, hence, intense local light scattering near the defects for any light polarization. For the same reason, the sections of droplet boundaries, where the light polarization coincides with the local director orientation and the gradient of refractive index $n_{\parallel} - n_p$ is large, are also clearly seen. By contrast, the boundary sections with the orthogonal arrangement of director and light polarization are seen least distinctly, because the gradient of refractive index $n_{\perp} - n_p$ is minimal in this region.

The sequence of director configurations arising in the nematic droplets upon an increase in the fraction of lecithin in the composite is schematically illustrated in Fig. 1. In the PDLC films with 0.08% lecithin, one of the boojums disappears in most (about 70%) of droplet ensemble. This is clearly seen in the bottom region of the droplet in Fig. 2b. The extinction band near the decaying boojum expands rather than narrows. In the remaining region of the droplet, the textural pattern has a form similar to the bipolar structure. The director-field distribution in these droplets can be represented by the configuration shown in Fig. 1b. It should be noted that the boundary conditions in this case are inhomogeneous. Here, the director in the bottom region of the droplet is oriented homeotropically. When moving along the surface to the remaining point defect, the director orientation becomes tilted and, finally, planar.

In samples with a higher lecithin content, the region of homeotropic and tilted director orientations increases and the director lines further straighten out (Fig. 1c), so that the structure, in essence, becomes monopolar. In [2], such a structure transformation was treated as "a continuous defect destruction accompanied by turning the size of its nucleus to infinity." In the crossed polarizers with the geometry presented in Fig. 2c, only one extinction band is seen in the droplet with such a director configuration. It emanates at the top of the point defect, strongly expands, and fills almost the entire lower half of the droplet. The texture of the upper half of the droplet is also analogous to the bipolar structure.

As the lecithin concentration increases, droplets with the surface hedgehog structure (Fig. 1d) and radial

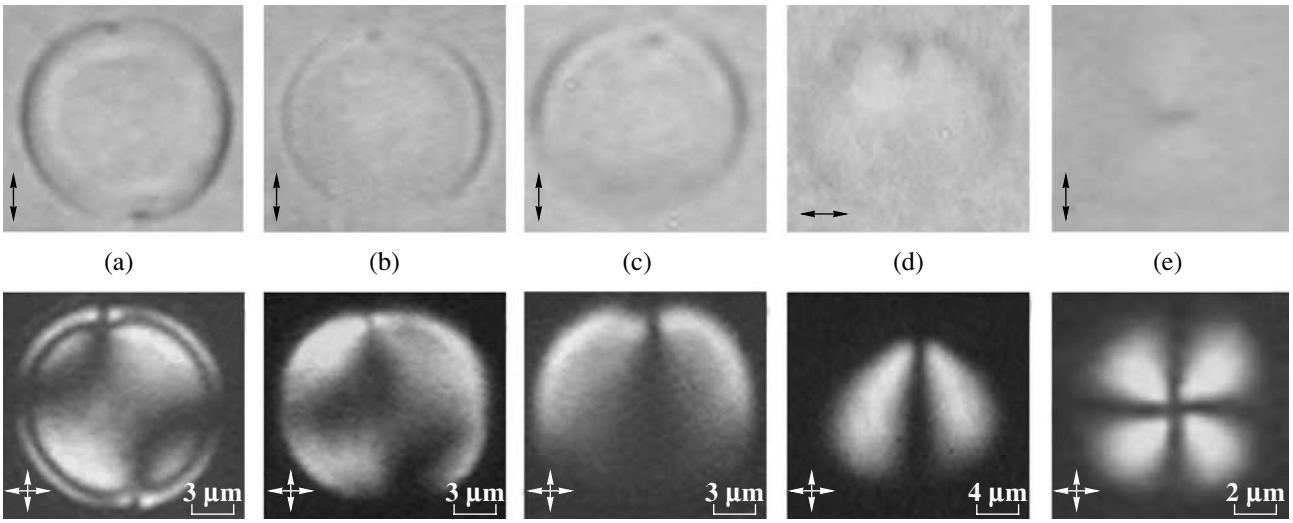

Fig. 2. Textural patterns of the 5CB LC nematic droplets dispersed in poly(vinyl butyral) with different lecithin concentrations C_{lec}. (bottom) Microphotographs in the geometry of crossed polarizers (shown by white arrows) and (top) photographs in the polarized light (the polarizer direction is shown by black arrows). (a) Bipolar droplet with symmetry axis directed at $\alpha = 11°$ with the polarizer, $C_{lec} = 0\%$; (b) droplet with a destructed bottom boojum, $\alpha = 11°$ and $C_{lec} = 0.08\%$; (c) monopolar droplet, $\alpha = 0°$ and $C_{lec} = 0.1\%$; (d) droplet with the surface hedgehog structure, $\alpha = 0°$ and C_{lec} 2.0%; and (e) droplet with the radial structure, $C_{lec} = 2.6\%$.

structure (Fig. 1e) appear. Droplets with the new structure appear and gradually increase in number. In this case, droplets with different director configurations can be observed simultaneously in the same PDLC film sample (Figs. 1a–1e), likely because of the inhomogeneous lecithin distribution over the film volume and due to some other factors, such as droplet shape, structure of the transition layer at the droplet surface, etc.

In the sequence of orientational structures from monopolar (Fig. 1c) to the surface hedgehog (Fig. 1d), the director field transforms in a smooth manner. One should identify these structures with care, because their textural patterns are, on the whole, similar. The distinctions in these textures are most clearly seen in the observation geometry shown in Figs. 2c and 2d. Here, only one extinction band is seen in the monopolar droplet. Three extinction bands are observed in the droplet with a surface hedgehog (Fig. 2d). The central band goes along the droplet symmetry axis, but it is much narrower than in the monopolar structure. Two side bands emanate from the point defect at an angle of approximately 50° to the symmetry axis on both its sides. As a result, such droplets are cone-shaped in the crossed polarizers (photographs of such textures were presented earlier in [7]), although they are, in fact, circular. The appearance of the three aforementioned extinction bands can be understood from the consideration of the corresponding director configuration shown in Fig. 1d. For the switched-off analyzer, the droplet boundaries adjacent to the defect are clearly seen for the monopolar structure if the light polarization is parallel to the symmetry axis (Fig. 2c). By contrast, the boundaries in the droplet with a surface hedgehog are seen most distinctly for the light polarized perpendicular to the symmetry axis (Fig. 2d).

CALCULATION OF DIRECTOR CONFIGURATION

The problem of determining the director configuration through the minimization of the orientational part of free energy

$$F = \frac{1}{2}\int K[(\nabla \cdot \mathbf{n})^2 + (\nabla \times \mathbf{n})^2]dV \qquad (1)$$

of the LC volume with a given boundary conditions can be solved analytically for some simple geometries, e.g., for the plane-parallel cells. Here, **n** is the nematic director and K is the elastic constant. For the droplet structures, the problem becomes more complicated, so the director field in this case is calculated numerically [8].

The transition structures described above (Figs. 1b–1d) were calculated within the framework of a three-dimensional model using the method developed in [9, 10] for the study of Friedericksz transitions in bipolar nematic droplets with rigidly fixed poles. The problem was solved in a one-constant approximation with the elastic modulus $K = (K_{11} + K_{22} + K_{33})/3$. The K_{ii} values were taken from [11]. The minimum of F in Eq. (1) was found by the variational method in the Cartesian coordinate system using the experimentally observed boundary conditions.

For example, to determine the director configuration for the texture shown Fig. 2b, the anchoring was assumed to be rigid and planar for all surface points

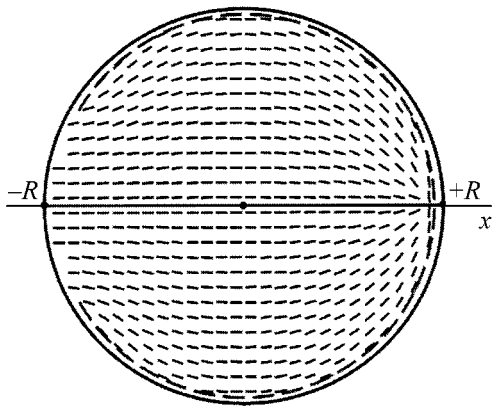

Fig. 3. The director configuration in the diametrical cross section passing through the symmetry axis of a spherical nematic droplet, as obtained by theoretical calculation within the framework of a 3D model with inhomogeneous boundary conditions. The dashed line near the surface shows the region with a specified planar director orientation.

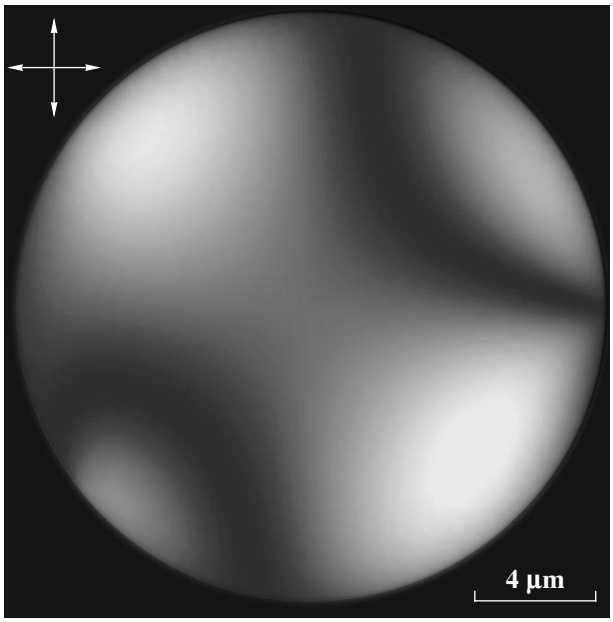

Fig. 4. Theoretically calculated texture of a spherical nematic droplet in crossed polarizers for the director configuration shown in Fig. 3 and an angle of 11° between the droplet symmetry axis and polarizer.

whose X coordinates fell within the interval $-0.8R \le X \le +R$. The azimuthal director direction in this surface region corresponded to the bipolar configuration with defects at the points $-R$ and $+R$ on the X axis. The boundary conditions were not specified for the rest of the surface with the coordinates $-R \le X < -0.8R$; i.e., the director orientation in this region was determined, as in the droplet volume, from the condition that the free energy be minimal. The resulting distribution of director field (Fig. 3) was similar to the configuration presented in Fig. 1b. In this distribution, the surface director orientation is also homeotropic near the point $-R$. When moving away from the symmetry axis, the orientation becomes tilted and then smoothly changes to planar.

Next, this information was used to calculate the corresponding textural patterns in crossed polarizers by applying the theoretical approach described in [12]. One can see (Fig. 4) that the theoretically calculated texture agrees well with the microphotograph of nematic droplet (Fig. 2b), taken for the same angle of inclination α of the symmetry axis to the polarizer.

CONCLUSIONS

Thus, a set of orientational structures intermediate between the bipolar and radial director configurations have been revealed for nematic droplets in PDLC film samples with various lecithin content. The data obtained are evidence that the change of surface anchoring from planar to homeotropic results in a gradual transformation of the bipolar structure of nematic droplets into the radial structure through a sequence of equilibrium director configurations without the formation of additional disclinations, as was predicted previously by the topological analysis in [1, 2]. Clearly, the approach described above allows the observation of only the equilibrium director configurations in different samples, whereas the temperature-induced variations of boundaries [2] allow one to trace the droplet restructurization dynamics. However, it should be remembered that not only the boundary conditions change in the second case but so do the elastic moduli that strongly influence the distribution of director field, thereby hampering the interpretation of the experimental results.

It should be emphasized that the surface anchoring in nematic droplets with intermediate configurations is inhomogeneous. Due to the use of the realistic inhomogeneous boundary conditions in our numerical calculation, the obtained director configurations and textural patterns of nematic droplets proved to be analogous to the experimentally observed ones.

This work was supported in part by the Presidium of the Russian Academy of Sciences (project no. 8.1), the Section of Physical Sciences of the Russian Academy of Sciences (project no. 2.10.2), and the Siberian Division of the Russian Academy of Sciences (integration project no. 18 and youth project no. 14).

REFERENCES

1. G. E. Volovik, Pis'ma Zh. Éksp. Teor. Fiz. **28**, 65 (1978) [JETP Lett. **28**, 59 (1978)].
2. G. E. Volovik and O. D. Lavrentovich, Zh. Éksp. Teor. Fiz. **85**, 1997 (1983) [Sov. Phys. JETP **58**, 1159 (1983)].

3. R. B. Meyer, Mol. Cryst. Liq. Cryst. **16**, 355 (1972).
4. S. Candau, P. LeRoy, and F. Debeauvais, Mol. Cryst. Liq. Cryst. **23**, 283 (1973).
5. V. Ya. Zyryanov and V. Sh. Épshteĭn, Prib. Tekh. Éksp. **2**, 164 (1987).
6. J. Cognard, *Alignment of Nematic Liquid Crystals and Their Mixtures* (Gordon and Breach, Paris, 1982; Universitetskoe, Minsk, 1986).
7. O. D. Lavrentovich, Pis'ma Zh. Tekh. Fiz. **14**, 166 (1988) [Sov. Tech. Phys. Lett. **14**, 73 (1988)].
8. S. Zumer and J. W. Doane, Phys. Rev. A **34**, 3373 (1986).
9. A. V. Shabanov, V. V. Presnyakov, V. Ya. Zyryanov, *et al.*, Pis'ma Zh. Éksp. Teor. Fiz. **67**, 696 (1998) [JETP Lett. **67**, 733 (1998)].
10. A. V. Shabanov, V. V. Presnyakov, V. Ya. Zyryanov, *et al.*, Mol. Cryst. Liq. Cryst. **321**, 245 (1998).
11. J. D. Bunning, T. E. Faber, and P. L. Sherrell, J. Phys. (Paris) **42**, 1175 (1981).
12. R. Ondris-Crawford, E. P. Boyko, B. G. Wagner, *et al.*, J. Appl. Phys. **69**, 6380 (1991).

Translated by V. Sakun

JETP Letters, Vol. 79, No. 6, 2004, pp. 262–267. Translated from Pis'ma v Zhurnal Éksperimental'noĭ i Teoreticheskoĭ Fiziki, Vol. 79, No. 6, 2004, pp. 320–325.

On the Relativistic Theory of Tunneling

V. S. Popov[1, *], B. M. Karnakov[2, **], and V. D. Mur[2]

[1] *Institute of Theoretical and Experimental Physics, Moscow, 117218 Russia*

**e-mail: markina@mail.itep.ru*

[2] *Moscow Institute of Engineering Physics (State University), Moscow, 115409 Russia*

***e-mail: karnak@theor.mephi.ru*

Received January 15, 2004

A relativistic generalization of the semiclassical theory of tunneling and multiphoton ionization of atoms and ions in the field of a high-intensity electromagnetic wave with linear, circular, and elliptic polarization is constructed. The exponential factor in the ionization probability is calculated for arbitrary values of adiabaticity parameter γ. In the case of low-frequency laser radiation, an asymptotically exact formula is derived for the ionization rate of the *s* atomic level, including the Coulomb, spin, and adiabatic corrections and the preexponential factor. © *2004 MAIK "Nauka/Interperiodica".*

PACS numbers: 32.80.Rm; 03.65.Xp; 03.65.Sq

1. Rapid progress in laser physics and technology has made it possible to attain the highest intensities $J \sim 10^{21}$ W/cm^2 [1, 2]; it is planned to increase these values by one to two orders of magnitude [3]. In such strong fields, atomic ions with charge $Z \sim 40$–60 will form; the binding energy $E_b = m_e c^2 - E_0$ of electron energy levels in such ions becomes comparable to the rest energy $m_e c^2$. In this case, the tunneling electron motion leading to the ionization can no longer be regarded as nonrelativistic, and the generalization of the Keldysh ionization theory [4–8] is required (this is the subject of this communication). Below, the equations defining the underbarrier trajectory in a wave field and the ionization rate of the *s* level are written for all values of the adiabaticity parameter γ. The case of ionization by a low-frequency laser field ($\gamma \ll 1$), important for applications, is considered and some critical remarks concerning the recently published article [9] are also made.

In our calculations, we will use the imaginary-time method (ITM) providing a pictorial description of the tunneling process, especially in the case of passage through a time-varying barrier [6–8]. As a rule, henceforth $\hbar = m_e = c = 1$.

2. A plane electromagnetic wave with linear polarization is defined by the potentials

$$\mathbf{A} = \left(0, -\frac{\mathscr{E}_0}{\omega} a(\eta), 0\right), \quad \varphi \equiv 0, \tag{1}$$

where $\mathscr{E}_0$ is the wave-field amplitude, $\mathscr{E} = \mathscr{H} = \mathscr{E}_0 a'(\eta)$, $\eta = \omega(t - x)$, the x axis is chosen along the wave-propagation direction, the electric field is directed along the y axis, and the magnetic field is directed along the z axis. The function $a(\eta)$ defines the pulse shape. For example, $a(\eta) = \sin\eta$ corresponds to the monochromatic laser light, $a(\eta) = \eta$ corresponds to a constant crossed field, $a(\eta) = \tanh\eta$ corresponds to a soliton-like pulse $\mathscr{E}(t, x) = \mathscr{E}_0/\cosh^2\eta$, and so on. The equations of motion for the electron 4-momentum $p^i = (\mathbf{p}, E)$ have the form

$$\begin{aligned} \dot{p}_x &= e\mathscr{E} v_y, \quad \dot{p}_y = e\mathscr{E}(1 - v_x), \\ \dot{p}_z &= 0, \quad \dot{E} = e(\mathscr{E}\mathbf{v}) = e\mathscr{E} v_y, \end{aligned} \tag{2}$$

where the dot denotes the derivative with respect to the laboratory time t. For any dependence $\mathscr{E}(\eta)$, there exists an integral of motion [5]

$$J = E - p_x = (1 - v_x)/\sqrt{1 - v^2} = \eta/\omega\tau, \tag{3}$$

where $\tau = \int^t \sqrt{1 - v^2}\, dt$ is the particle intrinsic time. The second equation in Eqs. (2) gives

$$\frac{dp_y}{d\eta} = \frac{e\mathscr{E}_0}{\omega} a'(\eta), \quad p_y(\eta) = \frac{e\mathscr{E}_0}{\omega} a(\eta) = -eA_y(\eta) \tag{4}$$

(while choosing the integration constant, we took into account that the light-front variable η and the momentum p_y become purely imaginary quantities after the transition to the imaginary time, $t \longrightarrow it$; cf. [10–12]). Next, we find that

$$\frac{dy}{d\eta} = \frac{1}{J\omega}\frac{dy}{d\tau} = \frac{p_y(\eta)}{J\omega}, \quad y(\eta) = \frac{e\mathscr{E}_0}{J\omega^2}\int_{\eta_0}^{\eta} a(\eta')d\eta', \tag{5}$$

and the quantities $p_x(\eta)$ and $x(\eta)$ are defined analogously. Note that the solution can be obtained in the explicit form for any wave-field dependence on η.

The explicit form of the tunnel trajectory for monochromatic laser radiation in the case $a(\eta) = \sin\eta$ is

$$p_x(\eta) = \frac{1}{4\beta^2 J}\left(\frac{\sinh 2\eta_0}{2\eta_0} - \cosh 2\eta\right),$$
$$p_y(\eta) = i\beta^{-1}\sinh\eta,$$
$$x = \frac{i\eta}{4\omega\beta^2 J^2}\left(\frac{\sinh 2\eta_0}{2\eta_0} - \frac{\sinh 2\eta}{2\eta}\right), \quad (6)$$
$$y = \frac{1}{\omega\beta J}(\cosh\eta_0 - \cosh\eta), \quad z \equiv 0,$$

where $\beta = \omega/e\mathscr{E}_0$ and the substitution $\eta \longrightarrow i\eta$ corresponding to the ITM is made. Here, $\eta_0 = -i\omega t_0$, where t_0 is the initial (imaginary) instant of time for the tunneling motion.

The quantities η_0 and J appearing in Eqs. (6) can be determined from the initial condition [8, 10]

$$E(\eta_0) = \sqrt{p_x^2 + p_y^2 + 1} = \epsilon, \quad p_x(\eta_0) = \epsilon - J \quad (7)$$

(here, $\epsilon = E_0/m_e c^2$, $0 < \epsilon < 1$, and E_0 is the initial energy of the energy level, including the electron rest energy); this gives

$$\sinh^2\eta_0 = \gamma^2\frac{1 - 2\epsilon J + J^2}{1 - \epsilon^2},$$
$$\frac{\sinh 2\eta_0}{2\eta_0} = 1 + 2\gamma^2\frac{1 - J^2}{1 - \epsilon^2}, \quad (8)$$

where γ is the adiabaticity parameter, which is a relativistic generalization of the well-known Keldysh parameter [4]

$$\gamma = \omega T_t = \frac{\omega}{e\mathscr{E}_0}\sqrt{1 - \epsilon^2}, \quad (9)$$

and T_t is the characteristic tunneling time in electric field $\mathscr{E}_0$. Equations (7) and (8) are used to determine η_0 and J as functions of the parameters γ and ϵ.

By calculating the "truncated action" function [8]

$$W = \int_{t_0}^{0}\{-\sqrt{1 - v^2} + e(\mathbf{Av}) + \epsilon\}dt$$
$$= \int_0^{\tau_0}\left\{1 - e(\mathbf{Ap}) - \frac{\epsilon}{\sqrt{1 - v^2}}\right\}d\tau$$

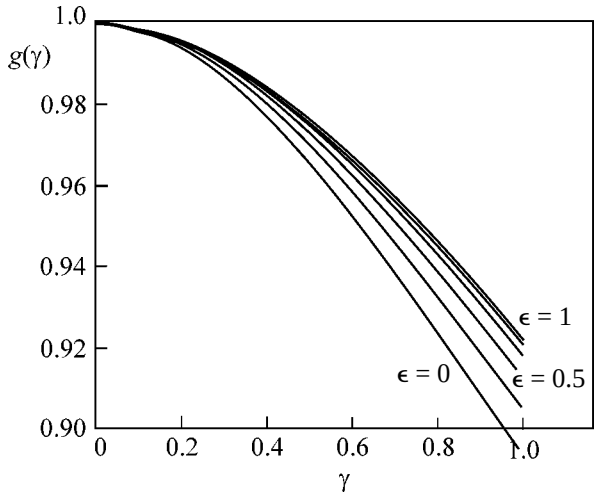

Fig. 1. Functions $g(\gamma, \epsilon_0)$ from formula (11) for monochromatic light (linear polarization). The curves correspond to the initial energy $\epsilon \longrightarrow 1$ (nonrelativistic case), 0.9, 0.75, 0.5, 0.25, and 0 (from top to bottom).

along the tunnel trajectory, we obtain the ionization rate of the relativistic bound state with an exponential accuracy,

$$w_R \propto \exp(-2\hbar^{-1}\mathrm{Im}\,W) = \exp\left\{-\frac{2m_e c^2}{\hbar\omega}\eta_0(J - \epsilon)\right\} \quad (10)$$

or

$$w_R \propto \exp\left\{-\frac{2}{3F}g(\gamma, \epsilon)\right\}, \quad (11)$$

where $g = \left(\sqrt{1 + \frac{2}{3}\xi^2 - \frac{1}{3}\xi^4}/\xi^2\gamma\right)\eta_0(J - \epsilon)$, $\mathscr{E}_S = m_e^2 c^3/e\hbar = 1.32 \times 10^{16}$ V/cm is the so-called Schwinger field, characteristic of QED [13, 14], $F = \mathscr{E}_0/\mathscr{E}_{\mathrm{ch}}$, and the characteristic field defined by the initial energy of the level is introduced:

$$\mathscr{E}_{\mathrm{ch}} = \frac{(\sqrt{3}\xi)^3}{1 + \xi^2}\mathscr{E}_S, \quad \xi = \left[1 - \frac{1}{2}\epsilon(\sqrt{\epsilon^2 + 8} - \epsilon)\right]^{1/2}. \quad (12)$$

The value of $\mathscr{E}_{\mathrm{ch}}$ increases monotonically with decreasing ϵ, i.e., with increasing level depth. In the nonrelativistic limit, $\mathscr{E}_{\mathrm{ch}} = (2I)^{3/2}\mathscr{E}_a$, where $\mathscr{E}_a = \alpha^3\mathscr{E}_S$, $\alpha = 1/137$, and I is the ionization potential (in atomic units). In this case, relation (11) transforms into the well-known Keldysh formula [4, 15]. Equations (8)–(11) generalize this formula to the case of deep levels and can easily be solved by computer methods (Fig. 1).

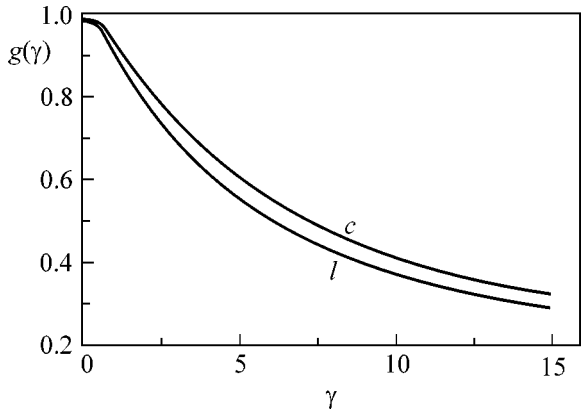

Fig. 2. Function $g(\gamma)$ in the case of linear and circular polarization (curves *l* and *c*, respectively) for a hydrogen-like atom with $Z = 60$.

Analogously, we can calculate the level ionization rate by a wave with elliptic polarization (general case of monochromatic radiation).[1] Instead of system (8), we obtain the equations

$$\begin{aligned}\sinh^2\eta_0 - \rho^2(\cosh\eta_0 - \sin\eta_0/\eta_0)^2 \\ = \gamma^2[1 + (J-\epsilon)^2/(1-\epsilon^2)], \\ (1-\rho^2)\sinh 2\eta_0/2\eta_0 + \rho^2[2(\sinh\eta_0/\eta_0)^2 - 1] \\ = 1 + 2\gamma^2(1-J^2)/(1-\epsilon^2),\end{aligned} \tag{13}$$

where ρ is the light ellipticity ($-1 \le \rho \le 1$, $\rho = 0$ corresponds to linear polarization and $\rho = \pm 1$ corresponds to circular polarization). In this case, formula (10) remains valid for $\mathrm{Im}W$; however, the quantities η_0 and J should now be determined from Eqs. (13). These equations are simplified in the case of linear (see Eq. (8)) and circular polarizations, when $\rho^2 = 1$ and

$$\begin{aligned}(\sinh\eta_0/\eta_0)^2 &= 1 + \gamma^2\frac{1-J^2}{1-\epsilon^2}, \\ \sinh 2\eta_0/2\eta_0 &= 1 + \gamma^2\frac{1-\epsilon J}{1-\epsilon^2}.\end{aligned} \tag{14}$$

Numerical calculation gives for function g the curves depicted in Fig. 2. With increasing ellipticity, function $g = g(\gamma, \epsilon, \rho)$ monotonically increases and the ionization probability accordingly decreases; in other words, we have qualitatively the same situation as in the nonrelativistic case [6].

[1] In this case, the equations of motion are used in the ITM. A more elegant method for solving this problem is associated with the application of the intrinsic-time method developed in Fock's remarkable paper [16]. The application of Fock's method makes it possible to consider the general case of a wave with elliptic polarization and leads to Eqs. (13); however, this requires a special consideration.

After rather cumbersome calculations, Eqs. (10) and (13) lead to the expansion

$$g(\gamma, \epsilon, \rho) = 1 - \frac{1-\rho^2/3}{10(1-\xi^2/3)}\gamma^2 + O(\gamma^4), \tag{15}$$

which is valid in the adiabatic region $\gamma \ll 1$ (for $\gamma \lesssim 0.5$, this expression has an accuracy of a few percent). In the nonrelativistic limit, when $\xi \sim \alpha\sqrt{I} \ll 1$, this formula is in accord with [6] for an arbitrary ellipticity ρ, while in the case of circular polarization, it fits to the result obtained in [5, 6]. Equation (15) directly shows that the increase in light ellipticity reduces the ionization probability w_R; conversely, a decrease in ϵ, i.e., increase in the depth of a bound level, increases this probability (for a fixed value of reduced field F, which is itself a function of the level energy).

3. The exponential factor in Eq. (11) is independent of the particle spin. In the framework of the ITM, the spin correction to the action function is given by [17]

$$\begin{aligned}\delta S_{\mathrm{spin}} &= \frac{ie}{2mc}\epsilon_{\alpha\beta\lambda\mu}\int F^{\alpha\beta}u^\lambda s^\mu d\tau \\ &= \frac{e}{mc}\int\{(\mathbf{sH}) - (\mathbf{vs})(\mathbf{vH}) + [\mathbf{vs}]\mathscr{E}\}dt.\end{aligned} \tag{16}$$

Considering that the tunnel trajectory (6) lies in the (x, y) plane and $\mathscr{E} = \mathscr{H}$, we obtain

$$\begin{aligned}\delta S_{\mathrm{spin}} &= \frac{e\mathscr{E}_0}{mc}\int_{t_0}^{0} s_x a'(\eta)(1 - v_x)dt \\ &= -\frac{e\mathscr{E}_0 J}{mc}\int_0^{\eta_0} s_x a'(\eta)d\tau.\end{aligned} \tag{17}$$

Spin rotation in a uniform external field is described by the Bargmann–Michel–Telegdi equation [18]; for crossed fields, this equation implies that $s_z(t) = \mathrm{const}$ and

$$\delta S_{\mathrm{spin}} = -\mu_B\frac{\mathscr{E}_0}{\omega}s_z a(i\eta_0). \tag{17'}$$

In the case of a constant field, we have $a(i\eta_0) = i\frac{\omega}{e\mathscr{E}_0}\sqrt{\frac{3\xi^2}{(1+\xi^2)}}$; in addition, we must also take into account the change in the exponential factor in Eq. (11) owing to the splitting of level ϵ_0 in a magnetic field, because this factor contains magnetic moment μ of a bound electron, which differs from the Bohr magneton if $Z\alpha \sim 1$ [19, 20]. As a result, we obtain the spin factor in the level ionization rate in a constant crossed field:

$$S_\pm^{\mathrm{ITM}} = \exp\left\{\pm\frac{\sqrt{3}\xi}{\sqrt{1+\xi^2}}(1 - \mu/\mu_B)\right\}, \tag{18}$$

where the signs $\pm\hbar/2$ correspond to the spin projections onto the direction of $\mathcal{H}$; for this reason, the states with different values of s_z are characterized by different ionization rates.

An alternative method for calculating spin correction to the action is based on squaring the Dirac equation. This approach is similar to that used in [21, 22] for the relativistic Coulomb problem with $Z > 137$. In this case, instead of Eq. (17), we obtain

$$S_+ = \frac{1+\sigma}{1-\sigma}\exp\left(-\frac{\sqrt{3}\xi}{\sqrt{1+\xi^2}}\frac{\mu}{\mu_B}\right), \quad \sigma = \frac{\sqrt{3}\xi}{1+\sqrt{1+\xi^2}}, \quad (18')$$

and $S_- = 1/S_+$. Expressions (18) and (18') are close numerically. According to Breit [19], for example, we have $\mu = 0.933\,\mu_B$ for the $1s_{1/2}$ ground level in a hydrogen-like atom with charge $Z = 60$, whence $S_+ = 1.046$ and S_+^{ITM} differs from it by only 1.5%; for $Z = 92$, we have $S_+ = 1.121$, and so on. Thus, the results of these two (independent) calculations virtually coincide.

For $Z\alpha \ll 1$, we have $S_\pm \approx S_\pm^{\mathrm{ITM}} = 1 + O((Z\alpha)^3)$; i.e., the tunneling probability is independent of the electron spin projection. This is not surprising since operator s commutes with the Schrödinger Hamiltonian and the spin component splits off.

4. Maximal intensities J are attained for IR lasers; for this reason, the case with $\gamma \ll 1$ deserves special consideration. For the tunneling ionization rate of the s level, we can derive an asymptotically exact formula in the limit of a weak ($\mathcal{E}_0 \ll \mathcal{E}_{\mathrm{ch}}$, or $F \ll 1$) field:

$$w_R = \frac{E_b}{\hbar}|C_\lambda|^2 D F^{-(2\nu-3/2)} \times \exp\left\{-\frac{2}{3F}\left(1-\frac{\gamma^2}{10(1-\xi^2/3)}\right)\right\}, \quad \rho = 0, \quad (19)$$

where $E_b = mc^2(1-\epsilon)$ is the binding energy of the level, $\nu = Z\alpha\epsilon/\sqrt{1-\epsilon^2}$ is the relativistic analogue of the effective principal quantum number $n^* = Z/\sqrt{2I}$, and C_λ is an asymptotic (at infinity) coefficient of the free-atom wave function (in the absence of the wave field). Generally speaking, this coefficient can be obtained only numerically from the Hartree–Fock–Dirac equations; however, for a hydrogen-like atom, there exists an analytic solution (see, e.g., [23]). For example, for the $1s_{1/2}$ ground level and any Z, we have

$$\epsilon = \nu = \sqrt{1-(Z\alpha)^2}, \quad C_{1s}^2 = 2^{2\epsilon-1}/\Gamma(2\epsilon+1). \quad (20)$$

Finally, the factor $D = D(\epsilon, Z)$ is independent of the wave amplitude and has a rather cumbersome form, and it will not be given here. It should be noted that the Coulomb factor Q [11] arising when the Coulomb interaction between an electron and the atomic core (with charge Z) is taken into account is calculated using the semiclassical perturbation theory [7]. For the elliptic radiation polarization, the exponential factor in Eq. (19) should be replaced in accordance with Eq. (15), while the field index F (in the preexponential factor) in the case of circular polarization should be replaced by $1 - 2\nu$.

In the nonrelativistic limit, Eq. (19) assumes the form

$$w = \kappa^2 C_\kappa^2 \sqrt{\frac{3F}{\pi}} 2^{2n^*} F^{1-2n^*} \exp\left\{-\frac{2}{3F}\left(1-\frac{1}{10}\gamma^2\right)\right\}, \quad (21)$$

where we now have $F = \mathcal{E}_0/\kappa^3$, $\gamma = \omega\kappa/\mathcal{E}_0$ is the Keldysh parameter, $\kappa = \sqrt{2I}$, and atomic units are used (in the case of circular polarization, we must omit factor $\sqrt{3F/\pi}$ and replace coefficient 1/10 in the exponent by 1/15). The generalization of formula (21) to the states with an arbitrary orbital angular momentum l is given in [6].

Let us assess the range of application of the nonrelativistic theory of ionization. With an exponential accuracy, we obtain from Eqs. (11) and (21)

$$w_R \propto \exp\{-2(\sqrt{3}\xi)^3\mathcal{E}_S/3(1+\xi^2)\mathcal{E}_0\}, \quad (22)$$

$$w_{NR} \propto \exp\left\{-\frac{2\kappa^3\mathcal{E}_a}{3\mathcal{E}_0}\right\} = \exp\left\{-\frac{2}{3}[2(1-\epsilon)]^{3/2}\frac{\mathcal{E}_S}{\mathcal{E}_0}\right\}. \quad (22')$$

Setting here $\epsilon = 1 - \frac{1}{2}\alpha^2\kappa^2 = \sqrt{1-(Z\alpha)^2}$ and taking into account the expansions

$$\kappa = Z\left[1+\frac{1}{8}(Z\alpha)^2+\ldots\right],$$

$$\sqrt{3}\xi = \alpha\kappa + \frac{7}{72}(\alpha\kappa)^3 + \ldots = Z\alpha + \frac{2}{9}(Z\alpha)^3 + \ldots,$$

we obtain

$$w_{NR}/w_R \approx \exp\left\{-\frac{1}{36}(Z\alpha)^5\frac{\mathcal{E}_S}{\mathcal{E}_0}\right\}, \quad Z\alpha \ll 1. \quad (23)$$

It can be seen that the range of applicability of the Keldysh nonrelativistic theory is "extended" to quite large values of Z. For example, for $Z = 40$, 60, and 80 and for the radiation intensity $J = 10^{23}$ W/cm^2, the values of w_{NR} and w_R differ by a factor of 1.15, 3, and 65, respectively. Using the formulas derived above, we can easily refine this estimate and make it more exact (Fig. 3). For want of space, we postpone the discussion of this question to a more detailed publication.

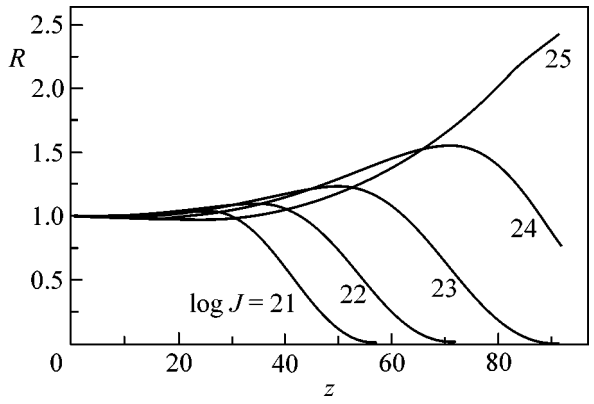

Fig. 3. The ratio $R = w_{NR}/w_R$ for the $1s_{1/2}$ ground level as a function of Z for various intensities of laser radiation. The figures on the curves indicate the values of $\log J$ [W/cm^2].

The ionization of a relativistic bound state by a constant crossed field was considered by Nikishov and Ritus [5]. Using the Klein–Gordon equation, they calculated the ionization probability w_R for the s level bound by short-range forces ($Z = 0$) in the case of a particle with zero spin. For $Z = \nu = 0$, expressions (19), (22), and (25) coincide with those obtained in [5], but they are written in a more compact form. The coincidence of the results obtained by two independent methods is very important for the ITM. Although this method possesses a heuristic potential and physical clearness, it cannot be regarded as rigorously substantiated, in spite of some attempts made in this direction [17].

5. In conclusion, we must consider the article by Milosevic, Krainov, and Brabec "Semiclassical Dirac Theory of Tunnel Ionization" [9], which contains formula (8) for the ground-state ionization rate w_r in constant crossed fields. This formula (which is treated in [9] as the "main result" of that study) can easily be written in the form

$$w_r = C_\lambda^2 P \overline{Q} \mathrm{Exp}, \quad \hbar = m = c = 1, \qquad (24)$$

where the factors Exp and P identically coincide with the corresponding expressions from [5, 10, 11],

$$\mathrm{Exp} = \exp\left(-\frac{2\sqrt{3}\xi^3}{1+\xi^2}\frac{\mathscr{E}_S}{\mathscr{E}}\right), \quad P = \frac{1}{\xi}\sqrt{\frac{1-\xi^2/3}{3+\xi^2}}\frac{\mathscr{E}}{\mathscr{E}_S}, \qquad (25)$$

while the Coulomb factor $\overline{Q}$ differs from our expression (formula (35) in [11]) only in that the exponent $\eta \equiv \nu = Z\alpha\epsilon/\sqrt{1-\epsilon^2}$ is replaced by the level energy ϵ. The difference between Q and $\overline{Q}$ is due to the fact that, in [9], a special case of ionization of the $1s_{1/2}$ level with energy $\epsilon = \sqrt{1-(Z\alpha)^2}$ was considered and the wave function had the simplest form [23]. This can be done if the atom has only one electron in the K shell, while the remaining electrons are stripped (hydrogen-like atom with nuclear charge Z). In this particular case, $\eta \equiv \epsilon$ and $\overline{Q} \equiv Q$, while the asymptotic coefficient is defined by formula (20) and corresponds to [9]. However, our formula for Q is considerably more general; it applies to multicharged ions with an arbitrary degree of ionization if the atomic-level parameters ϵ and C_λ^2 are taken from independent calculations for a free ($\mathscr{E} = \mathscr{H} = 0$) atom or directly from the experiment, as in the nonrelativistic theory of ionization [5–8].

In [9], neither spin factor (18) in the tunneling probability nor correction (15) on the order of γ^2 in the exponent were calculated and the adiabatic correction [6] changing the power of field in the preexponential factor was not taken into account. For this reason, formula (8) from [9] could refer only to constant fields. However, in this case the authors of [9] assume, in fact, that the Dirac bispinor $\hat{S}$ defined in the vicinity of atomic nucleus does not change in the course of electron tunnel motion (this obviously follows from the comparison of formulas (1), (2), and (5) in [9]), which is not correct. The word combination "Dirac theory" appearing in the title of [9] is also surprising since it is only the normalization factor C_λ^2 mentioned in all textbooks on quantum mechanics [23] (which, in addition, differs from unity by only a few percent; e.g., $C_\lambda^2 = 1$ for small Z and $C_\lambda^2 = 1.039$ for $Z = 60$) that is related to the Dirac theory, while the factors P, Q, and Exp are independent of the particle spin and can be calculated on the basis of the Klein–Gordon equation, as in [5, 10–12].

The formulas given in [9] literally reproduce the corresponding formulas[2] from [10–12] with the same notation (including the transition from the energy ϵ to the convenient variable ξ introduced in [10] and naturally arising in the ITM). The original contribution of the authors of [9] lies in the multiplication of factors Exp, Q, P, and C_λ^2, which were previously known. Thus, article [9] is a compilation of the studies [10–12] carried out (and published) several years earlier (which, however, is not mentioned in [9]). At the same time, it is stated in [9] that "*for the first time* a quantitative description of tunnel ionization of atomic ions" or "*the first quantitative determination* of tunneling in atomic ions in relativistic regime" is given in that work (italicized by us); see abstract and the text preceding formula (9) in [9].

Reference [11] in [9] shows that our publications were familiar to the authors. However, our studies are treated as the "analytic solution of the Klein–Gordon

[2] See, for example, Eqs. (17), (35), and (50) in [11]. While comparing these formulas with formula (8) from [9], it should be borne in mind that $eF \equiv \mathscr{E}/F_{cr}$, $F_{cr} \equiv \mathscr{E}_S = 1/e$, and $\mu = Z\alpha$ (for $\hbar = m = c = 1$).

equation for π^- atoms in static electric and magnetic fields," although we never mentioned π^- atoms.[3] On the contrary, it is repeatedly emphasized in [10–12] that our goal is the generalization of the imaginary time method to the case of relativistic tunnel electron motion and its application to the theory of ionization of deep levels (including the *K* shell) in heavy atoms.

One of the authors of this paper (V.P.) was obliged to note (in connection with the so-called ADK theory [24]; see [25] for details) a certain tendency to use the results obtained by other authors without the appropriate citation. The "main result" in [9] was obtained by simply rewriting the formulas from original publications [5, 10–12].

We are grateful to M.I. Vysotskii, S.P. Goreslavskii, V.R. Zoller, N.B. Narozhnoi, L.B. Okun', S.V. Popruzhenko, Yu.A. Simonov, and also to participants of the 17th Conference on Fundamental Atomic Spectroscopy (Zvenigorod, December 2003) and Scientific Conference MIFI-2004 (Moscow, January 2004) for fruitful discussions, valuable remarks, and moral support. We thank S.G. Pozdnyakov, who carried out numerical calculations, and N.S. Libova and M.N. Markina for the help in preparing the manuscript.

This study was supported in part by the Russian Foundation for Basic Research (project no. 01-02-16850).

REFERENCES

1. G. Mourou, C. P. J. Barty, and M. D. Perry, Phys. Today **51** (1), 22 (1998).
2. T. Brabec and F. Krausz, Rev. Mod. Phys. **72**, 545 (2000).
3. T. Tajima and G. Mourou, Phys. Rev. ST Accel. Beams **5**, 031301 (2002).
4. L. V. Keldysh, Zh. Éksp. Teor. Fiz. **47**, 1945 (1964) [Sov. Phys. JETP **20**, 1307 (1964)].
5. A. I. Nikishov and V. I. Ritus, Zh. Éksp. Teor. Fiz. **50**, 255 (1966) [Sov. Phys. JETP **23**, 168 (1966)]; Zh. Éksp. Teor. Fiz. **52**, 223 (1967) [Sov. Phys. JETP **25**, 145 (1967)].
6. A. M. Perelomov, V. S. Popov, and M. V. Terent'ev, Zh. Éksp. Teor. Fiz. **50**, 1393 (1966) [Sov. Phys. JETP **23**, 924 (1966)]; Zh. Éksp. Teor. Fiz. **51**, 309 (1966) [Sov. Phys. JETP **24**, 207 (1966)].
7. A. M. Perelomov and V. S. Popov, Zh. Éksp. Teor. Fiz. **52**, 514 (1967) [Sov. Phys. JETP **25**, 336 (1967)].
8. V. S. Popov, V. P. Kuznetsov, and A. M. Perelomov, Zh. Éksp. Teor. Fiz. **53**, 331 (1967) [Sov. Phys. JETP **26**, 222 (1968)].
9. N. Milosevic, V. P. Krainov, and T. Brabec, Phys. Rev. Lett. **89**, 193001 (2002).
10. V. S. Popov, B. M. Karnakov, and V. D. Mur, Pis'ma Zh. Éksp. Teor. Fiz. **66**, 213 (1997) [JETP Lett. **66**, 229 (1997)]; V. S. Popov, V. D. Mur, and B. M. Karnakov, Phys. Lett. A **250**, 20 (1998).
11. V. D. Mur, B. M. Karnakov, and V. S. Popov, Zh. Éksp. Teor. Fiz. **114**, 798 (1998) [JETP **87**, 433 (1998)].
12. B. M. Karnakov, V. D. Mur, and V. S. Popov, Yad. Fiz. **62**, 1444 (1999) [Phys. At. Nucl. **62**, 1363 (1999)].
13. W. Heisenberg and H. Euler, Z. Phys. **98**, 714 (1936).
14. J. Schwinger, Phys. Rev. **82**, 664 (1951).
15. L. D. Landau and E. M. Lifshitz, *Course of Theoretical Physics*, Vol. 3: *Quantum Mechanics: Non-Relativistic Theory*, 3rd ed. (Nauka, Moscow, 1974; Pergamon, New York, 1977).
16. V. A. Fok, Izv. Akad. Nauk SSSR, Ser. Fiz. **4–5**, 551 (1937).
17. M. S. Marinov and V. S. Popov, Yad. Fiz. **15**, 1271 (1972) [Sov. J. Nucl. Phys. **15**, 702 (1972)].
18. V. Bargmann, L. Michel, and V. L. Telegdi, Phys. Rev. Lett. **2**, 435 (1959).
19. G. Breit, Nature **122**, 649 (1928).
20. A. M. Perelomov and V. S. Popov, Yad. Fiz. **14**, 661 (1971) [Sov. J. Nucl. Phys. **14**, 370 (1971)].
21. V. S. Popov, Yad. Fiz. **12**, 429 (1970) [Sov. J. Nucl. Phys. **12**, 235 (1970)]; Yad. Fiz. **14**, 458 (1971) [Sov. J. Nucl. Phys. **14**, 257 (1971)]; Yad. Fiz. **64**, 421 (2001) [Phys. At. Nucl. **64**, 367 (2001)].
22. Ya. B. Zel'dovich and V. S. Popov, Usp. Fiz. Nauk **105**, 403 (1971) [Sov. Phys. Usp. **14**, 673 (1971)].
23. L. I. Schiff, *Quantum Mechanics*, 3rd ed. (McGraw-Hill, New York, 1968; Inostrannaya Literatura, Moscow, 1957).
24. M. V. Ammosov, N. B. Delone, and V. P. Kraĭnov, Zh. Éksp. Teor. Fiz. **91**, 2008 (1986) [Sov. Phys. JETP **64**, 1191 (1986)]; N. B. Delone and V. P. Kraĭnov, Usp. Fiz. Nauk **168**, 531 (1998) [Phys. Usp. **41**, 487 (1998)].
25. V. S. Popov, Usp. Fiz. Nauk **169**, 819 (1999) [Phys. Usp. **42**, 733 (1999)].

Translated by N. Wadhwa

[3] To ionize π^- atoms, the electric field strength should be increased by five orders of magnitude (since $\mathscr{E}_S \propto m^2$) to attain intensities $J \gtrsim 10^{23}$ W/cm^2, which is far beyond the limits of the wildest fantasies and can hardly be realized in principle due to the production of e^+e^- pairs from vacuum by an external field (Schwinger effect [14]).

JETP Letters, Vol. 79, No. 6, 2004, pp. 268–271. Translated from Pis'ma v Zhurnal Éksperimental'noĭ i Teoreticheskoĭ Fiziki, Vol. 79, No. 6, 2004, pp. 326–329.

Experimental Study of the Resonance Radiation Group Delay in Degenerate Systems

R. A. Akhmedzhanov and I. V. Zelensky*

Institute of Applied Physics, Russian Academy of Sciences, ul. Ul'yanova 46, Nizhni Novgorod, 603950 Russia

**e-mail: zelensky@appl.sci-nnov.ru*

Received February 12, 2004

The dependence of the polarization- and intensity-modulation group delay on the polarization of electromagnetic wave was studied experimentally for different transitions between the hfs components of the ^{87}Rb D_1 absorption line. It was found that the polarization-modulation delay strongly depends on the degeneracy structure of resonant transition and, in the general case, on the ellipticity of light-wave polarization. It is demonstrated that the polarization-modulation delay does not occur for the transitions not involving dark states. The polarization delay was studied as a function of the polarization ellipticity angle. The intensity-modulation delay was measured for the resonance radiation to show that it is observed for all ^{87}Rb D_1-line transitions and is independent of polarization. © *2004 MAIK "Nauka/Interperiodica".*

PACS numbers: 42.25.Ja; 42.50.Gy

The discovery of coherent population trapping (CPT) and electromagnetically induced transparency (EIT) has stimulated the study of resonance nonlinear effects in media with induced atomic coherence [1–3]. The appearance of a transparency window upon the resonant wave-field interaction in multilevel systems is accompanied by the appreciable lengthening of laser radiation path. The strong medium dispersion under the EIT conditions brings about anomalously strong delay of a signal pulse in the pump-wave field. For the special radiation-controlled regime, "light stop," i.e., in fact, implementation of optical memory, is possible [4, 5]. The combination of a low velocity of wave-packet propagation and increase in the wave-interaction path under resonance conditions renders the EIT regime promising for the observation of various nonlinear effects.

Degenerate schemes have gained the widest acceptance in the implementation of the CPT and EIT effects. This is caused by both the widespread occurrence of the degenerate systems and their obvious advantages. In particular, due to the fact that the frequencies of the fields used in these schemes are equal in the case of exact resonance, the Doppler broadening of the EIT-inducing two-photon transition can be reduced, in effect, to zero, and, in addition, the possibility of using a common generation source for the interacting waves allows the coherence of excitation events to be substantially improved. For this reason, degenerate systems prove to be suitable for the observation of EIT and, therefore, are widely used in experiment. In particular, the so-called light stop was observed for the ^{87}Rb $5s_{1/2}$, $F = 2 \longrightarrow 5p_{1/2}$, $F = 1$ transition [4]. It should also be noted that the EIT phenomenon in the systems with magnetic quantum number degeneracy is suggested for use in magnetic-field measurements [6–9].

The CPT in degenerate systems is caused by the polarization-induced separation of excitation channels. In such a situation, the behavior of the system depends on the mutual orientation of the polarizations of optical fields. The population trapping occurs in the so-called dark state representing a sublevel superposition noninteracting with field. The occurrence of a dark state and the population trapping in this state are the common property of degenerate systems and are well understood. In particular, the CPT in a magnetically degenerate two-level system interacting with a polarized radiation was studied in detail in the early works devoted to the theory of this phenomenon [10, 11].

For the EIT in degenerate systems, the traditional scheme of studying the behavior of a weak signal wave in the field of an intense pump wave becomes conventional, because the corresponding wave polarizations are chosen arbitrarily. In theoretical work [12], a general approach was suggested to the study of the evolution of a wave with slowly varying polarization interacting resonantly with a medium of degenerate atoms under CPT conditions. It has been shown that a change in the light-wave polarization propagates through such a medium with a group velocity that is much lower than the velocity of light and dependent on the wave polarization and the transition type.

Another effect inherent in multilevel systems consists in the delay of a change in the intensity of a resonant light wave as a result of population pumping out to the long-lived levels noninteracting with field [13]. Evi-

dently, a dark state can play the role of such level in degenerate systems.

In this work, the group delay of a change in polarization and intensity was studied as a function of the electromagnetic-wave polarization for different transitions between the hfs components of the ^{87}Rb D_1 absorption line. To reduce the influence of disturbing factors such as spurious magnetic fields, measurements were performed in a pure rubidium vapor without a buffer gas and with a relatively high laser intensity (100 mW/cm^2) [8]. The delay times under these conditions were relatively short (0.5–2 μs, which corresponds to a mean group velocity of 25–100 km/s) but sufficient for the measurements of their dependence on polarization.

The scheme of the experimental setup for studying the group delay of a change in polarization is presented in Fig. 1a. An external cavity diode laser 1 was used as a source of monochromatic radiation. The radiation was linearly polarized at the laser output. The polarization was additionally controlled by polarizer 2. The light-wave polarization was varied from linear to circular using a Pockels cell 3 and modulated about its mean value with a frequency of ~60 kHz and a modulation depth of ~10%. A laser beam with a cross section of 2×5 mm passed through a cylindrical cell 4, 56 mm in diameter and 55 mm in length, filled with rubidium vapor. To prevent the influence of the laboratory magnetic field, magnetic screen 8 was used. The rubidium concentration in the cell was varied using heater 9. The signal was detected using the scheme consisting of quarter-wave plate 5, polarizer 6, and photodiode 7. Quarter-wave plate 5 and polarizer 6 could rotate about the axis, allowing the modulation to be detected near the arbitrary elliptic radiation polarization.

Among the hfs transitions of the D_1 absorption line (Fig. 2), the $F = 1 \longrightarrow F' = 2$ transition does not involve a dark state, the $F = 1 \longrightarrow F' = 1$ and $F = 2 \longrightarrow F' = 2$ transitions involve a simple one-dimensional dark state, and the $F = 2 \longrightarrow F' = 1$ transition has a double (two-dimensional) dark state, which is to say that, for every light-wave polarization, the lower-level sublevels have a two-dimensional space noninteracting with the resonant electromagnetic field [10, 11]. Measurements showed that the delay in the propagation of polarization structure is absent for the $F = 1 \longrightarrow F' = 2$ transition. The group delay of a change in polarization was observed for the $F = 1 \longrightarrow F' = 1$ and $F = 2 \longrightarrow F' = 2$ transitions. This delay did not depend on the azimuthal rotation angle of polarization because of the axial symmetry of the system. The delay for the $F = 1 \longrightarrow F' = 1$ transition did not depend on the ellipticity. For the $F = 2 \longrightarrow F' = 2$ transition, the delay of the polarization-modulation propagation was found to be dependent on the mean ellipticity of light-wave polarization; the delay was maximal for the linear polarization and minimal for the circular polarization. These data are in agreement with the theoretical ideas developed in [12].

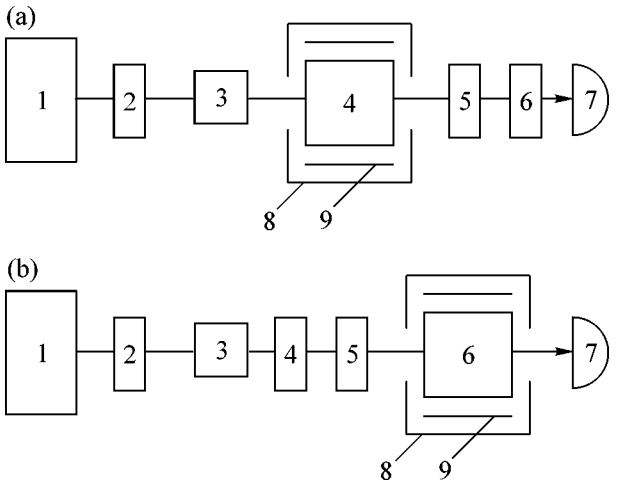

Fig. 1. (a) Scheme of the setup for measuring the polarization-modulation delay: 1 laser, 2 polarizer, 3 Pockels cell, 4 ^{87}Rb vapor cell, 5 quarter-wave plate, 6 polarizer, 7 photodiode, 8 magnetic screen, and 9 heater. (b) Setup for studying the intensity-modulation delay: 1 laser, 2 polarizer, 3 Pockels cell, 4 polarizer, 5 quarter-wave plate, 6 ^{87}Rb vapor cell, 7 photodiode, 8 magnetic screen, and 9 heater.

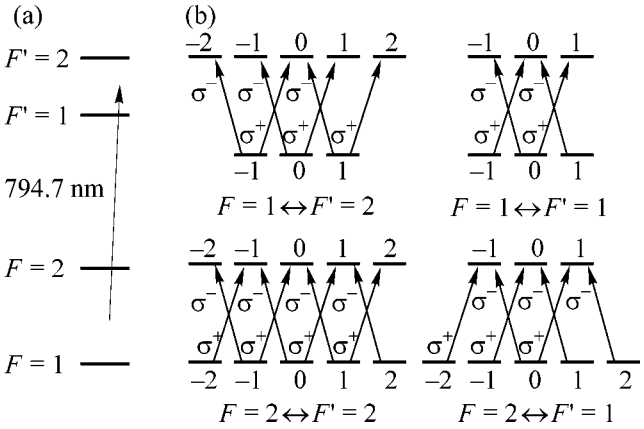

Fig. 2. (a) Hyperfine structure scheme of the ^{87}Rb D_1 line. (b) Transitions between the hfs levels of the ^{87}Rb D_1 line. The magnetic sublevels of the corresponding levels are shown. The magnetic quantum numbers are numbered and the arrows indicate the allowed transitions for the right σ^+ and left σ^- circular polarizations.

The situation with the $F = 2 \longrightarrow F' = 1$ transition proved to be more complicated; in addition to the delay of polarization structure, it changed and the radiation was depolarized. Such a behavior is apparently caused by the complex structure of the dark state of this transition and calls for further analysis. It is worth noting that the polarization modulation with a frequency of 60 kHz and a depth of 10% did not change the absorption at this

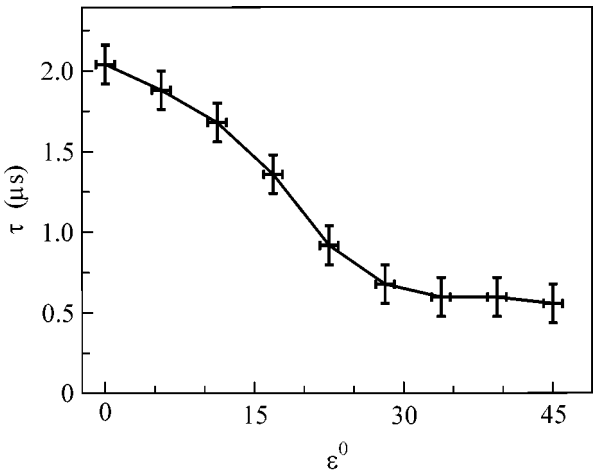

Fig. 3. Dependence of the group delay τ of a change in polarization on the mean ellipticity angle ϵ of the electromagnetic-wave polarization resonant with the $F = 2 \longrightarrow F' = 2$ transition of the ^{87}Rb D_1 absorption line.

transition, indicating the adiabatic character of the dark-state rearrangement in our experiment [3].

The maximal delay in the propagation of polarization structure at the $F = 2 \longrightarrow F' = 2$ transition was observed for a rubidium concentration of $\sim 2 \times 10^{12}$ cm^{-3}. The corresponding dependence of the group delay τ of a change in polarization on the mean ellipticity angle ϵ is shown in Fig. 3. One can see that the delay in the propagation of polarization structure for the linear polarization $\epsilon = 0°$ is more than three times larger than the delay for the circular polarization $\epsilon = 45°$. With an increase in the concentration, the delay decreased, likely due to the radiation trapping, i.e., breaking of atomic coherence in the reemitted light [14–16]. The group delay measured under the same conditions for the polarization structure at the $F = 1 \longrightarrow F' = 1$ transition was independent of the radiation polarization and equal to 0.75 ± 0.10 μs.

Along with the delay of a change in polarization, the delay of a change in the intensity of a resonant light wave, analogous to that observed previously in ruby crystal [13], was also studied in our experiment. The scheme of the setup for studying the intensity-modulation delay is shown in Fig. 1b. The radiation from laser 1 passed through linear polarizer 2 and fell on Pockels cell 3, to which an ac voltage with a frequency of 60 kHz and a bias voltage were applied. Upon passing through polarizer 4, the laser beam acquired linear polarization and amplitude modulation. A quarter-wave plate allowed the radiation polarization to be changed from linear to circular. The radiation passing through a cell with ^{87}Rb vapor inside magnetic screen 8 with heater 9 was detected using photodiode 7. The intensity-modulation delay was studied for the resonant light wave and different transitions between the hfs components of the ^{87}Rb D_1 line.

Our studies showed that the intensity-modulation delays in the polarization-delay experiments (laser intensity ~100 mW/cm^2 and rubidium concentration $\sim 2 \times 10^{12}$ cm^{-3}) did not exceed 0.5 μs for all ^{87}Rb D_1 transitions. Measurements with a higher concentration ($\sim 5 \times 10^{12}$ cm^{-3}) and lower laser intensity (50 mW/cm^2) gave the following results: 1.2 ± 0.2, 0.4 ± 0.2, 1.2 ± 0.2, and 2.0 ± 0.2 μs for the $F = 1 \longrightarrow F' = 2$, $F = 1 \longrightarrow F' = 1$, $F = 2 \longrightarrow F' = 2$, and $F = 2 \longrightarrow F' = 1$ transition, respectively. The small delay for the $F = 1 \longrightarrow F' = 1$ transition is caused by its low oscillator strength (one-fifth of the other transitions). It was found that the intensity-modulation delay is independent of the radiation polarization within the measurement accuracy. Note that the delay of a change in intensity occurs for the $F = 1 \longrightarrow F' = 2$ transition, for which no delay of polarization structure was observed. This is probably due to the population pumping to the $F = 2$ level.

In summary, the polarization- and intensity-modulation group delay have been studied for a light wave interacting resonantly with a medium consisting of degenerate atoms. It has been shown that the evolution of resonance radiation depends on the degeneracy structure of transition. For the transitions not involving a dark state, the polarization modulation was not delayed. For the transitions involving a one-dimensional dark state, the polarization-modulation group delay was observed, much as the electromagnetic-wave propagation is retarded under EIT conditions. In the simplest configuration ($F = 1 \longrightarrow F' = 1$ transition), the polarization delay does not depend on the radiation polarization. For the transitions with a more complex degeneracy structure, the polarization-modulation decay depends on the polarization of a resonant wave. Due to this dependence, the shape of the polarization pulse can be distorted upon its propagation in medium. These results are in close agreement with the conclusions of theoretical work [12]. For the transitions involving a two-dimensional dark state, the delay of polarization structure was accompanied by its change and the radiation depolarization. Evidently, such a behavior is caused by the complex structure of a dark state and calls for further investigation. The delay of a change in the laser-radiation intensity was observed for all the transitions studied. The delay in the propagation of a change in intensity is caused by the population pumping out to the long-lived levels noninteracting with the field. Both the dark state and the long-lived nonresonance levels can play the role of such levels. It should be noted that the delay of a change in intensity does not depend on the polarization and, under analogous conditions, is several times shorter than for the polarization delays.

These results can prove to be important for the solution of various fundamental and applied problems in nonlinear optics and, in particular, the problem of data

storage and processing of optical and, in the future, quantum information.

We are grateful to L.A. Gushchin, A.G. Litvak, and V.A. Mironov for helpful discussions. This work was supported by the Russian Foundation for Basic Research (project nos. 04-02-17042 and 03-02-17176).

REFERENCES

1. B. D. Agap'ev, M. B. Gornyĭ, B. G. Matisov, and Yu. V. Rozhdestvenskiĭ, Usp. Fiz. Nauk **163** (9), 35 (1993) [Phys. Usp. **36**, 763 (1993)].
2. E. Arimondo, Prog. Opt. **35**, 257 (1996).
3. A. B. Matsko, O. Kocharovskaya, Y. Rostovtsev, *et al.*, Adv. At. Mol. Opt. Phys. **46**, 191 (2001).
4. D. F. Phillips, A. Fleischhauer, A. Mair, *et al.*, Phys. Rev. Lett. **86**, 783 (2001).
5. O. Kocharovskaya, Y. Rostovtsev, and M. O. Scully, Phys. Rev. Lett. **86**, 628 (2001).
6. R. Wynands and A. Nagel, Appl. Phys. B **68**, 1 (1999).
7. R. A. Akhmedzhanov and I. V. Zelenskiĭ, Pis'ma Zh. Éksp. Teor. Fiz. **76**, 493 (2002) [JETP Lett. **76**, 419 (2002)].
8. P. N. Anisimov, R. A. Akhmedzhanov, I. V. Zelenskiĭ, and E. A. Kuznetsova, Zh. Éksp. Teor. Fiz. **124**, 973 (2003) [JETP **97**, 868 (2003)].
9. P. M. Anisimov, R. A. Akhmedzhanov, I. V. Zelenskiĭ, *et al.*, Zh. Éksp. Teor. Fiz. **124**, 973 (2003) [JETP **97**, 868 (2003)].
10. V. S. Smirnov, A. M. Tumaĭkin, and V. I. Yudin, Zh. Éksp. Teor. Fiz. **96**, 1613 (1989) [Sov. Phys. JETP **69**, 913 (1989)].
11. A. M. Tumaĭkin and V. I. Yudin, Zh. Éksp. Teor. Fiz. **98**, 81 (1990) [Sov. Phys. JETP **71**, 43 (1990)].
12. I. V. Zelenskiĭ and V. A. Mironov, Zh. Éksp. Teor. Fiz. **121**, 1068 (2002) [JETP **94**, 916 (2002)].
13. M. S. Bigelow, N. N. Lepeshkin, and R. W. Boyd, Phys. Rev. Lett. **90**, 133903 (2003).
14. I. Novikova, A. B. Matsko, and G. R. Welch, Opt. Lett. **26**, 1016 (2001).
15. I. Novikova and G. R. Welch, J. Mod. Opt. **49**, 349 (2002).
16. A. B. Matsko, I. Novikova, M. O. Scully, and G. R. Welch, Phys. Rev. Lett. **87**, 133601 (2001).

Translated by V. Sakun

JETP Letters, Vol. 79, No. 6, 2004, pp. 272–276. Translated from Pis'ma v Zhurnal Éksperimental'noĭ i Teoreticheskoĭ Fiziki, Vol. 79, No. 6, 2004, pp. 330–334.

Self-Action of Laser Radiation under the Conditions of Electromagnetically Induced Transparency

N. A. Zharova*, A. G. Litvak, and V. A. Mironov

Institute of Applied Physics, Russian Academy of Sciences, ul. Ul'yanova 46, Nizhni Novgorod, 603950 Russia

**e-mail: zhani@appl.sci-nnov.ru*

Received January 28, 2004; in final form, February 17, 2004

The laser-radiation self-action dynamics in the electromagnetically induced transparency band were studied analytically and numerically for an atomic gas with the Λ-type energy-level scheme. The self-consistent system of equations describing the spatiotemporal evolution of a finite-amplitude wave packet in the field of a uniform pump wave was derived. The self-action in the presence of competing diffraction, nonlinear dispersion, and radiation absorption in the system was qualitatively analyzed; in particular, the conditions for self-focusing of a probe beam were determined. The results were confirmed by the numerical simulation of wave-packet spatiotemporal evolution. © *2004 MAIK "Nauka/Interperiodica"*.

PACS numbers: 42.50.Gy; 42.65.Jx

The studies of interference phenomena [1–3] of the type of coherent population trapping (CPT) and electromagnetically induced transparency (EIT) in multilevel atomic ensembles have culminated in the intensive development of a new direction in nonlinear resonance optics. It is characterized by a negligible absorption of resonance radiation upon its parametric interaction with a medium. As a result, the traditional nonlinear effects can be observed for exceedingly low intensities of interacting waves (at a level of a few photons) and with less stringent phase-matching requirements.

The quantum interference effects are responsible for some unusual features in the propagation of a bichromatic resonance radiation in a system of three-level atoms. A broad class of self-consistent two-pulse structures were found in a one-dimensional case. In the absence of phase-coherence relaxation in a medium with the Λ-type energy-level scheme, they propagate without any noticeable change in shape at a distance much greater than the absorption length of an individual wave packet (see [4–6] and references cited therein). Of particular interest is the study of stationary self-action (self-focusing) of the bichromatic radiation [7–10] in a medium with EIT.

In this work, the self-action dynamics are considered for spatially restricted laser pulses under the EIT conditions in a medium of Λ-type atoms. The density matrix formalism is used to obtain a self-consistent system of equations describing the self-action dynamics of a bichromatic radiation in a system with long-lived phase coherence. The spatiotemporal evolution of a finite-amplitude wave packet in the field of a strong pump wave is qualitatively examined and the conditions under which the radiation self-focusing is possible are determined. The results of qualitative consideration are confirmed by the numerical simulation of self-action dynamics.

1. Let us consider the spatiotemporal evolution of the bichromatic laser radiation

$$E = E_1(\mathbf{r}_\perp, z, t)\exp(i\omega_1 t - ik_1 z) + E_2(\mathbf{r}_\perp, z, t)\exp(i\omega_2 t - ik_2 z) \quad (1)$$

interacting resonantly with a three-level system (Fig. 1) containing a metastable state $|2\rangle$. We assume that the wave-packet frequencies (ω_1, ω_2) coincide with the frequencies of atomic transitions, $\omega_1 = \omega_{13}$ and $\omega_2 = \omega_{23}$, so that a two-photon resonance takes place. For a rarefied gas, the relation between the wavenumbers and frequencies can be taken in the form of the dispersion relation in vacuum $k_{1,2} = \omega_{1,2}/c$.

The evolution of wave packets $E_{1,2}(r_\perp, z, t)$ is described by the reduced equations

$$2ik_j\left(\frac{\partial E_j}{\partial z} + \frac{1}{c}\frac{\partial E_j}{\partial t}\right) + \Delta_\perp E_j = 4k_j^2\pi P_j, \quad (2)$$

where P_j is the complex polarization amplitude induced by the field E_j (j = 1, 2). It is determined by the nondiagonal elements of density matrix ρ_{j3}:

$$P_j = Nb_{3j}\rho_{j3}, \quad (3)$$

where N is the atomic density and d_{3j} are the electric dipole moments of allowed transitions.

0021-3640/04/7906-0272$26.00

The specific features of wave-packet interaction in the case considered are caused by the fact that the relaxation rate Γ of low-frequency coherence is much lower than the upper-level decay rate γ, $\Gamma \ll \gamma$. The relaxation processes in this system are conditioned by the strongly different characteristic times. Clearly, the population n_3 of the upper level $|3\rangle$ and the coherences ρ_{13} and ρ_{23} reach their stationary values most rapidly. For wave fields smoothly varying at times

$$\tau_E \gg \gamma^{-1}, \tag{4}$$

the corresponding density-matrix elements are assumed to be quasi-stationary. The resulting dynamic equations for the density-matrix components of a Λ-type atom [1, 2] take the form

$$i\dot{n}_1 = -(g_1\rho_{31} - \text{c.c.}) + i\gamma n_3, \tag{5}$$

$$i\dot{n}_2 = -(g_2\rho_{32} - \text{c.c.}) + i\gamma n_3, \tag{6}$$

$$i\dot{\rho}_{12} = -g_1\rho_{32} + g_2^*\rho_{13} - i\Gamma\rho_{12}. \tag{7}$$

The quasi-stationary components n_3, ρ_{13}, and ρ_{23} are determined from the following relationships:

$$-g_1(n_3 - n_1) + g_2\rho_{12} = i\gamma\rho_{13}, \tag{8}$$

$$-g_2(n_3 - n_2) + g_1\rho_{21} = i\gamma\rho_{23}, \tag{9}$$

$$n_1 + n_2 + n_3 = 1. \tag{10}$$

Here, n_1, n_2, and n_3 are the populations of the respective levels, $\rho_{ij} = \rho_{ji}^*$ are the nondiagonal density-matrix elements, and $g_i = d_iE_i/\hbar$ are the Rabi frequencies. Expression (10) ensures the particle-number conservation in a three-level system.

One can readily find from Eqs. (5)–(10) that the time of establishing stationary population is

$$\tau_N \approx \left(\frac{|g_1|^2 + |g_2|^2}{\gamma}\right)^{-1}, \tag{11}$$

while the relaxation time of the low-frequency coherence ρ_{12} is given by the expression

$$\tau_{12} \approx \left(\Gamma + \frac{|g_1|^2 + |g_2|^2}{\gamma}\right)^{-1}. \tag{12}$$

It then follows that characteristic times (11) and (12) shorten with strengthening field and become equal under the CPT conditions ($|g_1|^2 + |g_2|^2 \gg \Gamma\gamma$).

Let us consider the long-time evolution of a "weak" wave packet ($|g_1|^2 \ll |g_2|^2$) in more detail. We assume that the radiation at frequency ω_2 is continuous and uniform; i.e., $g_2 = \text{const} = g$. The field amplitude g is much smaller than the saturation amplitude for the optical transitions in the Λ-type scheme ($g \ll \gamma$). In the case of a slowly varying (on the relaxation time scale (11), (12)) wave field g_1, we will determine the polarization P_1 using the adiabatic approximation. The calculation

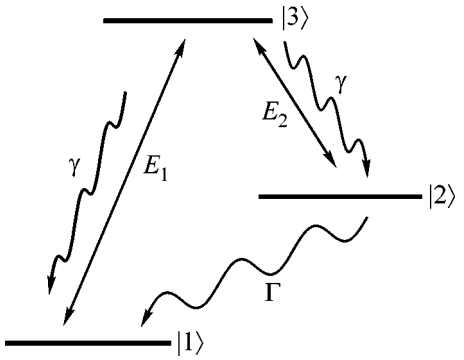

Fig. 1. Energy-level scheme of a Λ-type atom. The wave E_1 is resonant with the $|1\rangle \longleftrightarrow |3\rangle$ transition, the E_2 wave is resonant with the $|2\rangle \longleftrightarrow |3\rangle$ transition, and the low-frequency $|1\rangle \longleftrightarrow |2\rangle$ transition is forbidden.

of the time derivatives in Eqs. (5)–(7) by the perturbation method brings about equation

$$\frac{1}{c}\frac{\partial g_1}{\partial t} + \left(\frac{\partial}{\partial z} + \frac{i}{2k_1}\Delta_\perp\right)g_1$$

$$= -\frac{\mu}{g^2}\frac{\partial g_1}{\partial t} - \frac{\mu\Gamma}{g^2}g_1 + \frac{2\mu|g_1|^2}{g^4}\frac{\partial g_1}{\partial t} \tag{13}$$

$$+ \frac{\mu\gamma}{g^4}\frac{\partial^2 g_1}{\partial t^2} - \frac{\mu\gamma^2}{g^6}\frac{\partial^3 g_1}{\partial t^3},$$

which describes the wave-field evolution under the conditions of electromagnetically induced transparency ($g^2 > \Gamma\gamma$). Here, the field E_1 is expressed through its Rabi frequency g_1 and the parameter $\mu = 4\pi N\omega d_{13}^2/\hbar c$ is introduced. The first term on the right-hand side of Eq. (13) accounts for the well-known decrease in the propagation velocity of a probe pulse in the Λ-type system. The second and fourth terms are responsible for the pulse dissipation on the propagation path; a "uniform" (along the pulse length) wave-packet decay (second term) is determined by the relaxation rate Γ of low-frequency coherence, and the decay in the case of $\Gamma = 0$ is due to the diffusional wave-packet spreading (fourth term). The nonlinear third term appears because the group velocity of a wave packet in the Λ-type system depends on the weak amplitude g_1. Finally, the last term on the right-hand side of Eq. (13) accounts for the wave dispersion in the electromagnetic transparency window.[1] One can see from Eq. (13) that the dissipative effects in the wave packet with a small ($|g_1| \ll |g|$), though finite amplitude, predominate over the dispersion effects. Of all the dissipative effects, we will consider only the dissipation associated with the finite

[1] Note that the dispersion relation obtained and analyzed in [11] follows from Eq. (13) in the linear approximation.

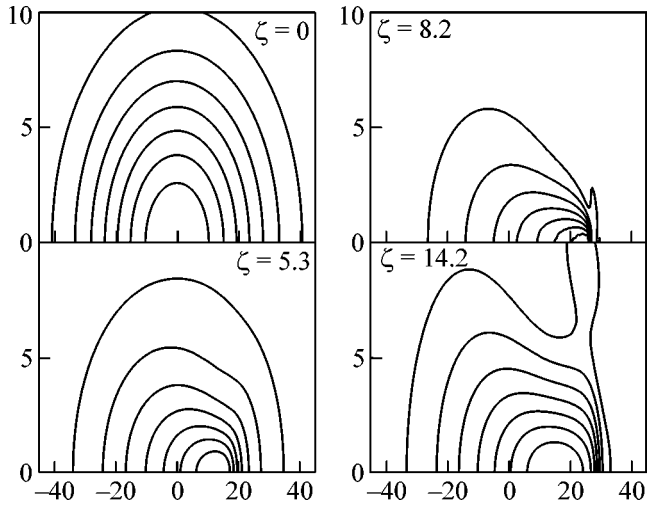

Fig. 2. |ψ|-Field isolines for the initial distribution $\psi(z = 0) = 1.5\exp(-0.5(r/5)^2 - 0.5(\tau/20)^2 - 0.15i\tau)$ and various distances from the entrance into a medium with electromagnetically induced transparency.

width of the EIT window (i.e., $\Gamma = 0$ in Eq. (13)) and introduce the dimensionless variables

$$\psi = g_1/g_m, \quad \tau = 2g_m^2(t - z/v_{gr})/\gamma,$$

$$v_{gr} = (1/c + \mu/g^2)^{-1}, \quad z_{\text{new}} = 4\mu g_m^4 z/g^4\gamma,$$

$$r_{\text{new}} = 2g_m^2\sqrt{2\hbar\mu}/(g^2\sqrt{\gamma}),$$

where g_m is a free parameter on the order of the maximal field value $g_m \sim \max(g_1(\xi, z))$ in the wave packet. As a result, we arrive at the equation

$$-i\frac{\partial\psi}{\partial z} + \Delta_\perp\psi + i|\psi|^2\frac{\partial\psi}{\partial\tau} + i\frac{\partial^2\psi}{\partial\tau^2} = 0, \qquad (14)$$

which describes the wave-packet self-action dynamics in the coordinate system associated with the pulse group velocity v_{gr}. In the experiments, the group velocity, as a rule, is much lower than the velocity of light [3], and the deceleration $v_{gr}/c \approx g^2/c\mu$ is determined by the medium parameters and the pump-wave amplitude.

In the one-dimensional case ($\Delta_\perp = 0$), the self-action dynamics are governed by the competition of the nonlinearity introduced by the amplitude dependence of group velocity with the dissipation and are manifested in the steepening of the pulse leading edge.

2. To illustrate the salient features of self-action, we consider the spatial evolution of a continuous radiation at the frequency detuned by Ω from the resonance frequency. By substituting the field $\psi = G(z, r_\perp)\exp(i\Omega\tau)$ into Eq. (14), we obtain the equation

$$-i\frac{\partial G}{\partial z} + \Delta_\perp G - \Omega|G|^2G - i\Omega^2G = 0. \qquad (15)$$

It accounts for the radiation self-action in a medium with cubic (Kerr) nonlinearity and dissipation. The nonlinear term is proportional to the frequency shift, and, for the negative detuning from the resonance ($\Omega < 0$), the nonlinearity in the Λ-type scheme is focusing. The absorption coefficient of a monochromatic radiation in the transparency window increases as Ω^2, so that the nonlinear effects predominate over the dissipation at small values of detuning $|\Omega| \ll 1$. The condition for the predominance of the nonlinear wave-beam refraction over the diffraction in the axially symmetric case implies that the power is higher than its self-focusing critical value. In the dimensional variables, one obtains for the self- focusing critical power

$$P_{cr} = 5.58\frac{c|g|^4}{8\pi\hbar\mu|\Omega|}. \qquad (16)$$

Evidently, the critical power decreases with increasing the detuning Ω. However, the frequency shift Ω must not exceed the width of EIT window; i.e.,

$$|\Omega| < g^2/\gamma. \qquad (17)$$

Accordingly, the critical power cannot be smaller than its minimal value

$$P_{cr}^{\min} = 5.85\frac{c|g|^2\gamma}{8\pi\hbar\mu}. \qquad (18)$$

Critical power (18) decreases also with decreasing amplitude $|g|$ of the controlling field, but it is bounded from below by the EIT condition $g^2 > \gamma\Gamma$. In reality, the critical power of a probe wave may become greater than (18) due to the finite pulse duration.

3. Below, we present the results of numerical simulation of the self-action dynamics performed for a finite EIT band using Eq. (14). The evolution of an axially symmetric distribution of the form

$$\psi(r, \tau, z = 0) = A_0\exp(-\tau^2/2a_\tau^2 - r^2/2a_r^2 + i\Omega\tau) \qquad (19)$$

was studied, where A_0 is the field amplitude, a_τ and a_r are the characteristic scales of the distributions in the respective coordinates, and Ω is the detuning from the resonance in the Λ-type scheme.

First of all, it should be noted that, in the case of initial Gaussian distribution with zero frequency shift ($\Omega = 0$), field strengthening (focusing) was attained for

none of the amplitudes A_0. The calculations with a positive shift ($\Omega > 0$) point to additional defocusing and a more rapid decrease in the field amplitude.

Of greater interest is the behavior of the distribution with a negative frequency detuning. The evolution of the initial distribution with parameters $A_0 = 1.5$, $a_r = 5$, and $a_\tau = 20$ and negative frequency shift $\Omega = -0.15$ is demonstrated in Fig. 2. At the first stage, the field self-focusing occurs against the background of leading-edge steepening, typical of nonlinear dispersion. The rise in the maximal field amplitude is stabilized as the spectrum broadens during the processes of leading-edge modification and spectral harmonic generation outside the transparency band. A dissipative decrease in the wave-field power to a value smaller than critical subsequently brings about wave-packet spreading mainly in the transverse direction. Inasmuch as the strong decay occurs on the paths of lengths on the order of the breaking length, the radiation self-focusing distance can be estimated using one-dimensional Eq. (14). It is well known that the profile of the shock-wave type appears in this case on the paths $z \simeq \tau_0/A_0^2$, where τ_0 is the pulse duration and A_0 is the maximal field amplitude. For the parameters used in our numerical calculation, this estimate gives $z_f = 9$. A somewhat smaller value, $z_f \approx 8$, obtained in the numerical simulation (Fig. 3) is likely caused by the increase in the maximal field on the axis of the system upon self-focusing. As the initial amplitude A_0 increases, the self-focusing proceeds more intensely; i.e., field strengthening with respect to the initial level becomes more and more pronounced (inset in Fig. 3). It should also be noted that the detuning interval where the radiation self-focusing occurs in the Λ-type scheme becomes noticeably wider with an increase in amplitude; the increase in the amplitude A_0 of the initial distribution from 1.5 to 1.7 (solid and dashed curves in the inset) doubles this interval.

4. Our study of the laser-radiation self-action dynamics under the EIT conditions has revealed a number of special features of this process. It should primarily be noted that the self-action in the case of resonant wave-field interaction is determined by the amplitude dependence of the wave-packet group velocity. In this case, the pulse leading edge steepens upon pulse propagation. For a spatially nonuniform (with respect to the transverse coordinate) initial field distribution, the group-velocity dispersion brings about horseshoe distortion of the leading edge of wave packet.

If the radiation frequency is detuned from resonance, the nonlinear effects in the Λ-type scheme appear as the Kerr-type nonlinearity, resulting in the radiation self-focusing (self-defocusing). Due to the finiteness of the transparency band (determined by the pump-wave field), these processes proceed under conditions of increasing (with increasing frequency shift) absorption.

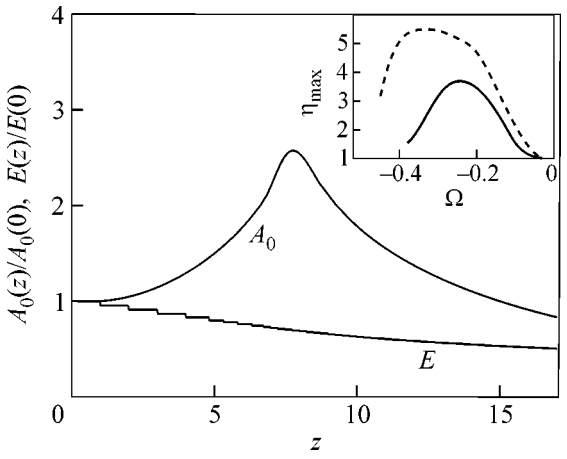

Fig. 3. Dynamics of the maximal field amplitude A_0 and the total energy E for the same initial conditions as in Fig. 2. All quantities are normalized to their initial values. Inset: the dependence of the maximum field strengthening $\eta_{max} = |\psi_{max}|/A_0$ on the initial frequency shift Ω. The solid curve is for the initial field amplitude $A_0 = 1.5$, and the dashed curve is for a slightly larger amplitude $A_0 = 1.7$.

Appreciable radiation self-focusing is possible in the case of negative wave-field detuning from the resonance frequency. For Gaussian beams, it occurs only in the frequency range $\Omega < 0$, i.e., in half of the transparency window. In the other half of the EIT band, the radiation self-focusing takes place. The competition of the nonlinearity and absorption in the transparency band gives rise, in particular, to the optimal frequency shift for which the self-focusing critical power is minimal. Expression (18) for the self-focusing critical power can conveniently be represented in the form

$$P_{cr} = \frac{\gamma\omega}{\Omega_c^2}\lambda^2 p,$$

where $p = P_{pump}/L^2$ is the pump power density, P_{pump} is the pump power, L is the transverse size of the pump field, λ is the wavelength, and $\Omega_c = (8\pi N\omega d^2/\hbar)^{1/2}$ is the cooperative frequency of the "probe" transition. With the parameters of the EIT experiment carried out in [3] ($\gamma \simeq 10^7$ s^{-1}, $\omega \simeq 10^{15}$ s^{-1}, $\Omega_c \simeq 10^9 - 10^{10}$ s^{-1}), the self-focusing critical power for beams of size L equal to several thousand wavelengths is on the order of $(10^{-5}$–$10^{-2})P_{pump}$.

We are grateful to M.D. Tokman for helpful discussions. This work was supported by the Russian Foundation for Basic Research (project nos. 01-02-17388 and 04-02-17147).

REFERENCES

1. B. D. Agap'ev, M. B. Gornyĭ, B. G. Matisov, and Yu. V. Rozhdestvenskiĭ, Usp. Fiz. Nauk **163**, 1 (1993) [Phys. Usp. **36**, 763 (1993)].
2. M. O. Scully and M. S. Zubairy, *Quantum Optics* (Cambridge Univ. Press, Cambridge, 1997).
3. M. D. Lukin, P. Hemmer, and M. O. Scully, Adv. At. Mol. Opt. Phys. **42**, 347 (2000); A. B. Matsko, O. Kocharovskaya, Y. Rostovtsev, *et al.*, Adv. At. Mol. Opt. Phys. **46**, 191 (2001).
4. J. H. Eberly, M. L. Pons, and H. R. Haq, Phys. Rev. Lett. **72**, 56 (1994).
5. A. V. Andreev, Zh. Éksp. Teor. Fiz. **113**, 747 (1998) [JETP **86**, 412 (1998)].
6. V. G. Arkhipkin and I. V. Timofeev, Kvantovaya Élektron. (Moscow) **30**, 180 (2000).
7. B. G. Matisov and I. E. Mazets, Pis'ma Zh. Tekh. Fiz. **20** (4), 16 (1994) [Tech. Phys. Lett. **20**, 140 (1994)]; S. F. Huelga, C. Maochiavello, T. Pellizzari, *et al.*, Phys. Rev. Lett. **79**, 3865 (1997).
8. J. T. Manassah and V. Gross, Opt. Commun. **124**, 418 (1996).
9. M. Jain, A. J. Merriam, A. Kasapi, *et al.*, Phys. Rev. Lett. **75**, 4385 (1995).
10. Tao Hong, Phys. Rev. Lett. **90**, 183901 (2003).
11. S. E. Harris, J. E. Field, and A. Kasapi, Phys. Rev. A **46**, R29 (1992).

Translated by V. Sakun

JETP Letters, Vol. 79, No. 6, 2004, pp. 277–281. From Pis'ma v Zhurnal Éksperimental'noĭ i Teoreticheskoĭ Fiziki, Vol. 79, No. 6, 2004, pp. 335–339.

Impurity-Induced Stabilization of Luttinger Liquid in Quasi-One-Dimensional Conductors¶

S. N. Artemenko

Institute for Radioengineering and Electronics, Russian Academy of Sciences, Moscow, 125009 Russia

e-mail: art@cplire.ru

Received December 9, 2003

It is shown theoretically that the Luttinger liquid can exist in quasi-one-dimensional conductors in the presence of impurities in a form of a collection of bounded Luttinger liquids. The conclusion is based on the observation by Kane and Fisher that a local impurity potential in Luttinger liquid acts, at low energies, as an infinite barrier. This leads to a discrete spectrum of collective charge and spin density fluctuations, so that interchain hopping can be considered as a small parameter at temperatures below the minimum excitation energy of the collective modes. The results are compared with recent experimental observation of a Luttinger-liquid-like behavior in thin $NbSe_3$ and TaS_3 wires. © *2004 MAIK "Nauka/Interperiodica".*

PACS numbers: 71.10.Pm; 71.27.+a; 71.45.Lr; 73.21.Hb

Electronic properties of one-dimensional (1D) metals are known to be very different from those of ordinary three-dimensional (3D) metals (for a review, see [1–3]). 3D electron gas is well described by Landau's Fermi-liquid picture, in which interaction modifies free electrons, making them quasiparticles that behave in many respects like noninteracting electrons. In contrast to the 3D case, in 1D electronic systems, the Fermi-liquid picture breaks down even in the case of the arbitrarily weak interaction. In 1D metals, single-electron quasiparticles do not exist, and the only low energy excitations turn out to be charge and spin collective modes with the sound-like spectrum. These modes are dynamically independent, giving rise to a spin-charge separation in 1D systems. Furthermore, correlation functions at large distances and times decay as a power law with interaction-dependent exponents. Such a behavior has been given the generic name Luttinger liquid [4].

The concept of Luttinger liquid is of great interest in view of its application to real physical systems, such as carbon nanotubes and semiconductor heterostructures with a confining potential (quantum wires and quantum Hall effect edge states). The case of special interest is quasi-1D conductors, i.e., highly anisotropic 3D conductors with chainlike structure. Numerous experimental studies of both organic and inorganic quasi-1D conductors at low temperatures typically demonstrate broken-symmetry states, like superconductivity, spin- or charge-density wave (CDW) states, and a metallic behavior above the transition temperature with nonzero single-particle density of states at Fermi energy. For instance, the most studied inorganic quasi-1D metals undergo the Peierls transition from a metallic state either to a semiconducting CDW state (e.g., blue bronze $K_{0.3}MoO_3$, TaS_3, $(TaSe_4)_2I$ etc.) or to semimetallic CDW state ($NbSe_3$) [5]. Typically, these transitions occur in the temperature range 50–250 K. From the theoretical point of view, the formation of Luttinger liquid in quasi-1D conductors at low enough temperatures is also problematic because of the instability towards 3D coupling in the presence of arbitrarily small interchain hopping [6–10]. So, the interchain hopping induces a crossover to 3D behavior at low energies, while Luttinger liquid behavior can survive only at a high enough energy scale where it is not affected by 3D coupling.

In contrast to the interchain hopping, the Coulomb interaction between the electrons at different chains does not destroy the Luttinger liquid state, the main difference from the 1D case being the absence of simple scaling relations between the exponents of the various correlation functions [11–14].

However, in recent experimental studies of temperature and field dependence of conductivity of TaS_3 and $NbSe_3$ in nanosized crystals, a transition from room-temperature metallic behavior to nonmetallic one accompanied by the disappearance of the CDW state at temperatures below 50–100 K was observed [15–17]. The low temperature nonmetallic state was characterized by power law dependences of the conductivity on voltage and temperature like that expected in Luttinger liquid, or by a stronger temperature dependence, corresponding to the variable-range hopping. Similar dependences of conductivity were also reported in focused-ion beam processed or doped relatively thick $NbSe_3$ crystals [17].

In order to account for such behavior, we study the possibility of impurity-induced stabilization of a gap-

¶ This article was submitted by the author in English.

less Luttinger liquid state in quasi-1D metals. Impurities in Luttinger liquid are known to act as infinite barriers, forming the effective boundaries for low energy excitations [18–20]. This leads to a dimensional quantization and, consequently, to a minimal excitation energy ω_1. As a result, the interchain hopping does not destroy the Luttinger liquid phase at temperatures $T \ll \omega_1$, producing only small perturbations of the 1D picture. To show this, we consider first the gapless 1D Tomonaga–Luttinger (TL) model with impurity potential included and make certain that the system with impurities breaks up into a set of independent segments described as bounded Luttinger liquid with discrete spectrum. Then, we calculate corrections caused by the interchain hopping to thermodynamic potential and to the one-particle Green's function and find that such corrections are small at low temperatures. Finally, we discuss modifications introduced by generalization of the TL model to the more realistic case of Coulomb potential and compare our results with experimental data.

First of all, we start with the TL model, ignoring interchain hopping integral $t_\perp$ in order to formulate the problem in the zeroth approximation in $t_\perp$. Electronic operators for right ($r = +1$) and left ($r = -1$) moving electrons with spin s are given in terms of phase fields as (see [1, 3])

$$\psi_{r,s}(x) = \lim_{\alpha\to 0}\frac{e^{irk_F x}}{\sqrt{2\pi\alpha}}\eta_{r,s}e^{iA_r},$$
$$A_r = \frac{1}{\sqrt{2}}[\Theta_\rho - r\Phi_\rho + s(\Theta_\sigma - r\Phi_\sigma)]. \quad (1)$$

Here, phase fields $\Phi_\nu(x)$ are related to charge ($\nu = \rho$) and spin ($\nu = \sigma$) densities, while fields $\Theta_\nu(x)$ are related to the momentum operators $\Pi_\nu = (1/\pi)\partial_x\Theta_\nu$ canonically conjugate to Φ_ν. Further, $\eta_{r,s}$ are Majorana ("real") Fermionic operators that assure proper anticommutation relations between electronic operators with different spin s and chirality r, and the cut off length α is assumed to be of the order of the interatomic distance.

We describe the intrachain properties of the system by the standard TL Hamiltonian [1, 3] with added $2k_F$ impurity backscattering term [2]. In the bozonized form, it reads

$$H = \sum_{\nu=\rho,\sigma}\int dx\left\{\frac{\pi v_\nu K_\nu}{2}\Pi_\nu^2 + \frac{v_\nu}{2\pi K_\nu}(\partial_x\Phi_\nu)^2\right\}$$
$$+\sum_i V_0 d\,\delta(x - x_i)\cos(\sqrt{2}\Phi_\rho + 2k_F x)\cos(\sqrt{2}\Phi_\sigma(x)), \quad (2)$$

where v_ν are velocities of the charge ($\nu = \rho$) and spin ($\nu = \sigma$) modes; $K_\nu = v_F/v_\nu$ is the standard Luttinger liquid parameter, describing the strength of the interaction; and V_0 and $d \sim \alpha$ are amplitude and radius of the scattering potential, respectively.

Kane and Fischer [18] found that the backscattering impurity potential for repulsive potential ($K_\rho < 1$) flows to infinity under scaling. Their arguments were generalized by Fabrizio and Gogolin [21] to the case of many impurities. It was shown that the impurity potential can be considered as effectively infinite, provided that the mean distance, l, between impurities satisfies the condition

$$l \gg \frac{1}{k_F}\left(\frac{D}{V_0}\right)^{2/(1-K_\rho)}, \quad (3)$$

where D is the bandwidth. We assume that the impurity potential is of atomic scale, $V_0 \lesssim D$, and the interaction between electrons is not too weak (i.e., K_ρ is not too close to 1). Then, condition (3) is satisfied for $l \gg 1/k_F \sim \alpha$, which is of the order of interatomic distance. So, the limit of strong impurity potential should be a good approximation in a wide range of impurity concentrations.

Further, Π_ν, Θ_ν, and Φ_ν must obey the commutation relations (see [1–3]) ensuring anticommutation of electronic operators (1). Using then the analogy of Eq. (2) with the Hamiltonian of an elastic string strongly pinned at impurity sites, we can write solutions for the phase operators Φ_ν and Θ_ν in the region between impurity positions at $x = x_i$ and x_{i+1} as

$$\Phi_\nu(x) = \sum_{n=1}^{\infty}\sqrt{\frac{K_\nu}{n}}(b_n + b_n^+)\sin q_n\tilde{x}$$
$$+\frac{\tilde{x}\Phi_{i+1} - (\tilde{x} - l_i)\Phi_i}{\sqrt{2}l_i}\delta_{\nu\rho} - \sum_{j<i}\pi\Delta N_{\nu j} - \pi\Delta N_{\nu i}\frac{\tilde{x}}{l_i}, \quad (4)$$
$$\Theta_\nu(x) = \sum_{n=1}^{\infty}\sqrt{\frac{1}{K_\nu n}}(b_n - b_n^+)\cos q_n\tilde{x} + \theta_\nu,$$

where $\tilde{x} = x - x_i$, $l_i = x_{i+1} - x$, $q_n = \pi n/l_i$, and Φ_i is the modulo 2π residue of $2k_F x_i$. Further, $\Delta N_{\rho i} = (\Delta N_{\uparrow i} + N_{\downarrow i})/\sqrt{2}$, $\Delta N_{\sigma i} = (\Delta N_{\uparrow i} - N_{\downarrow i})/\sqrt{2}$, and $\Delta N_{\uparrow i}$ ($\Delta N_{\downarrow i}$) is the number of extra electrons with spin up (down) in the region between ith and $(i + 1)$th impurities; and finally, $\theta_{\nu i}$ is the phase canonically conjugate to $\Delta N_{\nu i}$ ($[\theta_{\nu i}, \Delta N_{\nu i}] = i$).

Excitation spectra of the eigenmodes are $\omega_\nu = n\omega_{1,\nu} \equiv v_\nu q_n$, where $\omega_{1,\nu} = \pi v_\nu/l_i$ is the minimum excitation frequency for mode ν.

Note that, if we consider the open boundary conditions at the sample ends, $x = 0$, and $x = L$ (instead of periodic boundary conditions that are commonly used) then operators η_s in Eq. (1) are the same for electrons going right and left. In this case, the electron field operator, $\psi_s(x) = \psi_{s+}(x) + \psi_{s-}(x)$, vanishes at impurity positions, $x = x_i$, and expressions for the phase fields between the impurity sites turn out to be similar to

those found for bounded 1D Luttinger liquid in [21–23], the main difference being the summation over $j < i$ that ensures proper commutation relations between the electron operators related to different segments between impurities. Thus, the system breaks up into a set of independent segments described as bounded Luttinger liquid with discrete spectrum.

Now, we consider the role of interchain hopping adding to (2) the hopping Hamiltonian

$$H_\perp = t_\perp \sum_{m,n,r,s} \int dx \psi^+_{r,s,m}(x)\psi_{r,s,n}(x) + HC$$

$$= \sum_{m,n,r,s} \int dx \frac{it_\perp \eta_{r,s,n}\eta_{r,s,m}}{\pi\alpha}[\sin(A_{r,m} - A_{r,n}) \quad (5)$$

$$+ \sin(A_{r,m} - A_{-r,n} + 2irk_F x)],$$

where indices n and m, denoting the chain numbers related to the nearest neighbors, are added.

Arguments by Schulz [8] on instability of the Luttinger liquid in the presence of the interchain hopping were based on calculations of temperature dependence of the thermodynamic potential at low temperatures. So, we calculate the contribution of the interchain hopping to the thermodynamic potential per unit volume given by the standard expression [24]

$$\Delta\Omega = -T\ln\langle S\rangle/V, \quad S = T_\tau \exp\left(-\int_0^{1/T} H_\perp(\tau)d\tau\right), \quad (6)$$

where V is the volume, T_τ stands for imaginary time ordering, and $\langle\ldots\rangle$ means thermodynamic averaging over the unperturbed state.

At temperatures $T \gg \omega_{1,\nu}$, the discreteness of the excitation spectrum can be neglected; hence, according to [6–10], interchain hopping is expected to make significant contributions, destroying the Luttinger liquid. We examine the opposite limit, $T \ll w_{1,\nu}$, which does not exist in pure infinite Luttinger liquid.

Consider first the second order correction in $t_\perp$. The leading contribution to $\langle S\rangle$ in Eq. (6) is given by items in which the term related to a given chain contains contributions from the electrons with the same chirality, r, only,

$$\sum_{m,r,r'} \frac{t_\perp^2}{8\pi^2 - \alpha^2} \int d\mathbf{1}d\mathbf{2}\langle T_\tau \exp\{i[A_{r,m}(\mathbf{1}) - A_{r',n}(\mathbf{1})]\} \quad (7)$$

$$\times \exp\{-i[A_{r,m}(\mathbf{2}) - A_{r',n}(\mathbf{2})]\}\rangle e^{i(r-r')k_F(x_1 - x_2)},$$

where $\mathbf{1} = \{x_1, \tau_1\}$ and $\mathbf{2} = \{x_2, \tau_2\}$. Other items in which the terms related to the same chain contain contributions from electrons moving both left and right make small a contribution, and we do not discuss them in detail.

Then, we use Eq. (4) in (1) and calculate the average in (7) using the relation

$$\langle T_\tau \exp\{iA_{r,m}(\mathbf{1})\}\exp\{-iA_{r,m}(\mathbf{2})\}\rangle$$

$$= \exp\left\{-\frac{1}{2}\langle A^2_{r,m}(\mathbf{1}) + A^2_{r,m}(\mathbf{2}) \quad (8)\right.$$

$$\left. - 2T_\tau[A_{r,m}(\mathbf{1})A_{r,m}(\mathbf{2})]\rangle\right\}.$$

Neglecting small corrections $\propto \exp[-\omega_{1,\nu}/T]$ due to Planck's distribution functions, we find for the average in the exponent

$$\langle T_\tau A_r(\mathbf{1})A_r(\mathbf{2})\rangle$$

$$= \frac{1}{8}\ln\left[\frac{(\cosh z - \cos y_+)^{(K_\nu - K_\nu^{-1})}}{(\cosh z - \cos y_-)^{(K_\nu + K_\nu^{-1})}}\right] \quad (9)$$

$$+ i\tan^{-1}\left[\frac{\sin y_-}{e^z - \cos y_-}\right],$$

where $y_\pm = \pi(\tilde{x}_1 \pm \tilde{x}_2)/l_i$, $z = \pi(\alpha + v_\nu|\tau_1 - \tau_2|)/l_i$ (chain indices are dropped for brevity here).

In the integration over **1** and **2**, the leading contributions comes from the region $\mathbf{1} \approx \mathbf{2}$, i.e., $|y_-| \ll 1$, $z \ll 1$ where expression (7) reduces to

$$\frac{t_\perp^2 mL}{\pi^2\alpha^2 T}\int \frac{\cos[(r-r')k_F(x_-)]dx_-d\tau_-}{\prod_{\nu=\rho,\sigma}[(1+\epsilon_\nu\tau_-)^2 + (x_-/\alpha)^2]^{1+2\delta_\nu}}, \quad (10)$$

where $\epsilon_\nu = v_\nu/\pi\alpha$, $\delta_\nu = \frac{1}{4}(K_\nu + 1/K_\nu - 2)$, $\tau_- = |\tau_1 - \tau_2|$, $x_- = x_1 - x_2$, and m is the number of the nearest-neighbor chains. Contribution to expression (7) from integration over the region $|y_-| \gtrsim 1$, $z \gtrsim 1$, is small, $\sim(\alpha/l_i)^{2\delta}$, $\delta = \delta_\rho + \delta_\sigma$, because δ is not too small in the assumed case of the not too small interaction (cf. Eq. (3)).

Additional items in $\langle S\rangle$ in Eq. (6), in which the terms related to the same chain contain contributions from electrons moving both left and right, is smaller than that given by Eq. (10) by a factor of $\sim(\alpha/l_i)^{K_\rho + K_\sigma}$. For reasonable values of K_ν, this contribution is small and can be neglected.

Similarly, the leading contribution to $\Delta\Omega$ from higher-order terms in series expansion of the exponential in Eq. (6) was found to come from even powers $2n$ in $t_\perp$ that can be represented as a sum of $(2n-1)!!$ items like (7) with almost coinciding times and coordinates. Therefore, summing up the leading contributions and inserting them into Eq. (6), we can calculate the varia-

tion of the thermodynamic potential per single chain and per unit length

$$\Delta\Omega = -a\frac{t_\perp^2 m}{\pi^2 v_F},$$
$$a = \int \frac{(1+\cos 2k_F\alpha x)dxd\tau}{\prod\limits_{\nu=\rho,\sigma}\left[(1+\tau/K_\nu)^2+x^2\right]^{1+2\delta_\nu}}. \quad (11)$$

For moderate repulsion, $\delta \sim 1$, $a \sim 1$. In the limit of strong repulsion, $K_\rho \ll K_\sigma \sim 1$, a is small, $a \sim K_\rho^2$.

Thus, $\Delta\Omega$ is much smaller than the thermodynamic potential of purely 1D Luttinger liquid, $\Omega_0 \sim (1/K_\rho + 1/K_\sigma)\varepsilon_F k_F$,

$$\Delta\Omega/\Omega_0 \sim \left(\frac{t_\perp}{\varepsilon_F}\right)^2,$$

and temperature-dependent corrections to Eq. (11) are determined by small thermally activated contributions $\propto \exp[-\omega_{1,\nu}/T]$.

Now, we calculate modification of the one-particle Green's function due to the interchain hopping

$$G(\mathbf{1},\mathbf{1}') = -\langle T_\tau \psi(\mathbf{1})\bar{\psi}(\mathbf{1}')S\rangle/\langle S\rangle. \quad (12)$$

Again, we consider the low-temperature limit, $T \ll \omega_{1,\nu}$, not existing in a pure infinite system. Consider first the second order correction in $t_\perp$ to the Green's function of a pure 1D system, $G_0(\mathbf{1},\mathbf{1}')$,

$$G_2(\mathbf{1},\mathbf{1}') = -\langle T_\tau \psi(\mathbf{1})\bar{\psi}(\mathbf{1}')S_2\rangle + \langle T_\tau \psi(\mathbf{1})\bar{\psi}(\mathbf{1}')\rangle\langle S_2\rangle. \quad (13)$$

Calculation is similar to that considered above (cf. (7)–(9)). However, in contrast to the case of the thermodynamic potential, where the leading contribution was made by regions of almost coinciding values of times and coordinates, such contributions from two terms in (9) cancel each other. So, the second-order correction is estimated as

$$G_2(\mathbf{1},\mathbf{1}') \lesssim \left(\frac{t_\perp l}{v_F}\right)^2\left(\frac{\alpha}{l}\right)^{2\delta} G_0(\mathbf{1},\mathbf{1}').$$

Estimation of the fourth-order correction in $t_\perp$ gives $G_4 \sim (t_\perp l/v_F)^2(\alpha/l)^{2\delta}G_2$. Therefore, we conclude that at $T \ll \omega_{1,\nu}$ the interchain hopping gives small corrections to the one-particle Green's function, provided that

$$\left(\frac{t_\perp l}{v_F}\right)^2\left(\frac{\alpha}{l}\right)^{2\delta} \sim \left(\frac{t_\perp}{\varepsilon_F}\right)^2\left(\frac{\alpha}{l}\right)^{2\delta-2} \ll 1, \quad (14)$$

where we estimated the cut-off parameter as $\alpha \sim 1/k_F$.

So far we considered the TL model in which interaction is described by coupling constants related to forward- and backscattering. In order to make a comparison with experimental data, we must consider a more realistic Coulomb potential. It is reasonable to assume that the long-range part of the interaction is dominated by the Coulomb potential, while the backscattering is described by relatively small coupling constant g_1. This enables us to concentrate on the spin isotropic case and to ignore the possibility of the spin gap. The problem of the long-range Coulomb potential on an array of chains was solved in [11–13]. It was found that interaction of electrons on a given chain is screened by the electrons on other chains, and the Coulomb interaction can be described by the TL Hamiltonian with coupling constants dependent on wave vector,

$$g_2 = g_4 = \frac{4\pi e^2}{s^2(q_\parallel^2 + \epsilon_\perp q_\perp^2)}, \quad (15)$$

where s is the lattice period in the direction perpendicular to the chains and $\epsilon_\perp$ is a background dielectric constant for the transverse direction. Coupling constants in spin channel remain unaffected. In principle, the coupling constants must be determined by matrix elements of Coulomb potential that depend on the details of wave functions and on chain arrangement and must contain an infinite sum over transverse reciprocal lattice vectors. So, expression (15) is not universal and depends on material.

Equation (15) leads to **q**-dependent velocities

$$\omega_\rho = \frac{v_F}{K_\rho}q_\parallel,$$
$$\frac{1}{K_\rho} = \sqrt{1+\frac{\aleph}{s^2(q_\parallel^2+\epsilon_\perp q_\perp^2)}}, \quad \aleph = \kappa^2 s^2 = \frac{8e^2}{\hbar v_F}, \quad (16)$$

where κ is the inverse Thomas–Fermi screening length.

We do not perform explicit calculations, restricting ourselves to estimations. For the case of **q**-dependent coupling, expressions for the thermodynamic potential and Green's functions contain various integrals of correlation functions over $\mathbf{q}_\perp$. One can show that the results obtained above can be generalized qualitatively to the case of long-range Coulomb interaction if we substitute $q_\perp$ in Eq. (16) for its characteristic value, $q_\perp \sim \pi/s$. For example, integrals for corrections to the thermodynamic potential are dominated by close values of coordinates and times, similar to Eq. (10), and coupling parameters should be substituted by their averages over $q_\perp$,

$$\delta = \frac{1}{4}(\overline{K_\rho} + \overline{1/K_\rho} + k_\sigma + 1/K_\sigma - 4)$$
$$\sim \frac{1}{4}\left[\int \frac{s^2 d^2 q_\perp}{(2\pi)^2}\left(K_\rho + \frac{1}{K_\rho}\right) - 2\right].$$

Note that $\aleph = 8\alpha(c/v_F)$, where α is the fine structure constant. Since v_F is much smaller than the velocity of light, the factor $\aleph$ is large. For $v_F \approx 2\times 10^7$ cm/s, which

is a typical value for transition metal trihalcogenides, $\aleph \sim 90$. This corresponds to the case of strong interaction and leads to quite large values of coupling parameters, $\overline{1/K_\rho} \sim \sqrt{\aleph/\epsilon_\perp} \sim 3$–$8$, $\delta \sim 1/2$–2.

Now, we discuss conditions for observation of the Luttinger liquid in quasi-1D conductors stabilized by impurities. First, we discuss the condition for the temperature limiting from above the region where the Luttinger liquid can exist. This condition reads $T \ll \omega_{1,\nu}$. The minimal excitation energies, $\omega_{1,\nu}$, can be estimated as

$$\omega_{1,\nu} = \frac{\hbar v_F}{l}\overline{1/K_\nu} \sim \varepsilon_F\left(\frac{1}{k_F l}\right)\overline{1/K_\nu} \sim \varepsilon_F c_i \overline{1/K_\nu},$$

where c_i stands for dimensionless impurity concentration corresponding to number of impurities per one electron. As Fermi energy in $NbSe_3$ and TaS_3 is about 1 eV, we find that $\omega_{1,\rho}$ is about 100 K for an impurity concentration of $c_i \sim 10^{-2}$–10^{-3}.

Another condition to be fulfilled is the smallness of corrections to the Green's function due to interchain hopping. According to Eq. (14), the corrections are small, provided that

$$\left(\frac{t_\perp}{\varepsilon_F}\right)^2 c_i^{2\delta-2} \ll 1.$$

If the interaction is strong enough, $\delta \gtrsim 1$, this condition is no stricter than the condition for the limiting temperature discussed above. For lower strength of interaction, $\delta < 1$, this condition reads

$$c_i \gg \left(\frac{t_\perp}{\varepsilon_F}\right)^{1/(2-2\delta)}.$$

Estimating $t_\perp$ as being of the order of the Peierls transition temperature, $T_P \sim 100$–$200\ \mathrm{K} \sim 0.01\varepsilon_F$, we find that this condition can be fulfilled easily even at $\delta = 1/2$ for relatively small impurity concentration, $c_i \gg 10^{-2}$.

Thus, we find that Luttinger liquid can be stabilized by impurities in relatively pure linear-chain compounds at rather high temperatures corresponding to experimental observation [15–17] of the transition from metallic to nonmetallic conduction characterized by power law dependences of conductivity and by conductivity resembling the variable-range hopping. However, in order to make a detailed comparison with the experimental data, calculation of the conductivity in a random network made of weakly coupled bounded Luttinger liquids is needed.

The author is grateful to S.V. Zaitsev-Zotov for useful discussions. This work was supported by Russian Foundation for Basic Research, by INTAS, CRDF, and by collaborative program with the Netherlands Organization for Scientific Research.

REFERENCES

1. J. Voit, Rep. Prog. Phys. **58**, 977 (1995).
2. M. P. A. Fisher and L. I. Glazman, in *Mesoscopic Electron Transport*, Ed. by L. L. Sohn, L. Kouwenhoven, and G. Schön (Kluwer Academic, Dordrecht, 1997).
3. H. J. Schulz, G. Cuniberti, and P. Pieri, *Field Theories for Low-Dimensional Condensed Matter Systems* (Springer, Berlin, 2000); cond-mat/9807366.
4. F. D. M. Haldane, J. Phys. C **14**, 2585 (1981).
5. G. Grüner, *Density Waves in Solids* (Addison-Wesley, Reading, 1994).
6. V. N. Prigodin and Yu. A. Firsov, Zh. Éksp. Teor. Fiz. **76**, 736 (1979) [Sov. Phys. JETP **49**, 369 (1979)]; Zh. Éksp. Teor. Fiz. **76**, 1602 (1979) [Sov. Phys. JETP **49**, 813 (1979)]; Yu. A. Firsov, V. N. Prigodin, and Ch. Seidel, Phys. Rep. **126**, 245 (1985).
7. S. A. Brazovskiĭ and V. M. Yakovenko, Zh. Éksp. Teor. Fiz. **89**, 2318 (1985) [Sov. Phys. JETP **62**, 1340 (1985)].
8. H. J. Schulz, Int. J. Mod. Phys. B **5**, 57 (1991).
9. D. Boies, C. Bourbonnais, and A.-M. S. Tremblay, Phys. Rev. Lett. **74**, 968 (1995); cond-mat/9604122.
10. E. Arrigoni, Phys. Rev. Lett. **83**, 128 (1999).
11. S. Barišič, J. Phys. (Paris) **44**, 185 (1983).
12. S. Botrič and S. Barišič, J. Phys. (Paris) **44**, 185 (1984).
13. H. J. Schulz, J. Phys. C: Solid State Phys. **16**, 6769 (1983).
14. R. Mukhopadhyay, C. L. Kane, and T. C. Lubensky, Phys. Rev. B **64**, 045120 (2001).
15. S. V. Zaĭtsev-Zotov, V. Ya. Pokrovskiĭ, and P. Monceau, Pis'ma Zh. Éksp. Teor. Fiz. **73**, 29 (2001) [JETP Lett. **73**, 25 (2001)].
16. S. V. Zaitsev-Zotov, Microelectron. Eng. **69**, 549 (2003).
17. S. V. Zaitsev-Zotov, M. S. H. Go, E. Slot, and H. S. J. van der Zant, Phys. Low-Dimens. Semicond. Struct. **1–2**, 79 (2002); cond-mat/0110629.
18. C. L. Kane and M. P. A. Fisher, Phys. Rev. Lett. **68**, 1220 (1992).
19. K. A. Matveev and L. I. Glazman, Phys. Rev. Lett. **70**, 990 (1993).
20. A. Furusaki and N. Nagaosa, Phys. Rev. B **47**, 4631 (1993).
21. M. Fabrizio and A. O. Gogolin, Phys. Rev. B **51**, 17827 (1995).
22. S. Eggert, H. Johannesson, and A. Mattsson, Phys. Rev. Lett. **76**, 1505 (1996).
23. A. E. Mattsson, S. Eggert, and H. Johannesson, Phys. Rev. B **56**, 15615 (1997).
24. A. A. Abrikosov, L. P. Gor'kov, and I. E. Dzyaloshinskiĭ, *Methods of Quantum Field Theory in Statistical Physics* (Fizmatgiz, Moscow, 1962; Dover, New York, 1963).

JETP Letters, Vol. 79, No. 6, 2004, pp. 282–285. Translated from Pis'ma v Zhurnal Éksperimental'noĭ i Teoreticheskoĭ Fiziki, Vol. 79, No. 6, 2004, pp. 340–343.

Diamond-Like and Graphite-Like Carbon States in Short-Period Superlattices

T. N. Zavaritskaya*, V. A. Karavanskiĭ, N. N. Mel'nik*, and F. A. Pudonin***

** Lebedev Physical Institute, Russian Academy of Sciences, Moscow, 119991 Russia*

*** Natural Sciences Center, Institute of General Physics, Russian Academy of Sciences, Moscow, 119991 Russia*

Received January 29, 2004; in final form, February 9, 2004

The Raman and luminescence spectra are studied in superlattices consisting of carbon layers separated by thin SiC barrier layers. It is shown experimentally that, upon the avalanche annealing of an initially amorphous superlattice, the carbon layers can crystallize into either a diamond-like or graphite-like structure, depending on the geometrical parameters of the superlattice. A method is proposed for obtaining carbon films with a specified crystal modification within a unified technology. © *2004 MAIK "Nauka/Interperiodica".*

PACS numbers: 78.67.Pt; 68.65.Cd

To date, a great many investigations have been devoted to studying the physical properties of carbon structures and technological processes providing the basis for their formation. This is connected with the wide variety and unique properties of carbon compounds, which have determined their widespread practical use in areas from nanoelectronics to spacecrafts. However, the preparation of various carbon modifications within a unified technology is a complicated problem, which still remains unsolved [1].

Previously [2], the authors have shown that the periodic potential arising as a result of the alternation of layers differing in the band gap can affect the modification in which the substance crystallizes. The grown superlattices are also characterized by the existence of a periodic potential, which can be favorable to the formation of a specific carbon modification.

In this work, it is proposed that the annealing of amorphous superlattices based on carbon and a broadband semiconductor (here, SiC) with varying layer thicknesses be used to obtain various carbon modifications. It is assumed that, upon pulse annealing, carbon in these structures will transform to a certain modification determined by the superlattice parameters.

Multilayer periodic structures C/SiC with specified thicknesses of the C and SiC layers were manufactured for these experiments. The thickness of carbon layers was chosen to be a multiple of the lattice constant of a known carbon structural modification. Thus, the thicknesses of carbon layers for the graphite- and diamond-like structures were 1.34 and 0.8 nm, respectively. It was assumed that carbon in the structures with the graphite-like thickness will crystallize in the course of annealing into a graphite-like crystalline configuration, whereas carbon in the structures with the diamond-like thickness will transform into a diamond-like structure. Our Raman scattering and luminescence studies confirmed that the annealing of the grown samples resulted in the formation of a graphite-like or diamond-like structure in the samples of superlattices with the corresponding thickness of carbon layers.

Thus, we proposed and implemented a method for obtaining carbon films with a desired crystal modification. It is presumed that this method will allow specified carbon modifications to be obtained in a controlled way within a unified technology.

Radio-frequency sputtering was used to obtain carbon superlattices. The C and SiC deposition rates were 0.7 and 3.3 nm/min, respectively. Graphite and polycrystalline silicon carbide served as the targets for obtaining the carbon and SiC layers. The substrate was KEF-4.5 (100) silicon. A Co layer ~50-nm thick, which was necessary for the subsequent annealing of the as-grown superlattice, was sputtered on the substrate. The layer thicknesses were controlled by the sputtering time, because the deposition rate in this method remained constant during the entire technological process and did not depend on the thickness of the deposited film. The details of the process and the growth features for such superlattices are given in [2].

The conventional thermal annealing is unsuitable for short-period superlattices, because the mutual diffusion of layer atoms in the course of annealing leads to the mixing of layers and the degradation of the superlattice. Therefore, as in [2], a Co underlayer was used in annealing. Upon short-term low-temperature heating, this underlayer transformed from an amorphous state to a crystalline state in a time of $\sim 10^{-11}$–10^{-10} s with heat evolution. This heat is necessary for the superlattice annealing. The new type of annealing proposed in [2] was based on the fact that the internal energy of a layer in an amorphous (disordered) state is higher than the energy of the same layer in a crystalline or polycrystalline modification. This difference in ener-

gies is evolved upon layer transition from an amorphous to crystalline state. However, for an amorphous phase to transform to the crystalline phase, it is necessary to overcome an activation barrier. For a number of materials, for example, Co, this barrier is not very high and can be overcome by the short-term (~1–2 min) low-temperature (300–400°C) heating of this material. The transition rate of a material from an amorphous state to the crystalline state is on the order of the sound velocity, and the amount of evolved heat is proportional to the mass of this material. As was shown in [2], the mutual diffusion of superlattice layer atoms does not proceed under this type of annealing. This type of avalanche annealing is in many ways similar to the pulse laser annealing.

It should be noted that, according to [2], two processes can take place during avalanche annealing. The first one is a simple annealing of the C and SiC layers. Depending on the thickness of the C layers, carbon transforms to either a diamond-like (diamond-like superlattice, DSL) or graphite-like (graphite-like superlattice, GSL) modification if the number of carbon atoms corresponds to only an integer number of monolayers of these two modifications. Note that, because of the difference in the densities of the deposited carbon, diamond, and graphite, it is diamond-like and graphite-like modifications, rather than pure crystalline diamond or graphite structures, that can be obtained in the course of annealing. By varying the thickness of the carbon layers, it is possible to achieve the synthesis of predominantly diamond or graphite structures. It is not inconceivable that certain intermediate crystalline carbon states can exist that have not been synthesized previously. It should be noted here that the thicknesses of carbon layers in an SR must be small, because the difference between the DSL and GSL will disappear as the thickness increases. On this basis, carbon SLs were grown with carbon layer thicknesses of 0.8 nm (the diamond-like layer with $d \sim 4a$, where $a = 0.205$ nm is the interplanar spacing in diamond in the (111) direction) and 1.34 nm (the graphite-like layer with $d \sim 4a$, where $a = 0.335$ nm is the interplanar spacing in graphite in the (002) direction).

The second process that can proceed during the course of SL annealing is associated with the one-dimensional periodic SL potential arising as a result of the alternation of materials differing in the band gap and its action on the crystallization process. As was shown in [2], in the course of annealing, when superlattice atoms are in a nonequilibrium state, the superlattice potential is the only strong potential in the structure being annealed. This potential, by analogy with the Kronig–Penny (KP) potential, will strongly influence the formation of electronic and crystal structures of the sample. In the case of Si/SiO_2 superlattices with a small period (of order 1.0–1.5 nm), it was found that the one-dimensional periodic potential formed, in effect, the superlattice crystal structure, resulting in a material with hexagonal symmetry and lattice parameters differing from both Si and SiO_2. The parameters of the periodic SL potential in the case of carbon SLs are determined not only by the C and SiC band gaps but also by the SL thicknesses. To provide a stronger effect of this potential, the parameters of superlattice potential should be brought closer to the parameters of the KP potential. For this purpose, we manufactured SLs with narrow barriers (1.6 nm), whose periodic potential was similar to the KP potential, and with wide SiC barrier layers (3.2 nm), for which the difference of the superlattice potential from the KP potential was more pronounced.

Table

Sample no.	C thickness (Å)	SiC thickness (Å)	Number of periods
1	14	32	20
2	14	16	20
3	13.4	16	20
4	8	16	20

Porous structures were prepared from all obtained SLs by anodic etching. It is known that anodic etching starts (and predominantly continues) at defects. Previously, we showed that porous films could form with a lower concentration of crystal defects and doping impurity [3] than in the starting crystal. Moreover, in some cases [3], anodic etching is accompanied by the formation of nanocrystalline objects, whose properties are also of great interest.

The parameters of the synthesized samples are given in the table.

The Raman spectra of the synthesized samples are shown in Fig. 1. The Raman spectra of the sputtered C/SiC SLs are almost identical in shape (Fig. 1a), and their shape corresponds to the Raman spectrum of a strongly disordered carbon film (Fig. 1c). After annealing, the spectra of the samples under study became noticeably different (Fig. 1b). The Raman spectrum of sample 1 with the largest thickness of the SiC layers changed insignificantly (Fig. 1b, curve *1*). The spectra of the other samples exhibit shoulders in the region of *D* (~1350 cm^{-1}) and *G* (~1580 cm^{-1}) bands (see lower spectrum in Fig. 1c) differing in the intensity ratios. These bands correspond to the presence of sp^3 and sp^2 bonds, respectively, in the carbon material [4]. The Raman spectra of the annealed samples subjected to anodic etching are shown in Fig. 1c. As was already noted, atoms with a lower binding energy (defects, impurities, etc.) are removed first upon anodic etching. Therefore, the remaining part of the material can have a more perfect crystal structure [3]. We observe a similar picture for the structures under study as well. The *D* and *G* bands are clearly seen in the Raman spectrum of the etched annealed samples (Fig. 1c); however, these bands have different halfwidths and intensities. We note

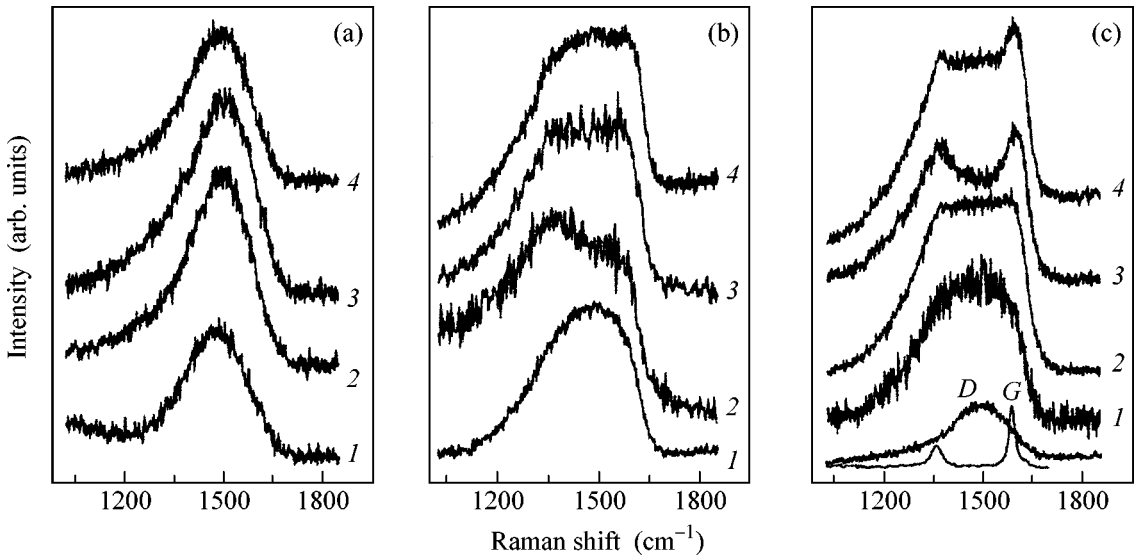

Fig. 1. Raman spectra of (a) sputtered SL samples, (b) samples after avalanche annealing, and (c) porous annealed samples. The Raman spectra of a disordered graphite (two lines) and a carbon film obtained by the decomposition of hydrocarbons (broad asymmetric band) are given at the bottom of graph (c) for comparison. In all graphs, the Raman spectra are shifted vertically with respect to each other for convenience. The numbers at the curves correspond to the sample number.

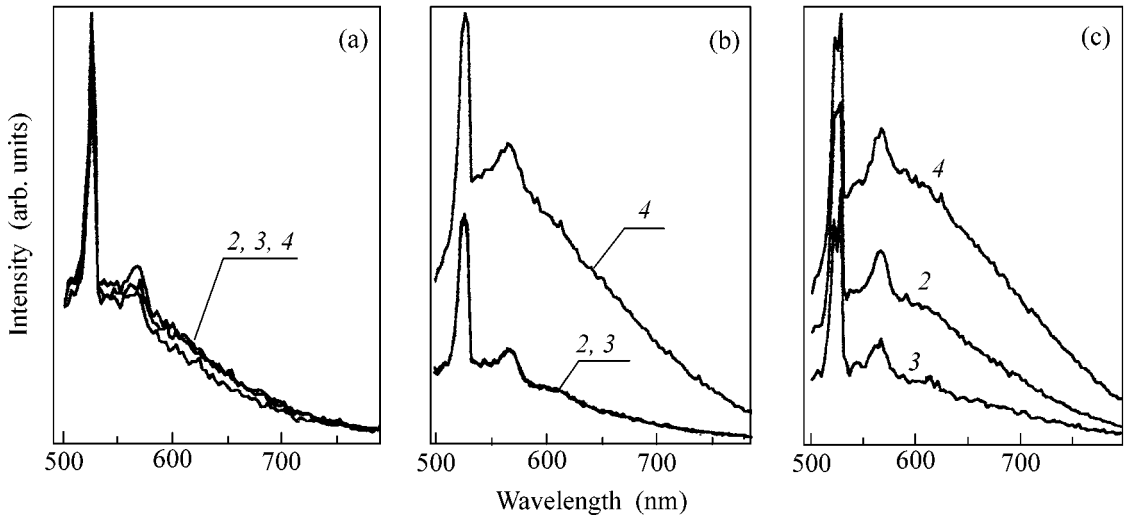

Fig. 2. PL spectra of (a) sputtered samples, (b) samples after avalanche annealing, and (c) annealed samples after anodic etching.

two features of the observed Raman spectra. First, the smallest change in the bandshape is observed for sample 1, in which the thickness of the SiC layers is twice as large as in the other samples. This fact suggests that the interaction between carbon layers influences the process of carbon structure formation. Second, the bandshapes of the Raman spectra of samples 2 and 3 differ substantially after annealing and anodic etching (Fig. 1c, curves *2*, *3*), although the thicknesses of the carbon layers differ by only 5% (1.4 and 1.34 nm). We add that the spectrum of graphite-like sample 3 (Fig. 1c, curve *3*) became similar to the Raman spectrum of a strongly disordered graphite.

The photoluminescence (PL) spectra of the synthesized samples are shown in Fig. 2. Note that the PL spectra of sample 1 remained virtually unchanged after annealing and etching and, hence, are not given in the figure. The spectra of the starting samples were almost identical (Fig. 2a). After annealing, the luminescence intensity of sample 4 increased significantly (Fig. 2b, curve *4*). The thickness of the carbon layers in this sample is close to the size of a diamond monolayer. Previ-

ously, we showed [5] that the simultaneous presence of the sp^3 and sp^2 bonds is necessary for the luminescence of carbon nanostructures. It can be assumed that the number of sp^3 bonds appeared in sample 4 upon annealing was greater than in the other samples, which led to the increase in the PL intensity. After anodic etching, the PL intensity of sample 2 increased (Fig. 2c, curve *2*). We believe that this sample must be intermediate in relation to the number of sp^3 bonds. In fact, the spectra demonstrate that graphite-like sample 3 has the lowest PL intensity, diamond-like sample 4 has the highest PL intensity, and sample 2 is intermediate in PL intensity.

Hence, based on the data of Raman and PL spectra, it may be stated that the crystal structure of carbon layers formed upon the avalanche annealing of superlattices depends on the superlattice geometrical parameters.

In summary, a method has been proposed and implemented for obtaining carbon films with a prescribed crystal modification within a unified technology. It has been shown experimentally that various modifications of the carbon crystal structure can be obtained in the superlattice layers by choosing the appropriate thickness of these layers. On the basis of this effect, the technology can be developed for obtaining carbon nanostructures with prescribed properties.

We are grateful to Prof. N.N. Sibel'din for useful discussions.

This work was supported by the Russian Foundation for Basic Research, the Federal Target Program "Integration of Higher Educational Institutions and Basic Science," Complex Scientific Problem of the Federal Target Scientific and Technical Program "Physics of Solid-State Nanostructures," the Program of the Presidium of the Russian Academy of Sciences "Low-Dimensional Quantum Structures," and the Program of the State Support of Leading Scientific Schools (project no. NSh-1923.2003.2).

REFERENCES

1. *Proceedings of 2nd International Conference on Carbon: Fundamental Problems of the Science, Materials Science, and Technology* (Moscow, 2003).
2. A. F. Plotnikov, F. A. Pudonin, and V. B. Stopachinskiĭ, Pis'ma Zh. Éksp. Teor. Fiz. **46**, 443 (1987) [JETP Lett. **46**, 560 (1987)].
3. N. N. Melnik, T. N. Zavaritskaya, M. V. Rzaev, *et al.*, Proc. SPIE **4069**, 212 (2000).
4. M. Ramsteiner and J. Wagner, Appl. Phys. Lett. **51**, 1355 (1987).
5. V. A. Karavanskiĭ, N. N. Mel'nik, and T. N. Zavaritskaya, Pis'ma Zh. Éksp. Teor. Fiz. **74**, 204 (2001) [JETP Lett. **74**, 186 (2001)].

Translated by A. Bagatur'yants

JETP Letters, Vol. 79, No. 6, 2004, pp. 286–292. From Pis'ma v Zhurnal Éksperimental'noĭ i Teoreticheskoĭ Fiziki, Vol. 79, No. 6, 2004, pp. 344–350.

Universal Behavior of Heavy-Fermion Metals Near a Quantum Critical Point¶

V. R. Shaginyan

St. Petersburg Nuclear Physics Institute, Gatchina, 188300 Russia
e-mail: vrshag@thd.pnpi.spb.ru
CTSPS, Clark Atlanta University, Atlanta, Georgia 30314, USA

Received November 24, 2003; in final form, February 9, 2004

The behavior of the electronic system of heavy-fermion metals is considered. We show that there exist at least two main types of the behavior when the system is near quantum critical point, which can be identified as the fermion condensation quantum phase transition (FCQPT). We show that the first type is represented by the behavior of a highly correlated Fermi liquid, while the second type is depicted by the behavior of a strongly correlated Fermi liquid. If the system approaches FCQPT from the disordered phase, it can be viewed as a highly correlated Fermi liquid which at low temperatures exhibits the behavior of Landau Fermi liquid (LFL). At higher temperatures *T*, it demonstrates the non-Fermi liquid (NFL) behavior which can be converted into the LFL behavior by the application of magnetic fields *B*. If the system has undergone FCQPT, it can be considered as a strongly correlated Fermi liquid which demonstrates the NFL behavior even at low temperatures. It can be turned into LFL by applying magnetic fields *B*. We show that the effective mass M^* diverges at the very point that the Neél temperature goes to zero. The *B*–*T* phase diagrams of both liquids are studied. We demonstrate that these *B*–*T* phase diagrams have a strong impact on the main properties of heavy-fermion metals, such as the magnetoresistance, resistivity, specific heat, magnetization, and volume thermal expansion. © *2004 MAIK "Nauka/Interperiodica"*.

PACS numbers: 71.27.+a; 71.10.Hf; 71.10.Ay

In heavy-fermion (HF) metals with strong electron correlations, quantum phase transitions at zero temperature may strongly influence the measurable quantities up to relatively high temperatures. These quantum phase transitions have recently attracted much attention because the behavior of HF metals is expected to follow universal patterns defined by the quantum mechanical nature of the fluctuations taking place at quantum critical points (see, e.g., [1, 2]). It is widely believed that the proximity of the electronic system of an HF metal to quantum critical points may lead to non-Fermi liquid (NFL) behavior. The system can be driven to quantum critical points (QCPs) by tuning control parameters other than temperature, for example, by pressure, by magnetic field, or by doping. When a system is close to a QCP, we are dealing with the strong coupling limit where no absolutely reliable answer can be given on pure theoretical first principle grounds. Therefore, the only way to verify what type of quantum phase transition occurs is to consider experimental facts which describe the behavior of the system. Only recently have experimental facts appeared which deliver experimental grounds to understand the nature of quantum phase transition producing the universal behavior of HF metals.

It is the very nature of HF metals that suggests that their unusual properties are defined by a quantum phase transition related to the unlimited growth of the effective mass at its QCP. Moreover, a divergence to infinity of the effective electron mass was observed at a magnetic field-induced QCP [3–5]. We assume that such a quantum phase transition is the fermion condensation quantum phase transition (FCQPT), an essential feature of which is the divergence of the effective mass M^* at its QCP [6, 7]. FCQPT takes place when the density x of a system tends to the critical density x_{FC}, so that $M^* \propto 1/r$, where r is the distance from the QCP, $r = |x - x_{FC}|$. Such a behavior does not qualitatively depend on the system's dimensions and is valid in cases of both two-dimensional (2D) and three-dimensional (3D) Fermi systems [8, 9]. Beyond FCQPT, the system possesses fermion condensation (FC) and represents a new state of electron liquid with FC [7, 10]. As soon as FCQPT occurs, the system becomes divided into two quasiparticle subsystems: the first is characterized by quasiparticles with the effective mass M^*_{FC}, while the second one is occupied by quasiparticles with mass M^*_L. The quasiparticle dispersion law in systems with FC can be represented by two straight lines, characterized by the effective masses M^*_{FC} and M^*_L and intersecting near the binding energy E_0. Properties of these

¶ This article was submitted by the author in English.

new quasiparticles with M^*_{FC} are closely related to the state of the system, which is characterized by the temperature T, pressure P, or by the presence of superconductivity. We may say that the quasiparticle system in the range occupied by FC becomes very "soft" and is to be considered as a strongly correlated liquid. Nonetheless, the basis of the Landau Fermi liquid theory [11] survives FCQPT: the low energy excitations of the strongly correlated liquid with FC are quasiparticles, while this state can be considered as a quantum protectorate [6]. The only difference between the Landau Fermi liquid and Fermi liquid after FCQPT is that we have to expand the number of relevant low energy degrees of freedom by introducing a new type of quasiparticles with the effective mass M^*_{FC} and the energy scale E_0 [6]. It is possible to provide a consistent picture of high-T_c metals as the strongly correlated Fermi liquid [12].

When a Fermi system approaches FCQPT from the disordered phase, its low energy excitations are Landau quasiparticles which can be characterized by the effective mass M^*. This mass strongly depends on the distance r, temperature, and magnetic fields B [8]. At low temperatures, it becomes a Landau Fermi liquid with the effective mass M^*, provided that $r > 0$. This state of the system, with M^* strongly depending on T, r, and B, resembles the strongly correlated liquid. In contrast to the strongly correlated liquid, there is no energy scale E_0 and the system under consideration is the Landau Fermi liquid at $T \longrightarrow 0$. Therefore, this liquid can be called a highly correlated liquid. Such a highly correlated Fermi liquid was observed in nonsuperconducting $La_{1.7}Sr_{0.3}CuO_4$ [8, 13].

In this Letter, we continue to show that, within the framework of FCQPT, it is possible to understand the NFL behavior observed in different strongly and highly correlated Fermi liquids such as high-T_c superconductors [12] and HF metals. We apply the theory of fermion condensation to describe the behavior of the electronic system of HF metals and to show that there exist at least two main types of the behavior. If the system approaches FCQPT from the disordered phase, it can be viewed as the highly correlated electron liquid and the effective mass M^* depends on temperature, $M^* \propto T^{-1/2}$. Such a dependence of M^* leads to the NFL behavior of the electronic system. The application of a magnetic field $(B - B_c) \geq B^*(T) \propto T^{3/4}$ restores Landau Fermi liquid (LFL) behavior. Here, B_c is a critical magnetic field. At $(B - B_c) \geq B^*(T)$, the effective mass depends on the magnetic field, $M^*(B) \propto (B - B_c)^{-2/3}$, being approximately independent of the temperature at $T \leq T^*(B) \propto (B - B_c)^{4/3}$. At $T \geq T^*(B)$, the $T^{-1/2}$ dependence of the effective mass and the NFL behavior are reestablished. At $T \longrightarrow 0$, the system becomes LFL with the effective mass $M^* \propto 1/r$. When the system has undergone FCQPT, it becomes a strongly correlated electron liquid and the effective mass behaves as $M^* \propto 1/T$, leading to the NFL behavior even at low temperatures. The application of a magnetic field $(B - B_c) \geq B^*(T) \propto T^2$ restores the LFL behavior. At $(B - B_c) \geq B^*(T)$, the effective mass $M^*(B) \propto (B - B_c)^{-1/2}$, being approximately independent of the temperature at $T \leq T^*(B) \propto \sqrt{B - B_c}$. At $T \geq T^*(B)$, both the $1/T$ dependence and the NFL behavior are reestablished. We show that the effective mass M^* diverges at the very point that the Neél temperature goes to zero. It is demonstrated that obtained B–T phase diagrams have a strong impact on the main properties of HF metals, such as the magnetoresistance, resistivity, specific heat, magnetization, and volume thermal expansion.

We start with the case of a highly correlated electron liquid when the system approaches FCQPT from the disordered phase. FCQPT manifests itself in the divergence of the quasiparticle effective mass M^* as the density x tends to the critical density x_{FC} or the distance $r \longrightarrow 0$ [8, 9]

$$M^* \propto \frac{1}{|x - x_{FC}|} \propto \frac{1}{r}. \tag{1}$$

Since the effective mass M^* is finite, the system exhibits the LFL behavior at low temperatures $T \sim T^*(x) \propto |x - x_{FC}|^2$ [8]. The quasiparticle distribution function $n(\mathbf{p}, T)$ is given by the equation

$$\frac{\delta\Omega}{\delta n(\mathbf{p}, T)} = \varepsilon(\mathbf{p}, T) - \mu(T) - T\ln\frac{1 - n(\mathbf{p}, T)}{n(\mathbf{p}, T)} = 0. \tag{2}$$

The function $n(\mathbf{p}, T)$ depends on the momentum $\mathbf{p}$ and the temperature T. Here, $\Omega = E - TS - \mu N$ is the thermodynamic potential and μ is the chemical potential, while $\varepsilon(\mathbf{p}, T)$,

$$\varepsilon(\mathbf{p}, T) = \frac{\delta E[n(p)]}{\delta n(\mathbf{p}, T)}, \tag{3}$$

is the quasiparticle energy. This energy is a functional of $n(\mathbf{p}, T)$ just like the total energy $E[n(p)]$, entropy $S[n(p)]$, and the other thermodynamic functions. The entropy $S[n(p)]$ is given by the familiar expression

$$S[n(p)] = -2\int [n(\mathbf{p}, T)\ln n(\mathbf{p}, T) + (1 - n(\mathbf{p}, T))\ln(1 - n(\mathbf{p}, T))]\frac{d\mathbf{p}}{(2\pi)^3}, \tag{4}$$

which results from purely combinatorial considerations. Equation (2) is usually presented as the Fermi–Dirac distribution

$$n(\mathbf{p}, T) = \left\{1 + \exp\left[\frac{(\varepsilon(\mathbf{p}, T) - \mu)}{T}\right]\right\}^{-1}. \tag{5}$$

At $T \longrightarrow 0$, one gets from Eqs. (2), (5) the standard solution $n_F(\mathbf{p}, T \longrightarrow 0) \longrightarrow \theta(p_F - p)$, with $\varepsilon(p \simeq p_F) -$

$\mu = p_F(p - p_F)/M^*$, where p_F is the Fermi momentum, $\theta(p_F - p)$ is the step function, and M^* is the Landau effective mass [11]

$$\frac{1}{M^*} = \frac{1}{p}\frac{d\varepsilon(p, T \longrightarrow 0)}{dp}\Big|_{p = p_F}. \quad (6)$$

It is implied that, in the case of LFL, M^* is positive and finite at the Fermi momentum p_F. As a result, the T-dependent corrections to M^*, to the quasiparticle energy $\varepsilon(p)$, and other quantities start with T^2 terms being approximately temperature-independent. The Landau equation relating the mass M of an electron to the effective mass of the quasiparticles is of the form [11]

$$\frac{\mathbf{p}}{M^*} = \frac{\mathbf{p}}{M} + \int F_L(\mathbf{p}, \mathbf{p}_1, x)\nabla_{\mathbf{p}_1} n(\mathbf{p}_1)\frac{d\mathbf{p}_1}{(2\pi)^3}. \quad (7)$$

Applying Eq. (7) at $T < T^*(x)$, we obtain the common result

$$M^* = \frac{M}{1 - N_0 F_L^1(x)/3}. \quad (8)$$

Here, N_0 is the density of states of the free Fermi gas and $F_L^1(x)$ is the p-wave component of the Landau interaction. At $x \longrightarrow x_{FC}$, the denominator in Eq. (8) tends to zero and one obtains Eq. (1). The temperature smoothing out the step function $\theta(p_F - p)$ at $p_F = (x/3\pi^2)^{1/3}$ induces the variation of the Fermi momentum $\Delta p_F \sim TM^*/p_F$. We assume that the amplitude F_L has a short range $q_0 \ll p_F$ of interaction in the momentum space. It is a common condition leading to the existence of FC and nearly localized Fermi liquids [7, 14]. If the radius is such that $q_0 \sim \Delta p_F \sim T_0 M^*/p_F$, corrections to the effective mass are proportional to T at $T \sim T_0$. Here, $T_0 \propto |x - x_{FC}|$ is a characteristic temperature at which the system's behavior is of the NFL type. On the other hand, at $T^*(x) \ll T_0$, we have $q_0 \gg T^*(x)M^*/p_F$ and the system behaves as LFL at $T \sim T^*(x)$, so that the corrections to the effective mass start with T^2 terms. We can also conclude that the transition region is rather large compared with $T^*(x)$, being proportional to T_0.

In the case of $T \sim T_0$, we again can use Eq. (8) with $F_L^1(p_F - \Delta p_F) \sim F_L^1(p_F) + A\Delta p_F$, where $A \propto dF_L^1(x)/dx$. Substituting this expansion of $F_L^1(p_F + \Delta p_F)$ into Eq. (8), we find that

$$M^* \sim \frac{M}{A\Delta p_F} \propto \frac{M}{M^* T}. \quad (9)$$

In deriving Eq. (9), we assumed that the system is close to FCQPT, so that $(1 - N_0 F_L^1(p_F)) \ll N_0 A\Delta p_F$. We can say that, at $T \sim T_0$, Δp_F induced by T becomes larger than the distance r from FCQPT, $\Delta p_F > |p_F^{FC} - p_F|$, where p_F^{FC} corresponds to x_{FC}. Solving Eq. (9) with respect to M^*, we obtain [8]

$$M^*(T) \propto \frac{1}{\sqrt{T}}. \quad (10)$$

The behavior of the effective mass given by Eq. (10) can be verified by measuring the thermal expansion coefficient, which is given by [15]

$$\alpha(T) = \frac{1}{3}\left(\frac{\partial(\log V)}{\partial T}\right)_P = -\frac{x}{3K}\left(\frac{\partial(S/x)}{\partial x}\right)_T. \quad (11)$$

Here, P is the pressure and V is the volume. Substituting Eq. (4) into Eq. (11), one finds that in the LFL theory coefficient is of the order of $\alpha(T) \sim M_L^* T/p_F^2 K$. By employing Eq. (10), one finds that, at $T \sim T_0$ [16],

$$\alpha(T) \propto a\sqrt{T} + bT, \quad (12)$$

with a and b being constants. This result is in good agreement with experimental facts obtained in measurements on $CeNi_2Ge_2$ [17].

The application of magnetic fields B leads to Zeeman splitting of the Fermi level. As a result, two quasiparticle distribution functions with Fermi momenta p_F^1 and p_F^2 appear, so that $p_F^1 < p_F < p_F^2$ and $\Delta p_F = (p_F^2 - p_F^1) \sim \mu_0 BM^*/p_F$. Here, μ_0 is the electron magnetic moment. In the same way Eq. (10) was derived, we can obtain the equation determining $M^*(B)$ [8]. The only difference is that there are no contributions coming from the terms proportional to Δp_F, and we have to take into account terms proportional to $(\Delta p_F)^2$. Assuming that the system is close to the critical point, we obtain

$$M^*(B) \sim M\left(\frac{\varepsilon_F}{B\mu}\right)^{2/3}. \quad (13)$$

At $T \sim T^*(x)$, Eq. (13) is valid as long as $M^*(B) \leq M^*(x)$; otherwise, we have to use Eq. (1). It follows from Eq. (13) that the application of magnetic fields reduces the effective mass. If there exists a magnetic order in the system which is suppressed by magnetic field $B = B_{c0}$, then the quantity $(B - B_{c0})$ plays the role of zero field, and Eq. (13) has to be replaced by the equation

$$M^*(B) \propto \left(\frac{1}{B - B_{c0}}\right)^{2/3}. \quad (14)$$

At high magnetic fields, we expect Eq. (14) to be invalid, because Δp_F becomes too large, so that $\Delta p_F > q_0$. In that case, the effective mass still depends on the magnetic field, but the proportionality given by Eq. (14) is not preserved, and the dependence on the magnetic field becomes weaker.

At elevated temperatures $T \sim T_0$, the effective mass starts to depend on both the temperature and the magnetic field. A crossover from the B-dependent effective mass $M^*(B)$ to the T-dependent effective mass $M^*(T)$ takes place at a transition temperature $T^*(B)$ as soon as $M^*(B) \simeq M^*(T)$. This requirement and Eqs. (10) and (14) give

$$T^*(B) \propto (B - B_{c0})^{4/3}. \quad (15)$$

At $T > T^*(x)$, Eq. (15) determines the line on the B–T phase diagram which separates the region of the LFL behavior taking place at $T < T^*(B)$ from the NFL behavior occurring at $T > T^*(B)$. At $T < T^*(B)$, the system behaves like LFL with the effective mass $M^*(B)$ and corrections to the effective mass start with T^2 terms. In accordance with the LFL theory, the specific heat $c \simeq \gamma T$, with

$$\gamma(B) \propto M^*(B) \propto (B - B_{c0})^{-2/3}. \quad (16)$$

The resistivity ρ behaves as $\rho = \rho_0 + A(B)T^2$, where the coefficient

$$A(B) \propto (M^*(B))^2 \propto (B - B_{c0})^{-4/3}. \quad (17)$$

It follows from Eqs. (16) and (17) that the Kadowaki–Woods ratio $K = A/\gamma^2$ [18] is conserved. All these results obtained from Eqs. (14)–(17) are in good agreement with experimental facts observed in measurements on the HF metal YbAgGe single crystal [19]. The critical behavior of the coefficient $A(B) \propto (B - B_{c0})^{\beta}$ at $B \longrightarrow B_{c0}$ described by Eq. (14) with $\beta = -4/3$ is in accordance with experimental data obtained in measurements on $CeCoIn_5$, which displayed the critical behavior with $\beta = -1.37 \pm 0.1$ [4].

In the LFL theory, the magnetic susceptibility $\chi \propto M^*/(1 - F_0^a)$. Note, that there is no ferromagnetic instability in Fermi systems related to the growth of the effective mass, and the relevant Landau amplitude $F_0^a > -1$ [14]. Therefore, at $T < T^*(B)$, the magnetic susceptibility turns out to be proportional to the effective mass

$$\chi(B) \propto M^*(B) \propto (B - B_{c0})^{-2/3}, \quad (18)$$

while the static magnetization $M_B(B)$ is given by

$$M_B(B) \propto B_\chi \propto (B - B_{c0})^{1/3}. \quad (19)$$

At $T > T^*(B)$, as follows from Eq. (10), Eq. (18) has to be rewritten as

$$\chi(T) \propto M^*(T) \propto \frac{1}{\sqrt{T}}. \quad (20)$$

The behavior of $\chi(B)$ and $M_B(B)$ as a function of magnetic field B given by Eqs. (18) and (19) and the behavior of $\chi(T)$, see Eq. (20), are in accordance with facts observed in measurements on $CeRu_2Si_2$ with the critical field $B_{c0} \longrightarrow 0$ [20].

Consider the system when $r \longrightarrow 0$. Then, its properties are determined by the magnetic fields B and the temperature T because there are no other parameters to describe the state of the system. At the transition temperatures $T \simeq T^*(B)$, the effective mass depends on both T and B, while at $T \ll T^*(B)$, the system is LFL with the effective mass being given by Eq. (14), and at $T \gg T^*(B)$, the mass is defined by Eq. (10). Instead of solving Eq. (8), it is possible to construct a simple interpolation formula to describe the behavior of the effective mass over all the region,

$$M^*(B, T) \propto F(B, T) = \frac{1}{c_1(B - B_{c0})^{2/3} + c_2 f(y)\sqrt{T}}. \quad (21)$$

Here, $f(y)$ is a universal monotonic function of $y = \sqrt{T}/(B - B_{c0})^{2/3}$ such that $f(y \sim 1) = 1$ and $f(y \ll 1) = 0$. It is seen from Eq. (21) that the behavior of the effective mass can be represented by a universal function F_M of only one variable y if the temperature is measured in the units of the transition temperature $T^*(B)$, see Eq. (15), and the effective mass is measured in the units of $M^*(B)$ given by Eq. (14), $F_M(y) = aF(B, T)/M^*(B)$ with a being a constant. This representation describes the scaling behavior of the effective mass. As is seen from Eqs. (19) and (21), the scaling behavior of the magnetization can be represented in the same way, provided the magnetization is normalized by the saturated value at each field given by Eq. (19),

$$\frac{M_B(B, T)}{M_B(B)} \propto \frac{1}{1 + c_3 f(y) y}, \quad (22)$$

where c_3 is a constant. It is seen from Eq. (22) that magnetization is a monotonic function of y. Upon using the definition of susceptibility, $\chi = \partial M_B/\partial B$, and differentiating both sides of Eq. (22) with respect to B, we arrive at the conclusion that the susceptibility also exhibits the scaling behavior and can be presented as a universal function of only one variable y, provided it is normalized by the saturated value at each field given by Eq. (18),

$$\frac{\chi(B, T)}{\chi(B)} \propto \frac{1}{1 + c_3 f(y) y} + 2c_3 y \frac{f(y) + y df(y)/dy}{(1 + c_3 f(y) y)^2}. \quad (23)$$

It is of importance to note that the susceptibility is not a monotonic function of y because the derivative is the sum of two contributions. The second contribution on the right-hand side of Eq. (23) makes the susceptibility have a maximum. The above behaviors of the magnetization and susceptibility are in accordance with the facts observed in measurements on $CeRu_2Si_2$ [20]. Note that the magnetic properties of $CeRu_2Si_2$ do not show any indications of the magnetic ordering at the smallest temperatures and in the smallest applied magnetic fields [20], which is $B_{c0} \longrightarrow 0$ in that case. As a result, we can conclude that the QCP is driven by the divergence of the effective mass rather than by mag-

netic fluctuations and FCQPT is the main cause of the NFL behavior. We can also conclude that the Neél temperature is zero in this case, because the magnetic susceptibility diverges at $T \longrightarrow 0$, as is seen from Eq. (20). A more detailed analysis of this issue will be published elsewhere.

Consider the case when the system has undergone FCQPT. Then, there exist special solutions of Eq. (2) associated with the so-called fermion condensation [7]. Being continuous and satisfying the inequality $0 < n_0(\mathbf{p}) < 1$ within some region in p, such solutions $n_0(\mathbf{p})$ admit a finite limit for the logarithm in Eq. (2) at $T \longrightarrow 0$ yielding [7]

$$\varepsilon(\mathbf{p}) - \mu = 0, \text{ if } 0 < n_0(\mathbf{p}) < 1; \quad p_i \le p \le p_f, \quad (24)$$

where $\varepsilon(\mathbf{p})$ is given by Eq. (3). At $T = 0$, Eq. (24) defines a new state of electron liquid with FC [7, 10] which is characterized by a flat spectrum in the $(p_f - p_i)$ region and which can strongly influence measurable quantities up to temperatures $T \ll T_f$. In this state, the order parameter of the superconducting state $\kappa(\mathbf{p}) = \sqrt{(1 - n_0(\mathbf{p}))n_0(\mathbf{p})}$ has finite values in the $(p_f - p_i)$ region, whereas the superconducting gap $\Delta_1 \longrightarrow 0$ in this region, provided that the pairing interaction tends to zero. Such a state can be considered as superconducting, with an infinitely small value of Δ_1, so that the entropy $S(T = 0)$ of this state is equal to zero [6, 7].

When $p_f \longrightarrow p_i \longrightarrow p_F$, the flat part vanishes and Eq. (24) determines the QCP at which the effective mass M^* diverges and FCQPT takes place. When the density approaches the QCP from the disordered phase, Eq. (24) possesses nontrivial solutions at $x = x_{FC}$ as soon as the effective interelectron interaction as a function of the density, or the Landau amplitude, becomes sufficiently strong to determine the occupation numbers $n(\mathbf{p})$ which deliver the minimum value to the energy $E[n(p)]$, while the kinetic energy can be considered as frustrated [6]. As a result, the occupation numbers $n(\mathbf{p})$ become variational parameters and Eq. (24) has nontrivial solutions $n_0(\mathbf{p})$, because the energy $E[n(p)]$ can be lowered by alteration of the occupation numbers. Thus, within the region $p_i < p < p_f$, the solution $n_0(\mathbf{p})$ deviates from the Fermi step function $n_F(\mathbf{p})$ in such a way that the energy $\varepsilon(\mathbf{p})$ stays constant, while outside this region, $n(\mathbf{p})$ coincides with $n_F(\mathbf{p})$ [7]. Note that a formation of the flat part of the spectrum has been confirmed in [21–23].

At $r > 0$ when the system is on the disordered side, that is, $\kappa(\mathbf{p}) \equiv 0$, and the density x moves away from QCP located at x_{FC}, the Landau amplitude $F_L(p = p_F, p_1 = p_F, x)$ as a function of x becomes smaller, the kinetic energy comes into a play and makes the flat part vanish. Obviously, Eq. (24) has only the trivial solution $\varepsilon(p = p_F) = \mu$, and the quasiparticle occupation numbers are given by the step function, $n_F(\mathbf{p}) = \theta(p_F - p)$.

At $\Delta_1 \longrightarrow 0$, the critical temperature $T_c \longrightarrow 0$. We see that the ordered phase can exist only at $T = 0$, and the state of electron liquid with FC disappears at $T > 0$ [6]. Therefore, FCQPT is not the endpoint of a line of finite-temperature phase transitions. This conclusion is in accordance with Eq. (2), which does not admit the existence of the flat part of spectrum at finite temperatures. As a result, the quantum-to-classical crossover upon approaching a finite-temperature phase transition does not exist. In the considered case, one can expect to observe such a crossover at $T \sim T_f$. On the other hand, Δ_1 becomes finite if we assume that the pairing interaction is finite and the corresponding $x - T$ phase diagram becomes richer. Moving along this line, we can consider the high-T_c superconductivity as well (see, e.g., [6, 7]).

At finite temperatures $T \ll T_f$, the occupation numbers in the region $(p_f - p_i)$ are still determined by Eq. (24) and the system becomes divided into two quasiparticle subsystems: the first subsystem is occupied by normal quasiparticles with the finite effective mass M_L^* independent of T at momenta $p < p_i$, while the second subsystem in the $(p_f - p_i)$ range is characterized by the quasiparticles with the effective mass $M_{FC}^*(T)$ [6, 24]

$$M_{FC}^* \simeq p_F \frac{p_f - p_i}{4T}. \quad (25)$$

There is an energy scale E_0 separating the slow dispersing low energy part, related to the effective mass M_{FC}^*, from the faster dispersing relatively high energy part, defined by the effective mass M_L^*. It follows from Eq. (25) that E_0 is of the form [6]

$$E_0 \simeq 4T. \quad (26)$$

The described system can be viewed as a strongly correlated one, it has the second type of the behavior and demonstrates the NFL behavior even at low temperatures. By applying magnetic fields, the system can be driven to LFL with the effective mass [25]

$$M^*(B) \propto \frac{1}{\sqrt{B - B_{c0}}}. \quad (27)$$

In the same way as it was done above, we find from Eqs. (25) and (27) that a crossover from the B-dependent effective mass $M^*(B)$ to the T-dependent effective mass $M^*(T)$ takes place at a transition temperature $T^*(B)$

$$T^*(B) \propto \sqrt{(B - B_{c0})}. \quad (28)$$

Equation (28) determines the line in the B–T phase diagram which separates the region of the LFL behavior at $T < T^*(B)$ from the NFL behavior occurring at $T > T^*(B)$. The existence of the B–T phase diagram given by Eqs. (15) and (28) can be highlighted by calculating

the resistivity and the magnetoresistance [8]. The resistivity, which at $T > T^*(B)$ demonstrates the NFL behavior, at $T < T^*(B)$, exhibits the LFL behavior, $\rho = \rho_0 + A(B)T^2$. The B–T diagram of the dependence of the effective mass on the magnetic field can be highlighted by calculating the magnetoresistance. At $(B - B_{c0}) > B^*(T)$, the magnetoresistance is negative, and at $(B - B_{c0}) < B^*(T)$, it becomes positive. This behavior of both the magnetoresistance and the resistivity is in agreement with measurements on $YbRh_2Si_2$ [3], when the system exhibits the second type of the behavior, see Eq. (28), while $CeCoIn_5$ and YbAgGe demonstrate the first type of behavior consistent with that given by Eq. (15) [4, 19].

At $T < T^*(B)$, the coefficients $\gamma \propto M^*(B)$, $\chi(B) \propto M^*(B)$, and $A(B) \propto (M^*(B))^2$, and we find that the Kadowaki ratio K arid the Sommerfeld–Wilson ratio $R \propto \chi(B)/\gamma(B)$ are preserved due to Eq. (27). The obtained B–T phase diagram and the conservation of both the Kadowaki and the Sommerfeld–Wilson ratios are in full agreement with data obtained in measurements on $YbRh_2Si_2$ and $YbRh_2(Si_{0.95}Ge_{0.05})_2$ [3, 5, 17]. Taking into account Eqs. (11) and (25), we find that in the case of the two quasiparticle subsystems the thermal expansion coefficient $\alpha(T) \propto a + bT + c\sqrt{T}$, with a, b, and c being constants. Here, the first term a is determined by the FC contribution, the second bT is given by normal quasiparticles with the effective mass M_L^*, and the third $c\sqrt{T}$ comes from a specific contribution related to the spectrum $\varepsilon_c(\mathbf{p})$ which ensures the connection between the dispersionless region $(p_f - p_i)$ occupied by FC and normal quasiparticles [16, 24]. At finite temperatures, the contribution coming from the third term is expected to be relatively small because the spectrum $\varepsilon_c(\mathbf{p})$ occupies a relatively small area in the momentum space. Since at $T \longrightarrow 0$, the main contribution to the specific heat $c(T)$ comes from the spectrum $\varepsilon_c(\mathbf{p})$, the specific heat behaves as $c(T) \propto a_1\sqrt{T} + b_1T$, with a_1 and b_1 being constants. The second term b_1T comes from the contribution given by FC and normal quasiparticles. Measurements for $YbRh_2(Si_{0.95}Ge_{0.05})_2$ show a power low divergence of $\gamma = c/T \propto T^{-\alpha}$ with $\alpha = 1/3$ [17]. This result is in reasonable agreement with our calculations giving $\alpha = 0.5$. At lower temperatures, the relative contribution of the first term $a_1\sqrt{T}$ becomes bigger and we expect that the agreement will also become better. Now, we find that the Grüneisen ratio $\Gamma(T) = \alpha(T)/c(T)$ diverges as $\Gamma(T) \propto 1/\sqrt{T}$ [16]. This result is in good agreement with measurements on $YbRh_2(Si_{0.95}Ge_{0.05})_2$ [5, 17].

As follows from Eq. (27), the static magnetization behaves as $M_B(B) \propto \sqrt{B - B_{c0}}$, in accordance with measurements on $YbRh_2(Si_{0.95}Ge_{0.05})_2$ [5]. We can also conclude that Eqs. (21)–(23) determining the scaling behavior of the effective mass, static magnetization, and the susceptibility are also valid in the case of strongly correlated liquid, but the variable y is now given by $y = T/\sqrt{B - B_{c0}}$, while the function $f(y)$ can be dependent on $(p_f - p_i)/p_F$. This dependence comes from Eq. (25). As a result, we can find that at $T < T^*(B)$, the factor $d\rho/dT \propto A(B)T$ behaves as $A(B)T \propto T/(B - B_{c0})$, and at $T > T^*(B)$, it behaves as $A(B)T \propto 1/T$. These observations are in good agreement with the data obtained in measurements on $YbRh_2(Si_{0.95}Ge_{0.05})_2$ [5].

It is worthy to note that, in zero magnetic fields, the Neél temperature is zero at FCQPT, because, as follows from Eq. (10), the effective mass tends to infinity at FCQPT and makes the susceptibility divergent. On the other hand, if there is the magnetic order and the Neél temperature is not equal to zero, the effective mass is finite and there is no FCQPT. As soon as the magnetic order is suppressed at $B \longrightarrow B_{c0}$, that is, the Neél temperature tends to zero, the effective mass $M^*(B) \longrightarrow \infty$, as follows from Eq. (14). If the system has undergone FCQPT, again at $B \longrightarrow B_{c0}$, the Neél temperature goes to zero and $M^*(B) \longrightarrow \infty$, see Eq. (27). If $B_{c0} = 0$, the effective mass diverges at $T \longrightarrow 0$, see Eq. (25), and the susceptibility χ tends to infinity, being proportional to the effective mass. In this case, the Neél temperature is equal to zero as well. Therefore, one may say that the effective mass M^* diverges at the very point that the Neél temperature goes to zero.

A few remarks are in order at this point. To describe the behavior of HF metals, we have introduced the system of quasiparticles, as is done in the Landau theory of normal Fermi liquids, where the existence of fermionic quasiparticles is a generic property of normal Fermi systems independent of microscopic details. As we have seen, at $T \ll T_f$, these quasiparticles have universal properties which determine the universal behavior of HF metals. One can use another approach, constructing the singular part of the free energy, introducing notions of the upper critical dimension, hyperscaling, etc. (see, e.g., [1, 2]). Moving along this way, one may expect difficulties. For example, having only the singular part, one has to describe at least the two types of the behavior. We reserve a consideration of these items for future publications.

In conclusion, we have shown that our simple model based on FCQPT explains the critical behavior observed in different HF metals. In the case of such HF metals as $CeNi_2Ge_2$, $CeCoIn_5$, YbAgGe, and $CeRu_2Si_2$, the behavior can be explained by the proximity to FCQPT, where their electronic systems behave like highly correlated liquids. In the case of such HF metals as $YbRh_2(Si_{0.95}Ge_{0.05})_2$ and $YbRh_2Si_2$, the critical behavior is different. This can be explained by the presence of FC in the electronic systems of these metals, i.e., by the fact that the electronic systems have undergone FCQPT and behave as strongly correlated liquids.

We have shown that the basis of the Landau Fermi liquid theory survives in both cases: the low energy excitations of both strongly correlated Fermi liquid with FC and the highly correlated Fermi liquid are quasiparticles. It is also shown that the effective mass M^* diverges at the very point that the Neél temperature goes to zero. The B–T phase diagrams of both the highly correlated liquid and the strongly correlated one have been studied. We have shown that these B–T phase diagrams strongly influence the effective mass and such important properties of HF metals as magnetoresistance, resistivity, specific heat, magnetization, susceptibility, and volume thermal expansion.

I thank P. Coleman for valuable comments. I am grateful to the CTSPS for hospitality during my stay in Atlanta. This work was supported in part by the Russian Foundation for Basic Research, no. 04-02-16136.

REFERENCES

1. S. Sachdev, *Quantum Phase Transitions* (Cambridge Univ. Press, Cambridge, 1999).
2. M. Vojta, Rep. Prog. Phys. **66**, 2069 (2003).
3. P. Gegenwart, J. Custers, C. Geibel, *et al.*, Phys. Rev. Lett. **89**, 056402 (2002).
4. J. Paglione, M. A. Tanatar, D. G. Hawthorn, *et al.*, Phys. Rev. Lett. **91**, 246405 (2003); J. Paglione *et al.*, cond-mat/0304497.
5. J. Custers, P. Gegenwart, H. Wilhelm, *et al.*, Nature **424**, 524 (2003).
6. M. Ya. Amusia and V. R. Shaginyan, Pis'ma Zh. Éksp. Teor. Fiz. **73**, 268 (2001) [JETP Lett. **73**, 232 (2001)]; S. A. Artamonov and V. R. Shaginyan, Zh. Éksp. Teor. Fiz. **119**, 331 (2001) [JETP **92**, 287 (2001)]; M. Ya. Amusia and V. R. Shaginyan, Phys. Rev. B **63**, 224507 (2001); V. R. Shaginyan, Physica B & C (Amsterdam) **312–313**, 413 (2002).
7. V. A. Khodel and V. R. Shaginyan, Pis'ma Zh. Éksp. Teor. Fiz. **51**, 488 (1990) [JETP Lett. **51**, 553 (1990)]; V. A. Khodel, V. R. Shaginyan, and V. V. Khodel, Phys. Rep. **249**, 1 (1994).
8. V. R. Shaginyan, Pis'ma Zh. Éksp. Teor. Fiz. **77**, 104 (2003) [JETP Lett. **77**, 99 (2003)]; Pis'ma Zh. Éksp. Teor. Fiz. **77**, 208 (2003) [JETP Lett. **77**, 178 (2003)].
9. V. M. Galitsky and V. A. Khodel, cond-mat/0308203; V. M. Yakovenko and V. A. Khodel, Pis'ma Zh. Éksp. Teor. Fiz. **78**, 850 (2003) [JETP Lett. **78**, 398 (2003)]; cond-mat/0308380.
10. G. E. Volovik, Pis'ma Zh. Éksp. Teor. Fiz. **53**, 208 (1991) [JETP Lett. **53**, 222 (1991)].
11. L. D. Landau, Zh. Éksp. Teor. Fiz. **30**, 1058 (1956) [Sov. Phys. JETP **3**, 920 (1956)].
12. M. Ya. Amusia and V. R. Shaginyan, Pis'ma Zh. Éksp. Teor. Fiz. **76**, 774 (2002) [JETP Lett. **76**, 651 (2002)].
13. S. Nakamae, K. Behnia, N. Mangkorntong, *et al.*, Phys. Rev. B **68**, 100502(R) (2003).
14. M. Pfitzner and P. Wölfe, Phys. Rev. B **33**, 2003 (1986).
15. L. D. Landau and E. M. Lifshitz, *Course of Theoretical Physics*, Vol. 5: *Statistical Physics*, 3rd ed. (Nauka, Moscow, 1976; Addison-Wesley, Reading, MA, 1970), Part 1.
16. M. Ya. Amusia, A. Z. Msezane, and V. R. Shaginyan, Phys. Lett. A **320**, 459 (2004).
17. R. Küchler, N. Oeschler, P. Gegenwart, *et al.*, Phys. Rev. Lett. **91**, 066405 (2003).
18. K. Kadowaki and S. B. Woods, Solid State Commun. **58**, 507 (1986).
19. S. L. Bud'ko, E. Q. Morosan, and P. C. Canfield, Phys. Rev. B (in press); cond-mat/0308517.
20. D. Takahashi, S. Abe, H. Mizuno, *et al.*, Phys. Rev. B **67**, 180407(R) (2003).
21. I. E. Dzyaloshinskii, J. Phys. I **6**, 119 (1996).
22. D. Lidsky, J. Shiraishi, Y. Hatsugai, and M. Kohmoto, Phys. Rev. B **57**, 1340 (1998).
23. V. Yu. Irkhin, A. A. Katanin, and M. I. Katsnelson, Phys. Rev. Lett. **89**, 076401 (2002).
24. M. V. Zverev, V. A. Khodel', V. R. Shaginyan, and M. Baldo, Pis'ma Zh. Éksp. Teor. Fiz. **65**, 828 (1997) [JETP Lett. **65**, 863 (1997)].
25. Yu. G. Pogorelov and V. R. Shaginyan, Pis'ma Zh. Éksp. Teor. Fiz. **76**, 614 (2002) [JETP Lett. **76**, 532 (2002)].

JETP Letters, Vol. 79, No. 6, 2004, pp. 293–297. Translated from Pis'ma v Zhurnal Éksperimental'noĭ i Teoreticheskoĭ Fiziki, Vol. 79, No. 6, 2004, pp. 351–355.

Ballistic Electron Wave Functions and Negative Magnetoresistance in a Small Ring Interferometer

O. A. Tkachenko*, V. A. Tkachenko, and D. G. Baksheev

Institute of Semiconductor Physics, Siberian Division, Russian Academy of Sciences, Novosibirsk, 630090 Russia

**e-mail: otkach@isp.nsc.ru*

Received December 11, 2003; in final form, February 12, 2004

By two-dimensional ballistic magnetotransport calculations, it is demonstrated that large-scale resistance peaks, typical of small ring interferometers in zero magnetic field, are suppressed at $B \sim 1$ T. This result is explained by the peculiarities of the interference pattern at the confluence sites of quantum wires and is in qualitative agreement with experimental data. © *2004 MAIK "Nauka/Interperiodica".*

PACS numbers: 73.23.Ad; 73.63.Nm

An ideal ring interferometer is a device consisting of one-dimensional quantum wires. The first theoretical publications [1, 2], in which the points of connection of quantum-wire leads with the ring were assumed to be structureless and the wires were considered as homogeneous, predicted a periodic 100% conductance modulation in a varying magnetic field, i.e., the Aharonov–Bohm (AB) oscillations. The origin of the effect is in the passage through the ring resonance levels. However, in reality, the AB oscillations [3–5] have a much smaller amplitude and, in some cases, are observed against the background of large-scale features in the conductance [5–8]. Another effect that is often observed in experimental measurements is the presence of a negative magnetoresistance [7–12].

Obviously, a real interferometer is much more complicated than the one-dimensional model because of the finite wire width and because of the formation of deep triangular potential wells, i.e., quantum dots, at the sites of wire separation into the ring arms. According to the self-consistent calculations of the three-dimensional electrostatic potential and electron density [6, 8, 13], these quantum dots have many single-particle levels, which should affect the transmission through the interferometer. Calculations performed for a two-dimensional ballistic transport in zero magnetic field show that the triangular dots cause additional reflection and even interferometer blocking. This conclusion follows from the comparison of the arrangements of large-scale peaks and dips in the energy dependence of transparency for the whole device and for one triangular dot [6, 8].

A similar sequence of quasiperiodic resistance peaks in the gate-voltage dependence was experimentally obtained for small ring interferometers (r = 130 nm) [7, 8]. It was found that a large negative magnetoresistance is present in the region of conductance dips and that the conductance approaches the value $\sim 2e^2/h$ as the magnetic field grows [9]. An explanation of all these facts requires numerical investigation of the magnetic-field effect on the behavior of a ballistic electron in a realistic potential of the interferometer. Note that the magnetotransport in an interferometer was modeled earlier using simple modeling potentials that neglect the electrostatics of the structure [14, 15].

In this paper, we study the wave functions and the magnetotransport in small interferometers, for which the effect of triangular dots is most pronounced. We show that, in zero magnetic field, the Fermi-energy dependence of the conductance of a single-mode interferometer consists of the alternating portions with high, $G \approx 2e^2/h$, and low, $G \ll 2e^2/h$, transparencys. In the region of a triangular dot, the wave functions corresponding to the low-conductance intervals have a symmetry that suppresses the transmission of a ballistic electron into the ring arms. Magnetic field violates this symmetry and increases the transmission probability through the interferometer.

To calculate the interferometer transparency, we used the method described in [16] and representing the extension of the recursive Green's-function technique [17]. This method allows the Schrödinger equation in a magnetic field to be solved for the realistic potentials of a complex geometry. The advantage of the method [16] is that the matrices of transmission and reflection amplitudes and the wave functions are calculated simultaneously for each point of a grid used for the discretization of the computational region. The stability is an important feature of this method. The conductance of the device is determined from the multichannel Landauer–Büttiker formula [18]. The two-dimensional effective potential necessary for calculating the conductance and wave functions was obtained by modeling three-dimensional electrostatics of an interferometer fabricated by etching on the basis of a GaAs/AlGaAs heterostructure [6]. The lithographic dimensions were

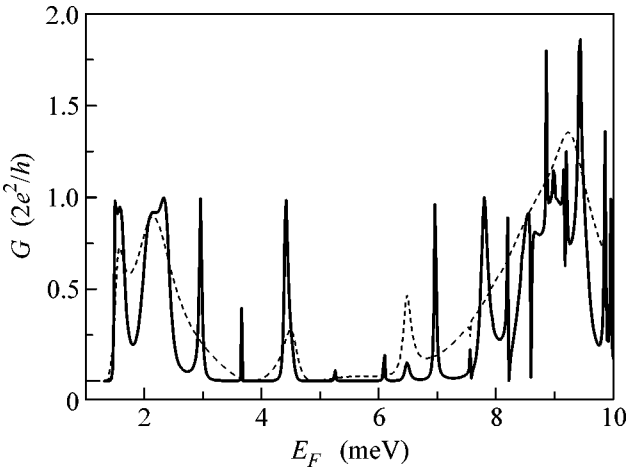

Fig. 1. Conductances calculated for a small symmetric interferometer T_{ring} (solid line) and for a triangular quantum dot T_{dot} (dashed line) as functions of the Fermi energy at $B = 0$.

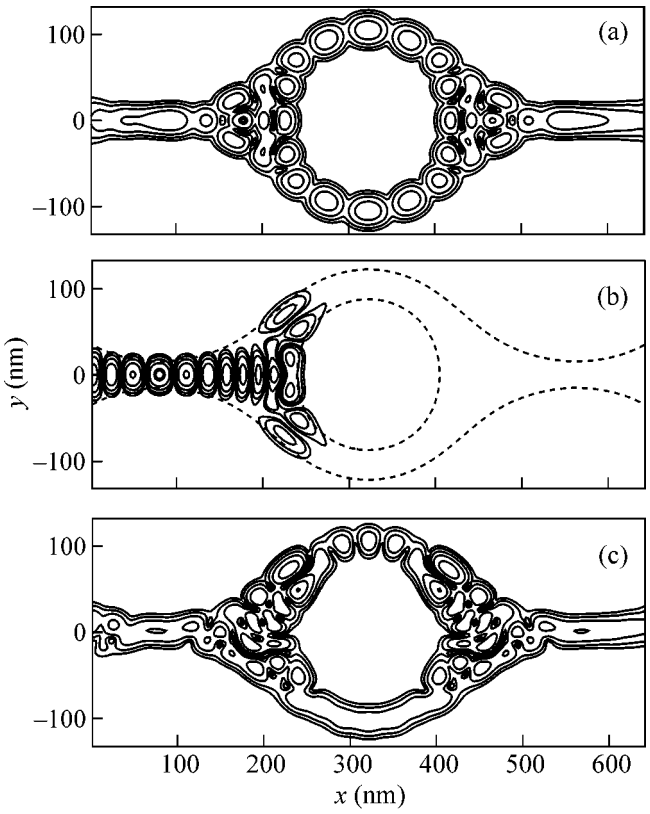

Fig. 2. Probability density distribution in an electron wave incident in the first mode: (a) the interferometer transparency is $T_{ring} = 0.99$ at $E_F = 2.34$ meV and $B = 0$; (b) $T_{ring} = 1.5 \times 10^{-4}$ at $E_F = 5.66$ meV and $B = 0$ (the dashed lines show the boundaries of the classically allowed region $E_F = U_{eff}$); (c) $T_{ring} = 1$ at $E_F = 5.62$ meV and $B = 1$ T. The probability-density isolines correspond to the levels of 0.01, 0.0316, 0.1, 0.316, and 1 and to the maximal values (a) 1.2, (b) 1.4, and (c) 2.3.

taken smaller than in the cited publication (the average ring radius was $r = 105$ nm). For simplicity, we chose a symmetric etch profile and ignored the fluctuation impurity potential (uniform doping). In our case, the channel widths in the narrowest parts of the ring and between the ring and reservoirs with 2D electron gas were approximately the same and rather small. This made it possible to obtain a single-mode regime simultaneously for all constrictions over a sufficiently large energy interval from 1.3 to 8 meV. The lower boundary of the interval corresponds to the first transverse-quantization level in the narrow part of the interferometer input channel, and the upper boundary corresponds to the second level in the ring arms. The choice of this situation is motivated by the following reasons. If the channels connecting the ring with reservoirs become much narrower than the ring-arm channels and have tunnel barriers, a single-electron charging of a multimode ring becomes possible [19]. The opposite condition leads to the case where two open triangular dots are separated by the tunnel barriers formed in the ring arms. Evidently, both these tunneling situations make the device transparency rather low. However, these cases could hardly be realized in experiment [9], because, in a magnetic field of ~ 1 T, the interferometer conductance was close to $2e^2/h$ in a considerable portion of the gate-voltage interval, which is impossible in the tunneling regime.

The calculated dependence $T_{ring}(E_F)$ of the interferometer transparency on the energy of ballistic electrons shows that, in zero magnetic field, the transmission peaks alternate with deep dips (Fig. 1). For comparison, we calculated the transparency $T_{dot}(E_F)$ of a half of the interferometer (the outgoing wave is assumed to propagate through two parallel channels extending the ring arms). One can see that two curves, on the whole, correlate with each other, and additional resonances on the curve $T_{ring}(E_F)$ obtained for the interferometer appear as a result of a circular motion in the ring. The question arises of why the interferometer conductance has wide and deep dips in the region 1.3–8 meV in zero magnetic field while the transparency of the ring arms and the connecting channels is close to its total value.

Let us consider the plots of probability density in the interferometer for the states corresponding to the total transmission (Fig. 2a) and total reflection (Fig. 2b). We assume that electrons are incident from the left in the first transverse-motion mode. Since the ring and the triangular dots have a small size and the energy of the incident particles is low, the transmission is determined by quantum interference. The state with the energy $E_F = 2.34$ meV corresponds to the resonant transmission with $T_{ring} = 0.99$ through the combined dot–ring system. One can see from Fig. 2a that the wave function is delocalized over the whole system, and the standing wave along the ring contains 16 antinodes.

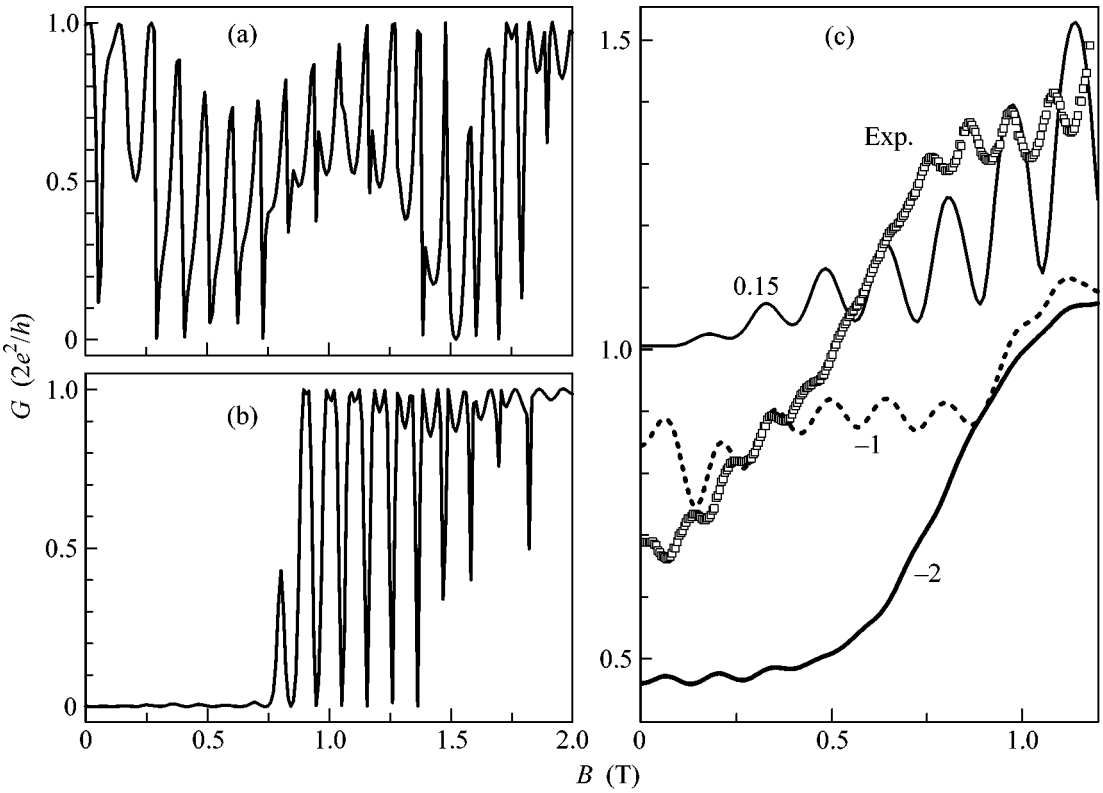

Fig. 3. Interferometer conductance as a function of magnetic field for Fermi energy E_F = (a) 2.34 and (b) 5.6 meV. (c) Effects of negative magnetoresistance and suppression of AB oscillations observed for an asymmetric ring in [11]. The values of E_F are indicated in millielectron volts near the calculated curves. The experimental curve taken from [11] is presented for comparison.

Now, we consider the state with $E_F = 5.66$ meV and $T_{\text{ring}} = 1.5 \times 10^{-4}$ (Fig. 2b), which corresponds to a suppressed transmission. In zero magnetic field, the wave function represents a standing wave that arises between the antidot and the reservoir and has a symmetry forbidding the transmission into the ring arms at the first triangular dot. Specifically, two maxima of the probability density at the arm input correspond to the second transverse-motion mode. This mode, being not mixed with the first one, is totally reflected, because its transmission through the narrow parts of the channels is not allowed. Figure 2b shows that electron tunnels at a small depth into the classically forbidden region of the two-dimensional effective potential $E_F < U_{\text{eff}}$. Similar pictures of probability density also occur for other states of minimal transmission at $B = 0$ ($E_F = 3.83$ meV or $E_F = 4.9$ meV). Note that, in symmetric single-mode interferometers that have no quantum wells at the channel-confluence sites, the reflection states in zero magnetic field appear only as a result of the destructive wave interference at the ring output [15]. In this case, the electron distribution density in the ring is always nonzero [20]. By contrast, we investigate the reflection states corresponding to the case where an electron does not penetrate into the ring at all, although the first-mode motion is open. An increase in a magnetic field breaks the symmetry in the positions of the probability-density maxima at the ring-input triangular dot, and the transmission probability through the interferometer increases. Figure 2c represents the state of total transmission in the magnetic field $B = 1$ T for $E_F = 5.62$ meV.

The magnetic-field effect manifests itself in the AB oscillations (Fig. 3a) and in the negative magnetoresistance (Fig. 3b). Note that the one-dimensional interferometer model gives the AB oscillations with a full amplitude modulation and a period corresponding to the flux quantum through the ring [1, 2]. Similar results were obtained by a simplified two-dimensional modeling of single-mode ring interferometers [14, 15]. However, the calculation for a realistic interferometer potential gives a qualitatively different result. For the half-integer magnetic flux quanta, the conductance of a symmetric interferometer with a finite channel width is not suppressed to zero, as was predicted by the one-dimensional model. The presence of levels in triangular dots and their displacement from the ring levels in a magnetic field is seen in the $G(B)$ curve as a large-scale conductance modulation and as Fano profiles of the peak–dip type. Because of the presence of Fano resonances, the form of the AB oscillations is not sinusoidal and the period and phase vary. Calculations show that, for the states with $T_{\text{ring}} = 1$ at $B = 0$, despite the large-scale conductance modulation, the transmission remains, on the

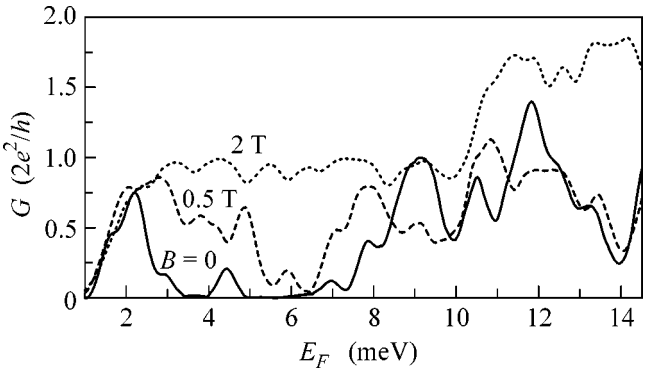

Fig. 4. Dependence of the conductance at the Fermi energy for the ring, shown in Fig. 2, in magnetic fields $B = 0$, 0.5, and 2 T at a temperature of 1.5 K.

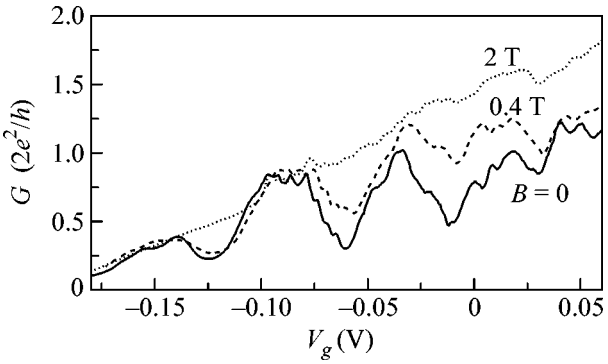

Fig. 5. Experimental dependence of the conductance on the gate voltage for a small ring at a temperature of 1.5 K. The dependence is plotted using the data reported in [9].

average, high with an increase in the magnetic field. However, the states corresponding to the total reflection become more transparent in a magnetic field. One can see from Fig. 3b that the conductance $G(B)$ grows with increasing magnetic field and reaches the value $2e^2/h$ even at $B \approx 1$ T. Thus, at the given energy, we obtain the giant negative magnetoresistance effect. For other states of minimal transmission at $B = 0$, a similar behavior takes place for $G(B)$.

As for the amplitude of AB oscillations, it depends in a complicated way on the Fermi energy, magnetic field, and the degree of ring asymmetry. The effect of AB-oscillation suppression upon passing to a tunneling regime in one of the ring arms was analyzed in our previous papers [8, 11] (together with the corresponding experimental data). Figure 3c shows the conductance $G(B)$ calculated for different Fermi energies of a small interferometer (r = 110 nm) with different channel widths in the ring. The first mode opens in one of the ring arms at $E_F = -1$ meV, while the other arm is open for the transmission of two modes. At $E_F = -2$ meV, the ring is interrupted by a tunnel barrier and the AB oscillations are suppressed. At $E_F = -1$ meV, the AB oscillations show a 5% modulation, and, at $E_F \approx 0$, a modulation from 7 to 10% (in the experiment, a 5% modulation is observed). It follows from the analysis of Fig. 3 that the model of a symmetric single-mode interferometer exaggerates the effects of AB oscillations and negative magnetoresistance, compared to the experiment [9]. However, when the fluctuation potential [8, 13] and the nanolithography errors [8, 11] are taken into account, the results of calculations become closer to the measurements [11].

Figure 4 shows the dependences of conductance on the Fermi energy, averaged for an effective temperature of T = 1.5 K. The dependences are obtained for different magnetic fields and correspond to the conditions of experiments with small rings [7–9]. One can see that the deep dips typical for conductance $G(E_F)$ in low magnetic fields begin to blur at B = 0.5 T. At B = 2 T, the edge current states start to form (the asymptotic values of $2e^2/h$ and $4e^2/h$ are approached). For comparison, Fig. 5 shows the experimental results reported in [9]. The measured dependence of the conductance of a small interferometer on the gate voltage V_g at $B = 0$ shows dips that can be related to the conductance dips in Fig. 4. One can see that, in the case of modeling and in the experiment, the dips decrease with increasing magnetic field in a similar way. The electrostatic calculation allows us to compare the lengths of the intervals of E_F and V_g, within which a qualitatively similar behavior of conductances is observed. In the calculations, a 0.05-V variation of the upper gate voltage V_g causes an approximately 5.5-meV shift of one-dimensional subbands in the channels of symmetric interferometer. Hence, the values obtained for the lengths of the single-mode motion intervals ($G \le 2e^2/h$) in the calculations and measurements are in good agreement.

Thus, the two-dimensional modeling of the transmission through a small interferometer in the single-mode regime predicts high-resistance peaks caused by the backscattering of a ballistic electron in the triangular quantum dots. With an increase in a magnetic field, the height of these peaks decreases because of the increase in the probability of electron penetration into the ring arms. This effect may be the cause of the negative magnetoresistance observed in the experiments [7–11]. We have also shown that the amplitude of AB oscillations nonmonotonically depends on the Fermi energy, magnetic field, and the degree of ring asymmetry. When one of the ring arms switches to the tunneling regime, the AB oscillations become suppressed.

We are grateful to M.V. Éntin, Z.D. Kvon, A.A. Bykov, and J.C. Portal for discussions and to A.K. Bakarov for providing us with the experimental data from previous publications. This work was supported by the Russian Foundation for Basic Research (project no. 16516), the Federal Target Scientific and Technical Program “Physics of Solid-State Nanostructures” (project no. 01.40.01.09.04), and the program of

the Russian Academy of Sciences "Low-Dimensional Quantum Structures."

REFERENCES

1. M. Büttiker, Y. Imry, and R. Landauer, Phys. Lett. A **96A**, 365 (1983); Y. Gefen, Y. Imry, and M. Ya. Azbel, Phys. Rev. Lett. **52**, 129 (1984); M. Büttiker, Y. Imry, and M. Ya. Azbel, Phys. Rev. A **30**, 1982 (1984).
2. Jian-Bai Xia, Phys. Rev. B **45**, 3593 (1992).
3. G. Timp, A. M. Chang, J. E. Cunningham, *et al.*, Phys. Rev. Lett. **58**, 2814 (1987); C. J. B. Ford, A. B. Fowler, J. M. Hong, *et al.*, Surf. Sci. **229**, 307 (1990); K. Ismail, S. Washburn, and K. Y. Lee, Appl. Phys. Lett. **59**, 1998 (1991); A. A. Bykov, Z. D. Kvon, E. B. Ol'shanetskiĭ, *et al.*, Pis'ma Zh. Éksp. Teor. Fiz. **57**, 596 (1993) [JETP Lett. **57**, 613 (1993)].
4. Z. D. Kvon, L. V. Litvin, V. A. Tkachenko, and A. L. Aseev, Usp. Fiz. Nauk **169**, 471 (1999) [Phys. Usp. **42**, 402 (1999)].
5. A. A. Bykov, Z. D. Kvon, E. B. Olshanetsky, *et al.*, Physica E (Amsterdam) **2**, 519 (1998).
6. O. A. Tkachenko, V. A. Tkachenko, D. G. Baksheev, *et al.*, Pis'ma Zh. Éksp. Teor. Fiz. **71**, 366 (2000) [JETP Lett. **71**, 255 (2000)].
7. A. A. Bykov, D. G. Baksheev, L. V. Litvin, *et al.*, Pis'ma Zh. Éksp. Teor. Fiz. **71**, 631 (2000) [JETP Lett. **71**, 434 (2000)].
8. V. A. Tkachenko, A. A. Bykov, D. G. Baksheev, *et al.*, Zh. Éksp. Teor. Fiz. **124**, 351 (2003) [JETP **97**, 317 (2003)].
9. A. A. Bykov, D. V. Nomokonov, A. K. Bakarov, *et al.*, Pis'ma Zh. Éksp. Teor. Fiz. **78**, 36 (2003) [JETP Lett. **78**, 30 (2003)].
10. C. H. Yang, M. J. Yang, K. A. Cheng, and J. C. Culbertson, Phys. Rev. B **66**, 115306 (2002).
11. V. A. Tkachenko, Z. D. Kvon, D. V. Shcheglov, *et al.*, Pis'ma Zh. Éksp. Teor. Fiz. **79**, 168 (2004) [JETP Lett. **79**, 136 (2004)].
12. O. Estibals, Z. D. Kvon, J. C. Portal, *et al.*, Physica E (Amsterdam) **13**, 1043 (2002).
13. V. A. Tkachenko, Z. D. Kvon, O. A. Tkachenko, *et al.*, Pis'ma Zh. Éksp. Teor. Fiz. **76**, 850 (2002) [JETP Lett. **76**, 720 (2002)].
14. T. Nakanishi and T. Ando, Phys. Rev. B **54**, 8021 (1996).
15. K. N. Pichugin and A. F. Sadreev, Phys. Rev. B **56**, 9662 (1997).
16. T. Usuki, M. Saito, M. Takatsu, *et al.*, Phys. Rev. B **52**, 8244 (1995).
17. T. Ando, Phys. Rev. B **44**, 8017 (1991).
18. Ya. M. Blanter and M. Büttiker, Phys. Rep. **336**, 1 (2000).
19. A. Fuhrer, S. Lüsher, T. Ihn, *et al.*, Nature **413**, 822 (2001).
20. E. K. Heller and F. C. Jain, J. Appl. Phys. **87**, 8080 (2000).

Translated by E. Golyamina

JETP Letters, Vol. 79, No. 6, 2004, pp. 298–303. Translated from Pis'ma v Zhurnal Éksperimental'noĭ i Teoreticheskoĭ Fiziki, Vol. 79, No. 6, 2004, pp. 356–361.

Terahertz Spectroscopy with a Josephson Oscillator and a SINIS Bolometer

M. Tarasov[1, 4], L. Kuz'min[2, 4], E. Stepantsov[3, 4], I. Agulo[4], A. Kalabukhov[2, 4], M. Fominskii[1, 4], Z. Ivanov[4], and T. Claeson[4]

[1] *Institute of Radio Engineering and Electronics, Russian Academy of Sciences, Fryazino, Moscow region, 114112 Russia*
[2] *Moscow State University, Moscow, 119899 Russia*
[3] *Shubnikov Institute of Crystallography, Russian Academy of Sciences, Moscow, 117333 Russia*
[4] *Chalmers University of Technology, Gothenburg, Sweden*

Received January 26, 2004; in final form, February 17, 2004

The voltage response of a thin-film normal-metal hot-electron bolometer based on a SINIS (superconductor–insulator–normal metal–insulator–superconductor) structure to the radiation of a high-temperature Josephson junction in the terahertz frequency region was measured. Bolometers were integrated with planar log-periodic and double-dipole antennas, and Josephson junctions were integrated with log-periodic antennas. Measurements showed that the Josephson junction at a temperature of 260 mK was overheated by the transport current, so that its electron temperature exceeded 3 K at a bias voltage of 1 mV. The maximum response of a bolometer with a double-dipole antenna was observed at a frequency of 300 GHz, which agreed well with the calculated value. The Josephson radiation was observed at frequencies up to 1.7 THz. The voltage response of a bolometer reached 4×10^8 V/W, and the total noise-equivalent power reached 1.5×10^{-17} W/Hz$^{1/2}$. © *2004 MAIK "Nauka/Interperiodica".*

PACS numbers: 74.50.+r; 07.57.Kp; 85.25.Pb

1. SINIS bolometers. Normal-metal hot-electron bolometers with a capacitive decoupling of the superconductor–insulator–normal metal–insulator–superconductor (SINIS) structure were proposed in [1] and experimentally tested in [2]. The response to an external microwave signal and the noise-equivalent power of such a bolometer are determined by its electron temperature. To improve the noise and signal characteristics, a direct electron cooling of a normal-metal absorber by a superconductor–insulator–normal metal (SIN) tunnel junction was proposed in [3]. The electron cooling effect was demonstrated in [4] and further developed in [5].

A general view of a substrate with bolometers is presented in Fig. 1a. A broadband log-periodic antenna with a frequency range of 0.2–2 THz is positioned at the center of the substrate; two double-dipole antennas with a central frequency of 300 GHz are on the right, and one double-dipole antenna with a central frequency of 600 GHz is on the left. At the top and bottom, test structures are positioned with two pairs of SIN junctions for studying the electron cooling effect. The latter is described for such a structure in [6]. An atomic-force microscopic image of the central part of the bolometer is shown in Fig. 1b.

The first step in fabricating the samples was the formation of gold contact pads and traps for hot quasiparticles. The pattern was made by standard photolithography. Gold 60 nm in thickness was deposited by thermal evaporation. The next step consisted in the formation of the tunnel junctions and the absorber. The pattern was made by direct electron lithography. The films were deposited by thermal evaporation at different angles through a suspended double-photoresist mask. This method made it possible to deposit films of different metals in a single process in vacuum and provide their overlap in the tunnel junction regions. A 65-nm-thick aluminum film was deposited at an angle of 60° to the substrate and oxidized for 2 min in oxygen at a pressure of 0.1 mbar to obtain a tunnel barrier. A double-layer absorber film consisting of chromium and copper with a total thickness of 75 nm was deposited perpendicular to the substrate. The absorber volume was 0.18 μm^3. The outer cooling SIN junctions of the test structures had a resistance of 0.86 kΩ each, and the inner junctions had 5.3 kΩ each. The inner junctions had a simple crosslike geometry, where a segment of a normal-metal strip crossed the oxidized aluminum electrode. Their overlap area was 0.2×0.3 μm. The structure of the outer junctions was such that the ends of the normal-metal absorber covered the corner of each of the outer oxidized aluminum electrodes, and the junction area was 0.55×0.82 μm. An increase in the size of aluminum electrodes made it possible to improve the diffusion of hot quasiparticles carried away from the absorber by the tunneling current and to avoid a reabsorption in the normal metal for the phonons emitted upon quasiparticle recombination. Additionally, for the

same purpose, one of the test structures had hot-particle traps in the form of normal-metal films located in the junction region under the aluminum film. In the experiments with electron cooling, the application of a bias voltage close to the energy gap of the outer SIN junctions caused a decrease in the electron temperature measured by the inner SIN thermometers from 260 to 100 mK.

2. High-temperature Josephson oscillators. According to [7, 8], the maximal Josephson-oscillation frequency and power are determined by the critical current I_c, the normal resistance R_n, and their product $V_c = I_cR_n$. The characteristic frequency of a Josephson junction is $f_c = (2e/h)V_c$, where e is the electron charge and h is the Planck's constant. The characteristic voltage of a Josephson junction does not exceed the energy gap, which corresponds to frequencies on the order of 700 GHz for niobium junctions, while, for high-T_c superconductors (HTSCs) with a critical temperature above 77 K, the corresponding frequency may reach 10 THz and higher. However, high characteristic voltages and oscillation frequencies are realized only at temperatures much lower than the critical temperature. In particular, values of V_c above 5 mV are observed for the HTSC junctions at liquid-helium temperatures and lower. For the HTSC junctions on bicrystal substrates, the choice of the substrate material is highly important. The best dc characteristics are obtained for junctions on the strontium titanate substrates, but the high dielectric constant and the substantial losses at high frequencies render them unsuitable for use in the submillimeter wave range. Sapphire substrates proved to possess the most suitable characteristics, and they were used to fabricate the Josephson oscillators. Unlike standard bicrystal substrates with a misorientation in the substrate plane, we used substrates with a crystallographic axis inclined to the substrate plane. Epitaxial YBaCuO films were grown by laser ablation on the substrates whose c axis in the ⟨100⟩ direction was inclined at an angle of 14° + 14°. Films 250 nm thick were deposited on a CeO_2 buffer layer. The critical temperature of the films was $T_c = 89$ K, and the transition width was $\Delta T_c = 1.5$ K. The bicrystal Josephson junctions were from 1.5 to 6 μm wide and, at a temperature of 4.2 K, had the characteristic voltage $V_c \geq 4$ mV. Under an external submillimeter radiation, their I–V characteristics exhibited Shapiro steps at voltages up to 4 mV, which corresponds to frequencies above 2 THz.

3. Bolometer response to changes in temperature and absorbed power. The main bolometer characteristics were measured at a temperature of 260 mK in a cryostat with a closed-cycle He-3 absorption refrigerator. The maximal voltage response to the temperature variations was 1.6 mV/K for a 10-kΩ SIN junction, and the maximal current response was equal to 55 nA/K for a 6-kΩ junction.

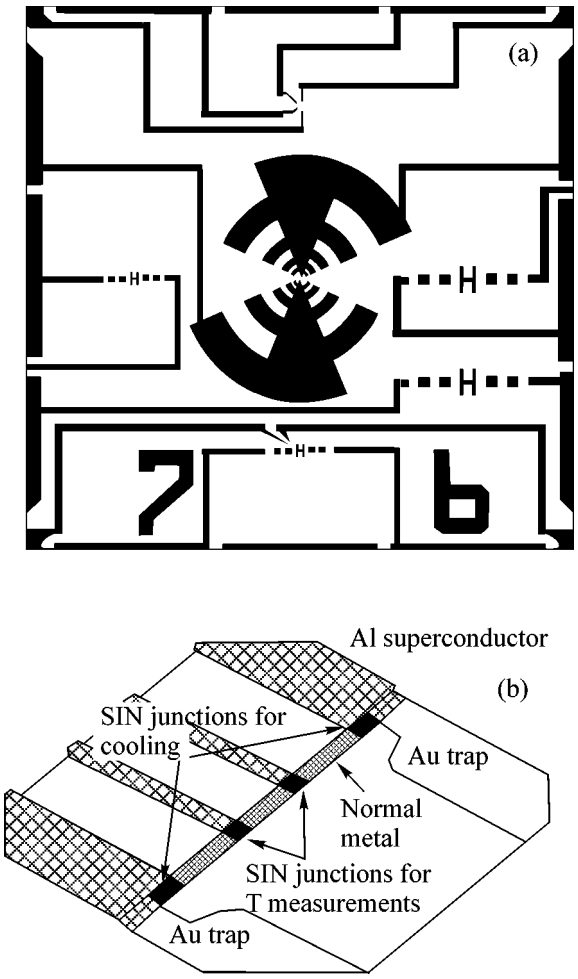

Fig. 1. (a) General view of a substrate with bolometer and (b) atomic-force microscopic image of the bolometer central part.

For structures with four SIN junctions, it was possible to apply power to the inner pair of junctions and measure the response of the outer pair. The measured dependences of the response on the bias voltage are shown in Fig. 2. The maximal voltage response was 4×10^8 V/W for a pair of 70-kΩ junctions, and the maximal current response was 550 A/W for a pair of 10-kΩ junctions. These values correspond to the noise-equivalent power (NEP)

$$\text{NEP} = I_n/S_i \quad \text{or} \quad \text{NEP} = V_n/S_v, \tag{1}$$

where I_n is the current noise, V_n is the voltage noise, $S_i = dI/dP$ is the current response, and $S_v = dV/dP$ is the bolometer voltage response. Setting the noise voltage of our preamplifier equal to 3 nV/Hz$^{1/2}$, we obtain the technical noise-equivalent power:

$$\text{TNEP} = 1.25 \times 10^{-17}\ \text{W/Hz}^{1/2}. \tag{2}$$

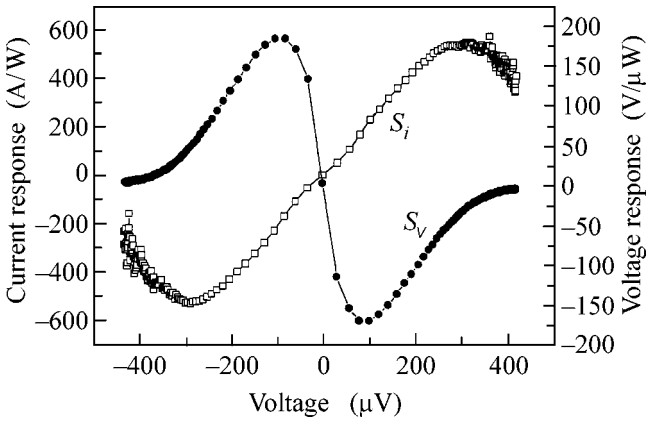

Fig. 2. Current and voltage responses of bolometer with a tunnel junction resistance of 10 kΩ vs. the bias voltage at a temperature of 260 mK.

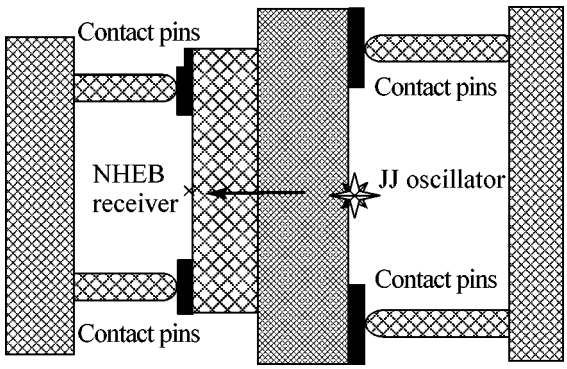

Fig. 3. Schematic diagram of the experiment at 260 mK with the backside of the Josephson oscillator substrate pressed to the backside of the bolometer substrate.

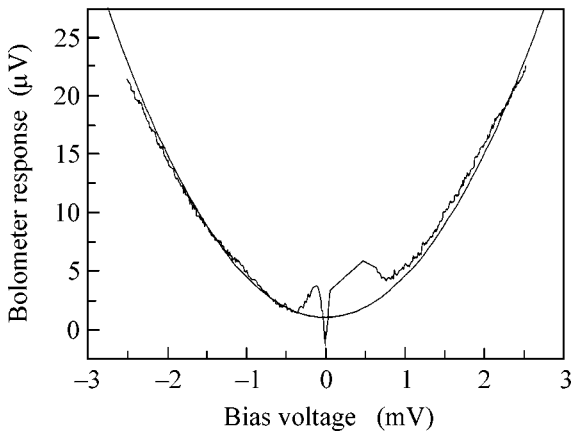

Fig. 4. Bolometer response to the radiation of a Josephson source. The solid parabola corresponds to Joule heating.

Substituting the measured values of the response to changes in temperature and power, we obtain the bolometer heat conductivity

$$G_V = \frac{\partial P}{\partial T} = \frac{\partial V/\partial T}{\partial V/\partial P} = 0.8\times 10^{-11}\ \text{W/K}. \qquad (3)$$

The thermodynamic noise-equivalent power is determined by the expression

$$\text{NEP}_{\text{TD}}^2 = 4kT^2G. \qquad (4)$$

Taking into account that $G = 5\Sigma\nu T^4 = 10^{-11}$ W/K, we obtain $\text{NEP}_{\text{TD}} = 1.4\times 10^{-18}$ W/Hz$^{1/2}$ and, substituting the heat conductivity in a voltage-bias mode, we obtain

$$\text{NEP}_{\text{V}} = 1.3\times 10^{-18}\ \text{W/Hz}^{1/2}. \qquad (5)$$

The use of a SQUID-based low-noise reading device with a current resolution of 50 fA/Hz$^{1/2}$ will allow the noise-equivalent power to be improved by an order of magnitude as compared to the technical noise-equivalent power determined by the noise of a warm transistor amplifier.

4. Measurement of the Josephson junction radiation at 260 mK. In the first series of experiments, the backside of a substrate with the Josephson oscillator was directly attached to the backside of a substrate with the bolometer (Fig. 3), and this assembly was cooled to 260 mK. Since the planar antennas were deposited on the substrates with a dielectric constant higher than 10, the main lobes of their directivity patterns were oriented toward the dielectric and, when the radiating antenna was positioned opposite the receiving antenna, an efficient power transfer occurred from the Josephson junction to the bolometer. The log-periodic antennas of the oscillator and the receiver were identical and rated for a frequency range from 200 GHz to 2 THz.

The dependence of the bolometer response on the voltage applied to the Josephson junction is shown in Fig. 4. By applying a magnetic field, the critical current of the Josephson junction can be suppressed to zero, and then the junction will be a simple current-heated resistor. In this case, depending on the bias on the radiating junction, the bolometer receives thermal radiation from a cold or heated load. The dependence of the response on the bias is found to be parabolic, which corresponds to the Joule heating proportional to the square of applied voltage. This experiment allows one to separate the Josephson radiation component, whose frequency corresponds to the bias voltage, from the broadband thermal component, whose power is proportional to the square of bias voltage. It is significant that, above 1 mV, the Josephson junction is strongly overheated both in the absence and in the presence of magnetic field and its effective electron temperature considerably exceeds the refrigerator equilibrium temperature.

The maximal Josephson radiation power can be estimated as $P_{\text{osc}} = 0.1I_cV_c = 2\times 10^{-9}$ W [7]. In the case of

a log-periodic radiation antenna with a knife-edge pattern and double-dipole reception antenna with a pencil-beam pattern, the mismatch of the directivity patterns takes place and the losses increase by more than 10 dB. The oscillator substrate had five log-periodic antennas on its surface, and the bolometer substrate had two double-dipole antennas and one log-periodic antenna. The oscillator and receiver antennas were never directed toward each other, resulting in the losses of no less than 10 dB. No convergence lenses were placed between the oscillator and receiver, so that the received beams diverged, adding another 10-dB (or greater) loss. The mismatch with antenna, the mismatch between the radiating and receiving beams, the inaccurate alignment of the directions of different antennas, the reflections from the sapphire–silicon boundary, and the difference in polarizations—all this provides a total loss of no less than 30 dB at frequencies on the order of 1 THz. As a result, the power received by the bolometer is less than 10^{-12} W. Setting the response of the bolometer under consideration to $S = 1.1 \times 10^8$ V/W, we find that the maximal voltage response is equal to approximately 1.1×10^{-4} V. In our experiments, the response to the Josephson radiation reached a level of 10 μV. The difference of one order of magnitude may be caused by such factors as nonideal characteristics of the Josephson junction, excess current, and overheating, which reduce the output power. The response to the non-Josephson radiation on the parabolic portion of the response curve may be ascribed to the receipt of the submillimeter and infrared radiation from the matched load integrated in the broadband antenna circuit and radiating into the quasi-optical channel.

If we accept the overheating model for the Josephson junction as a bridge of variable thickness [4], we can estimate the temperature in the middle of the bridge as

$$T_m = \sqrt{T_b^2 + 3\left(\frac{eV}{2\pi k}\right)^2}. \quad (6)$$

From this relation, we obtain an equivalent electron temperature of about 3 K for a Josephson junction bias of 1 mV. Considering that the thermal radiation is scattered within a solid angle of 4π and that the bolometer is placed at a distance of about 1 mm in a dielectric, the value of 5 mK of the effective temperature measured by the bolometer becomes understandable. Since the power is first radiated and then received, it is also necessary to take into account the quantum character of radiation according to the Planck law:

$$P_r = \frac{hf}{e^{hf/kT} - 1} 0.3 f. \quad (7)$$

According to this relation, the maximal radiation occurs at a frequency corresponding to the temperature:

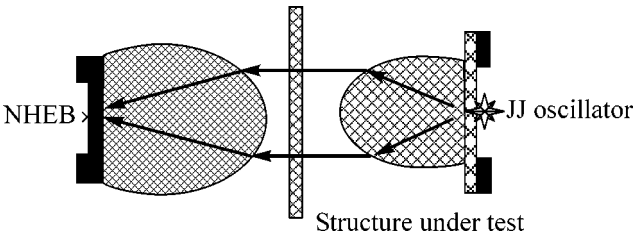

Fig. 5. Schematic diagram of the quasi-optical experiment, where the bolometer was positioned on the flat surface of a hyperhemispherical sapphire lens at 260 mK and the substrate with the Josephson oscillator was placed on a similar silicon lens at 1.8 K. The oscillator and receiver were 3 cm apart, so that the tested object could be placed between them.

$hf \approx kT$. Applying Eq. (7) to Eq. (1) and neglecting the phonon temperature, we arrive at the expression

$$P_{\text{rad}} = \frac{0.6}{4\pi^2}\frac{e^2V^2}{h}, \quad (8)$$

which fits the quadratic dependence observed in the experiment.

5. Irradiation of bolometer by the Josephson junction at 1.8 K. To increase the output power of the Josephson source and the oscillation frequency, it is necessary to increase the characteristic voltage of the Josephson junction, i.e., its critical current. Placing the Josephson junction at the He-4 cooling step, we prevent the bolometer overheating by the dc bias-current power of the Josephson junction. For example, in a junction with a resistance of 10 Ω, a power of 0.2 μW is absorbed at an oscillation frequency of 300 GHz, and this power increases to 2.5 μW at a frequency of 1 THz.

In the quasi-optical configuration (Fig. 5), the bolometer was placed on the flat surface of a hyperhemispherical sapphire lens at a temperature of 260 mK, and the substrate with the Josephson oscillator was placed on a similar silicon lens at a temperature of 1.8 K. The oscillator and the receiver were spaced 3 cm apart.

The topology of the Josephson samples was the same as in the experiments at 260 mK, but the critical current exceeded 0.5–1 mA at 4 K. In the absence of an external magnetic field, the value of I_cR_n exceeded 5 mV. With increasing magnetic field, the critical current oscillated. Under the irradiation by a backward-wave oscillator, the Shapiro steps were observed up to 4 mV. The experimental curves are shown in Fig. 6. Figure 6a represents the response of a bolometer with a double-dipole antenna rated for a central frequency of 300 GHz and the response of a bolometer with a log-periodic broadband antenna in the range 0.2–2 THz. Figure 6b shows the response of a bolometer with a double-dipole antenna for two values of magnetic field, i.e., for the higher (upper curve) and lower (lower curve) values of critical current and characteristic volt-

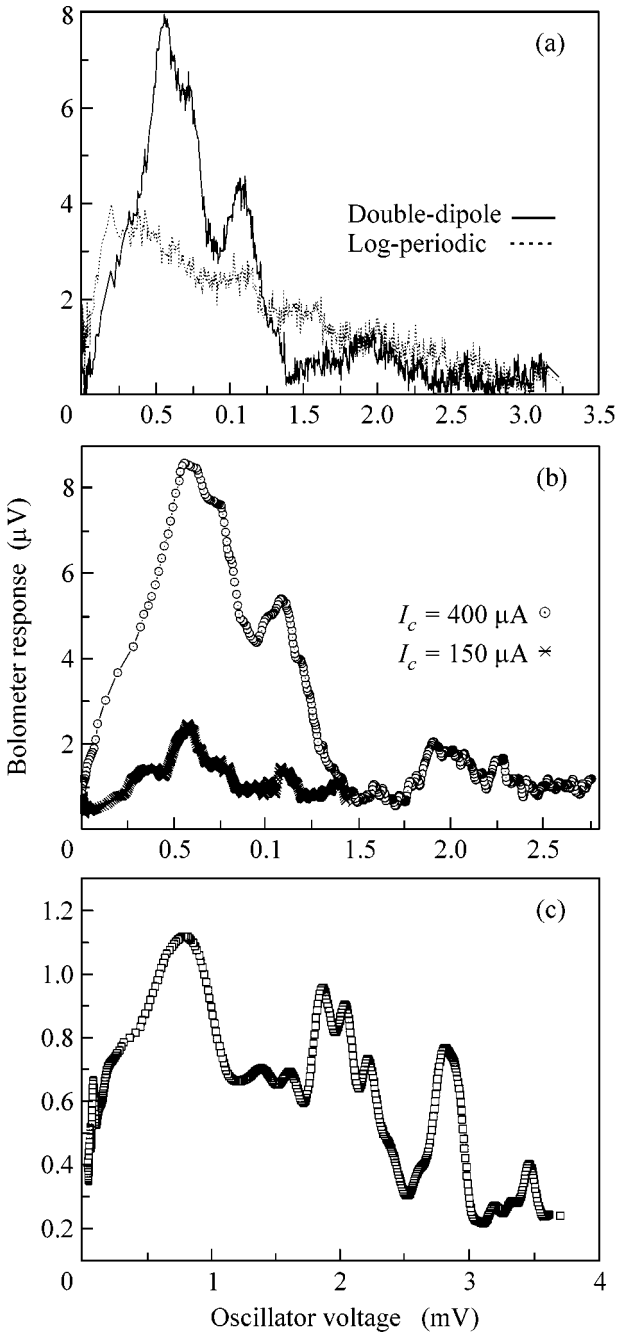

Fig. 6. (a) Responses measured by a bolometer with a double-dipole antenna (upper curve) and a bolometer with a log-periodic antenna (lower curve). (b) Response of a bolometer with a double-dipole antenna for two values of magnetic field and critical currents of 400 (upper curve) and 150 μA (lower curve). (c) Response measured at high bias voltages without magnetic field. The last maximum corresponds to a frequency of 1.7 THz.

age. The response corresponding to the highest frequency (1.7 THz) is shown in Fig. 6c. The same curve exhibits the third and fifth harmonics of the antenna fundamental mode.

6. Discussion. A simple analytic expression for the voltage response of bolometer [9] gives a rough estimate of the practically attainable power response at a temperature of 260 mK:

$$S_V^{\max} = \frac{2k_b}{e\Sigma\nu T_e^4} = 10^8 \text{ V/W}.$$

A more accurate calculation, according to [9], yields a value of 4×10^8 V/W, which coincides with the experimental data. With allowance made for the bolometer noise at the operating point and the amplifier noise V_N = 6 nV/Hz$^{1/2}$ in a current bias mode, the noise-equivalent power is

$$\text{NEP}_\text{V} = V_N/S_V^{\max} = 1.5 \times 10^{-17} \text{ W/Hz}^{1/2}.$$

Let us also estimate the characteristic values for the voltage bias mode with electron cooling. The main heat flow occurs from hot phonons to electrons that are subjected to electron cooling:

$$P_{Ph-e} = \Sigma\nu T_{Ph}^5 = 0.5 \text{ pW}.$$

To remove this power from the electron system, it is necessary to apply cooling current

$$I_c = \frac{eP_{Ph-e}}{k_b T} = 2.2 \times 10^{-8} \text{ A}.$$

This current gives rise to a shot noise. Taking the theoretical value of the current response $S_I = e/2k_bT = 6 \times 10^3$ A/W, we obtain the noise-equivalent power

$$\text{NEP}_\text{I} = \sqrt{4k_bT_e\Sigma\nu T_{Ph}^5} = 1.3 \times 10^{-17} \text{ W/Hz}^{1/2}. \quad (9)$$

This value is smaller than the measured value of 5×10^{-17}. This can be explained by the fact that the current response of high-resistance SIN junctions is weaker than the theoretical value obtained for an optimal resistance of 1 kΩ.

The voltage response has been measured for a SINIS bolometer at 260 mK to give 4×10^8 V/W. The noise-equivalent power limited by the bolometer and amplifier noise is 1.5×10^{-17} W/Hz$^{1/2}$. The measurements of the radiation from an HTSC Josephson junction have shown that, at bias voltages on the order of 1 mV, the junction is overheated, and its effective temperature exceeds 3 K for a substrate temperature of 260 mK. The use of HTSC junctions at low temperatures is advantageous, because these junctions allow one to obtain high values of characteristic voltage I_cR_n and increase the radiation frequency at least to 1.7 THz. A combination of a Josephson terahertz oscillator with a high-sensitivity SINIS bolometer makes it possible to realize a compact cryogenic terahertz network analyzer with a frequency resolution on the order of several gigahertz.

This work was supported by the VR and STINT foundations (Sweden) and by the INTAS (project nos. 01-686 and 00-384).

REFERENCES

1. L. Kuzmin, Physica B (Amsterdam) **284–288**, 2129 (2000).
2. M. Tarasov, M. Fominskiĭ, A. Kalabukhov, and L. Kuz'min, Pis'ma Zh. Éksp. Teor. Fiz. **76**, 588 (2002) [JETP Lett. **76**, 507 (2002)].
3. L. Kuzmin, I. Devyatov, and D. Golubev, Proc. SPIE **3465**, 193 (1998).
4. M. Nahum, T. M. Eiles, and J. M. Martinis, Appl. Phys. Lett. **65**, 3123 (1994).
5. M. Leivo, J. Pecola, and D. Averin, Appl. Phys. Lett. **68**, 1996 (1996).
6. M. Tarasov, L. Kuz'min, M. Fominskiĭ, *et al.*, Pis'ma Zh. Éksp. Teor. Fiz. **78**, 1228 (2003) [JETP Lett. **78**, 714 (2003)].
7. K. K. Likharev and B. T. Ul'rikh, *Systems with the Josephson Contacts* (Mosk. Gos. Univ., Moscow, 1978).
8. M. Tinkham, M. Octavio, and W. J. Skocpol, J. Appl. Phys. **48**, 1311 (1977).
9. D. Golubev and L. Kuzmin, J. Appl. Phys. **89**, 6464 (2001).

Translated by E. Golyamina

JETP Letters, Vol. 79, No. 6, 2004, pp. 304–307. Translated from Pis'ma v Zhurnal Éksperimental'noĭ i Teoreticheskoĭ Fiziki, Vol. 79, No. 6, 2004, pp. 362–366.

Dissipation of Ripplon Flow at the Surface of Superfluid ^{4}He

A. I. Safonov*, S. S. Demukh, and A. A. Kharitonov

Russian Research Centre Kurchatov Institute, pl. Kurchatova 1, Moscow, 123182 Russia

**e-mail: safonov@isssph.kiae.ru*

Received February 18, 2004

Within the framework of quantum hydrodynamics of a superfluid helium surface, the momentum relaxation rate caused by the annihilation of two ripplons with phonon creation, inelastic phonon scattering with ripplon annihilation, and in the case of helium films one-particle ripplon scattering from the surface-level inhomogeneities introduced by the substrate roughness (new relaxation mechanism) was obtained for a ripplon gas at $T \lesssim 0.25$ K. The contribution from the inelastic phonon scattering is negligible at these temperatures. For a film at $T \leq 0.15$ K, one-particle scattering dominates, leading to a temperature dependence of the form $K \propto T^{5/3}$ for the convective thermal conductance. At higher temperatures, phonon creation with annihilation of two ripplons is the dominant mechanism, giving $K \propto T^{-3}$. These results are in quantitative agreement with the available experimental data.

PACS numbers: 67.40.Pm; 67.40.Hf; 68.03.Kn

The hydrodynamical flow drag of a gas of elementary excitations (ripplons) [1] at the surface of superfluid ^{4}He determines the heat transfer in helium films at $T \lesssim 0.2$ K [2, 3], the possibility of and the conditions for the observation of the second surface sound [4], and also plays an important role in the experiments with two-dimensional atomic hydrogen (2D H↓) at the helium surface [5, 6]. In this work, the phonon-induced ripplon-flow decay at the surface of a bulk liquid is calculated and the flow dissipation mechanism is suggested for a helium film covering rough substrate.

The ripplon gas flow along the helium surface separately from bulk liquid was considered theoretically by Andreev and Kompaneets in [7] and observed experimentally by Mantz, Edwards, and Nayak in [2, 3]. Originally, the main role in the ripplon-flow stagnation was ascribed to the creation of a long-wavelength ripplon with annihilation of two short-wavelength ripplons [2, 8], followed by a rapid decay of the long-wavelength ripplon, whose velocity field penetrates across the whole film width. Later on, it was recognized, however, that both the theoretical probability of this process [9] and the actual decay of acoustic ripplons [10] are quite insignificant. It was established theoretically that the inelastic phonon (P) scattering at the surface with the creation of a ripplon (R) [8, 9] or the annihilation of two ripplons with phonon creation [11] are the main mechanisms that are responsible for the interaction of ripplon subsystem with bulk helium at temperatures considered. Next, Reynolds, Setija, and Shlyapnikov [11] showed that the energy transfer from the ripplon to the phonon subsystem is mainly governed by the second process.

Following the reasoning exactly as in [11], we calculate the momentum-transfer rate from the ripplon to the phonon subsystem with the creation of a phonon with wavevector ($\mathbf{q}$, k), where $\mathbf{q}$ and k are the components, respectively, along and perpendicular to the surface, and with the annihilation of two ripplons with wavevectors $\mathbf{q}'$ and $\mathbf{q}''$. Denote the ripplon and phonon temperatures as T_R and T_P. The ripplon frequency and wavevector are related to each other by the well-known expression $\omega_{q'}^2 = q'^3\alpha/\rho$ [1], where $\alpha = 0.378$ dyne/cm and $\rho = 0.145$ g/cm^3 are, respectively, the surface tension and the density of liquid ^{4}He at $T = 0$. Similarly, one has for phonons $\omega_{qk} = c\sqrt{q^2 + k^2}$, where $c = 238$ m/s is the sound velocity in helium. Due to the energy and momentum conservation laws, $q \ll q'$ and, hence, $\mathbf{q}'' \approx -\mathbf{q}'$. According to [11], the matrix element for the R + R ⟷ P transition is

$$\langle \mathbf{q}k|H|\mathbf{q}'', \mathbf{q}'\rangle \approx \left(\frac{\hbar^3 c^2}{V\rho\omega_{qk}}\right)^{1/2} q'k\delta_{\mathbf{q},\,\mathbf{q}'+\mathbf{q}''}, \qquad (1)$$

where V is the liquid volume. The momentum transfer rate to phonons is given by the expression presented in [11] for the heat transfer rate:

$$\Pi_{\mathrm{R}+\mathrm{R}\leftrightarrow\mathrm{P}} = V\frac{2\pi}{\hbar^2}\int \hbar\mathbf{q}|\langle \mathbf{q}k|H|\mathbf{q}'', \mathbf{q}'\rangle|^2$$

$$\times [N_{q'}N_{q''}(1 + n'_{qk}) - n'_{qk}(1 + N_{q'})(1 + N_{q''})] \qquad (2)$$

$$\times \delta(\omega_{q'} + \omega_{q''} - \omega_{qk})\frac{d^2q'd^2qdk}{(2\pi)^5},$$

where $N_{q'}(T_\mathrm{R})$, $N_{q''}(T_\mathrm{R})$, and $n'_{qk}(T_\mathrm{P})$ are the equilibrium occupation numbers for, respectively, ripplons and phonons in the reference system associated with

ripplons. The integration over q' goes over a half of the momentum space, lest the same pairs ($\mathbf{q}'$, $\mathbf{q}''$) of ripplons be taken twice.

Let ripplons move relative to the bulk liquid with a velocity $\mathbf{u}$ much lower than the sound velocity. Then, the occupation numbers in the reference system associated with ripplons are $n'_{qk} \equiv n'(\omega_{qk}) = n(\omega_{qk} - \mathbf{uq})$, where n's are the occupation numbers in a fixed coordinate system. By expanding n' in powers of $\mathbf{uq}$ and retaining only the linear term (because $|\mathbf{uq}| \ll cq \leq \omega_{qk}$), we obtain $n'_{qk} \approx n_{qk} - \mathbf{uq}(dn_{qk}/d\omega_{qk})$. Due to the symmetry, all terms proportional to $\mathbf{q}$ in Eq. (2) turn to zero upon the integration, and $\mathbf{q}(\mathbf{uq})$ can be replaced by $\mathbf{u}q^2/2$. In addition, $\omega_{q'} \approx \omega_{q''} \approx \frac{1}{2}\omega_{qk}$ and $N_{q'} \approx N_{q''}$. The subsequent calculation yields

$$\Pi_{\mathrm{R+R\leftrightarrow P}} = \frac{16}{45\pi^2}\frac{\mathbf{u}}{c}\left(\frac{\rho}{\alpha}\right)^{4/3}\frac{\hbar^2}{\rho c^4}\left(\frac{T_\mathrm{P}}{\hbar}\right)^{20/3} \times \int_0^\infty x^{20/3}dx\left[\frac{e^{2x}}{(e^{2x}-1)}\left(\frac{e^{\beta x}+1}{e^{\beta x}-1}\right)\right]. \quad (3)$$

In this expression, $\beta = T_\mathrm{P}/T_\mathrm{R}$. The substitution of numerical values gives

$$\Pi_{\mathrm{R+R\leftrightarrow P}} = \left(1.33\times 10^{-4}\frac{\mathrm{g}}{\mathrm{cm}^3\mathrm{K}^{20/3}}\right)\mathbf{u}T_\mathrm{P}^{20/3}F(\beta), \quad (4)$$

where $F(\beta)$ stands for the integral in Eq. (3). For small β, i.e., for $T_\mathrm{P} \ll T_\mathrm{R}$, the evaluation of this integral gives $F(\beta) \approx 7.91/\beta$, and it becomes constant $F \approx 12.9$ in the opposite limit $\beta \gg 1$. If the temperatures of both subsystems coincide, the integral is $F(1) \approx 14.3$.

Let us now turn to the inelastic phonon scattering $\mathrm{P}(\mathbf{q}k) \longleftrightarrow \mathrm{P}(\mathbf{q}'k') + \mathrm{R}(\mathbf{Q})$. One can readily see from the kinematic considerations [8] that the ripplon frequency ω_Q is small compared to the phonon frequencies ω_{qk} and $\omega_{q'k'}$, whereas the vectors q, q', and Q are, generally speaking, comparable. Consequently, $\hbar\omega_Q \ll T_\mathrm{P}$, because the main contribution to the momentum transfer comes, clearly, from phonons with energies $\lesssim T_\mathrm{P}$ (the phonon and ripplon temperatures are assumed to be comparable). According to the experimentally confirmed [10] calculations of Roche, Roder, and Williams [9], the reciprocal decay time caused by the inelastic phonon scattering is equal for acoustic ripplons to

$$\frac{1}{\tau_Q} \approx \frac{\pi^2}{60}\frac{\hbar Q}{\rho}\left(\frac{T_\mathrm{P}}{\hbar c}\right)^4. \quad (5)$$

Similarly to Eq. (2), the momentum transfer rate can be estimated by the integral

$$\Pi_{\mathrm{P}\leftrightarrow\mathrm{P+R}} = \int\frac{\hbar\mathbf{Q}}{\tau_Q}N'_Q\frac{d^2Q}{(2\pi)^2} \quad (6)$$

with the shifted ripplon distribution function $N'(\omega_Q) = N(\omega_Q - \mathbf{uQ}) \approx N_Q + \mathbf{uQ}(T/\hbar\omega_Q^2)$ and the integration going to $Q \sim q_T = T_\mathrm{P}/\hbar c$, where q_T is the wavevector of a thermal phonon. This gives

$$\Pi_{\mathrm{P}\leftrightarrow\mathrm{P+R}} \sim \frac{\pi}{480}\frac{\mathbf{u}}{c}\frac{\hbar c}{\alpha}\left(\frac{T_\mathrm{P}}{\hbar c}\right)^6 T_\mathrm{R}, \quad (7)$$

i.e.,

$$\Pi_{\mathrm{P}\leftrightarrow\mathrm{P+R}} \sim \left(7.1\times 10^{-5}\frac{\mathrm{g}}{\mathrm{cm}^3\mathrm{K}^7}\right)\mathbf{u}T_\mathrm{P}^6T_\mathrm{R}, \quad (8)$$

which is several orders of magnitude smaller than the value obtained for the $\mathrm{R+R}\longleftrightarrow\mathrm{P}$ process at temperatures $T \lesssim 0.2$ K. Thus, the characteristic time of momentum transfer from the ripplon to the phonon subsystem is, evidently,

$$\tau_\mathrm{R} \approx \frac{\rho_\mathrm{R}\mathbf{u}}{\mathbf{\Pi}_{\mathrm{R+R\leftrightarrow P}}} \approx \frac{1.26\times 10^{-7}\mathrm{sK}^5}{T_\mathrm{P}^5\beta^{5/3}F(\beta)}, \quad (9)$$

where $\rho_\mathrm{R} = 1.67\times 10^{-10}T_\mathrm{R}^{5/3}$ (g/cm^2) K$^{-5/3}$ is the ripplon mass density.

The convective thermal conductance

$$K_\mathrm{R} = TS_\mathrm{R}^2\frac{\tau_\mathrm{R}}{\rho_\mathrm{R}}, \quad (10)$$

due to the heat transfer by the ripplon hydrodynamical flow [2], where $S_\mathrm{R} = 1.52\times 10^{-2}T^{4/3}$ erg cm^{-2} K$^{-7/3}$ is the ripplon gas entropy, is one of the possible experimentally measured quantities. It follows that, if the ripplon stagnation is controlled by the $\mathrm{R+R}\longleftrightarrow\mathrm{P}$ process, the value of K_R must decrease as T^{-3} with increasing temperature. However, the experiments of Mantz, Edwards, and Nayak [2] showed a cardinally different behavior (Fig. 1): the thermal conductance increased with temperature up to $T \approx 0.15$ K, whereupon it became saturated and even slightly decreased. Such a distinction can be explained by the occurrence of a different and a more efficient ripplon-stagnation mechanism in helium films. It follows from the experimentally observed temperature dependence of thermal conductance that the characteristic ripplon-momentum relaxation time at low temperatures depends weakly on temperature. This allows one to disregard multiparticle processes such as direct ripplon interaction with the substrate phonons and restrict oneself to a search for the mechanisms determining the finite lifetime of an individual ripplon.

We assume that the ripplon decay is due to the scattering from the film surface inhomogeneities introduced by the substrate roughness (Fig. 2a). Since the ripplon propagation is unrelated to the surface orientation, only the variable surface curvature $K(\mathbf{r})$ can be the cause of scattering. The effective potential for ripplon scattering (Fig. 2b) can easily be found from the dimen-

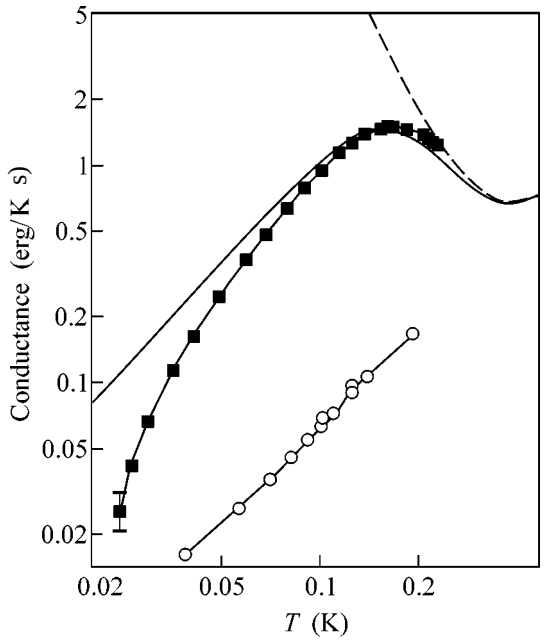

Fig. 1. The convective thermal conductance of ripplons at the surface of ^{4}He film: (solid curve) according to Eq. (16) with $H = 6$ cm and $l = 2.9$ μm, and (■) experimental results of Mantz *et al.* [2]. The calculated dependence (light dots) takes into account the experimentally measured thermal conductance of substrate. The dashed curve shows the ripplon thermal conductance restricted only to the interaction with helium phonons.

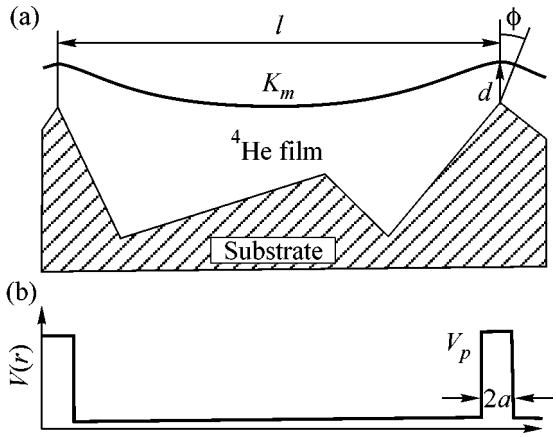

Fig. 2. (a) The profile of a substrate surface and a coating helium film. (b) Effective potential produced by the surface curvature and leading to the ripplon scattering.

sional considerations: $V(\mathbf{r}) \sim \hbar(\alpha/\rho)^{1/2}|K(\mathbf{r})|^{3/2}$. Due to the capillary effect, a film covering a rough surface fills the deepenings between the substrate peaks to form menisci with curvature $K_m = \rho g H/\alpha \sim 10^3$ cm^{-1}, where $H \sim 1$ cm is the height above the level of bulk liquid. At the peaks, the curvature coincides, in the order of magnitude, with the reciprocal film thickness, $K_p \simeq 2/d \simeq 6 \times 10^5 H^{1/3}$ cm^{-1} (the height H is in centimeters). The number of peaks per unit surface area is equal to $\sim 1/l^2$, where l is the roughness scale. Since the constant component of effective potential does not induce scattering and $K_p \gg K_m$, the effective potential $V(\mathbf{r})$ can be replaced by the zero value everywhere except for the vicinities of peaks, where, due to the relation between the potential and the curvature, it is $V_p \sim \hbar(\alpha/\rho)^{1/2} d^{-3/2}$. The vicinity size a is determined by the surface slope $\phi = K_m l/4$ near the peak and is $a = \phi d \simeq 10^{-7}$ cm for $l = 1$ μm. Thus, the scattering centers are rather widely spaced, so that each of them can be considered separately.

Note that K_p is small compared to the wavevector $q_T = (\rho/\alpha)^{1/3}(T/\hbar)^{2/3} \sim 3 \times 10^6$ cm^{-1} of the typical ripplon, whereas $q_T a \simeq 0.3$. One can, therefore, use the Born approximation for slow particles, which, as is known, gives the isotropic scattering. The scattering cross section of a ripplon with wavevector $\mathbf{q}$ can be obtained from the standard expression [12] for the two-dimensional case by the substitution of the ripplon effective mass according to the definition $1/m = \partial E_q/\partial(q^2) = \frac{3}{4}\hbar(\alpha/\rho)^{1/2} q^{-1/2}$. The result is independent of q:

$$\sigma \simeq \frac{4}{9\hbar^2}\left(\frac{\rho}{\alpha}\right)\left|\int V(\mathbf{r}) d^2 r\right|^2 \simeq \frac{4\pi^2 V_p^2 a^4}{9\hbar^2}\left(\frac{\rho}{\alpha}\right), \qquad (11)$$

or, using the expressions for V_p and a,

$$\sigma \sim \frac{32\phi^4\pi^2}{9} d. \qquad (12)$$

The ripplon mean free path is, as usual, $\lambda = l^2/\sigma$, and the reciprocal relaxation time τ_q of the momentum projection onto the initial direction is found from the relation $\tau_q \omega_q = q\lambda$.

The momentum transfer rate from ripplons to the substrate is calculated by analogy with Eq. (6):

$$\Pi_V = \frac{1}{2}\int_0^\infty \frac{d^2 q}{(2\pi)^2}\frac{\hbar \mathbf{u} q^2}{\tau_q}\left|\frac{dN_\omega}{d\omega_q}\right|. \qquad (13)$$

The integration with respect to q and the substitution of ϕ give

$$\Pi_V \sim 0.14\frac{T_R^2 \mathbf{u}}{\hbar}\left(\frac{\rho}{\alpha}\right)^5 (gH)^4 l^2 d. \qquad (14)$$

Accordingly, the characteristic time of momentum transfer from ripplons to the substrate is

$$\tau_R \approx \frac{\rho_R \mathbf{u}}{\Pi_V} \approx \frac{8 \times 10^{-15}\ \mathrm{K}^{1/3}\ \mathrm{cm}^7\ \mathrm{s}}{T_R^{1/3} H^4 l^2 d}. \qquad (15)$$

Thus, the thermal conductance at low temperatures is proportional to $T^{5/3}$, in full agreement with the experimentally observed dependence.

For several simultaneously acting mechanisms, the momentum relaxation rates add up. Hence, the final expression for the film thermal conductance at $T_P = T_R = T$ has the form

$$K \approx \left(83T^3 + \frac{9\times 10^7}{T^{5/3}} H^4 l^2 d\right)^{-1} \text{ [erg/s K]}. \qquad (16)$$

In Eq. (16), the temperature is in K and the roughness scale l is in cm. The temperature dependence of K_R for $H = 6$ cm and $l = 2.9$ μm is shown in Fig. 1 by the solid curve. The agreement with the experiment [2] (■) looks rather conclusive, the more so as all calculations were carried out using the *ab initio* values, while the only fitting parameter—substrate roughness scale l—seems to be quite reliable from the viewpoint of experimental conditions. In the calculations, the experimentally measured thermal conductance of the substrate (mylar film coated with a layer of solid neon) was taken into account. For comparison, the ripplon convective thermal conductance restricted only to the interaction with liquid phonons (R + R ⟷ P process), as is the case for the surface of bulk helium, is shown in Fig. 1 by the dashed curve.

As is known, the equilibrium film thickness d is related to the height above the level of bulk liquid by $d \approx 3 \times 10^{-6} H^{-1/3}$, where both quantities are expressed in cm. For this reason, the dependence of K on the film thickness observed by Mantz *et al.* in [3] can be explained qualitatively by formally replacing the height H by $(3 \times 10^{-6}/d)^3$ in Eq. (16). It should also be noted that the fact that the momentum relaxation time depends on the substrate roughness scale and on the film height above the bulk liquid can be the reason why the times observed in experiments with two-dimensional atomic hydrogen [6] were much shorter than in the experiments of Mantz *et al.* [2, 3].

In conclusion, let us discuss the validity of using the concept of ripplon temperature. The point is what is the ratio between the rate of establishing equilibrium in the ripplon system and the rate of equilibrium breaking due to the interaction with phonons (one-particle elastic ripplon scattering by the surface inhomogeneities does not affect the distribution function). The characteristic heat transfer time from ripplons to phonons is mainly determined by the R + R ⟷ P process and can be estimated as $\tau_{rp} \sim R_{rp} C_R = 3 \times 10^{-10} T^{-13/3}$ K$^{13/3}$ s, where $C_R = 1.52 \times 10^{-2} T^{4/3}$ erg K$^{-7/3}$ cm^{-2} is the ripplon heat capacity (coinciding with the ripplon entropy) and $R_{rp} = 1.8 \times 10^{-8} T^{-17/3}$ K$^{20/3}$ cm^2/erg is the thermal resistance between the ripplon and phonon subsystems [11]. One can readily see that, in the absence of an external heat inflow and efficient relaxation mechanisms in the ripplon system, the indicated process leads to the ripplon thermal distribution with temperature equal to the phonon temperature (the phonon system is assumed to be in equilibrium). Such a situation is realized, e.g., when measuring the temperature dependence of surface tension in pure ^{4}He [13] and in the measurements of thermal conductance of helium films [2]. As to the experiments with atomic hydrogen [5], the time of establishing thermal equilibrium in a two-dimensional system is determined by the ripplon scattering from the H atoms adsorbed at the helium surface [14]. For a characteristic density of ~10^{12} cm^{-2} of these atoms and the temperature $T \lesssim 100$ mK, this time is $\tau_2 \sim 60$ ns, which is two orders of magnitude shorter than the heat transfer time from ripplons to phonons. Thus, a two-dimensional system is also in thermal equilibrium in this case, but its temperature can be different from the phonon temperature.

We are grateful to L.A. Maksimov for helpful discussions and to I.I. Lukashevich for support. This work was supported by the Russian Foundation for Basic Research (project no. 02-02-16652a) and INTAS (grant no. 2001-0552).

REFERENCES

1. K. R. Atkins, Can. J. Phys. **31**, 1165 (1953).
2. I. B. Mantz, D. O. Edwards, and V. U. Nayak, Phys. Rev. Lett. **44**, 663 (1980); **44**, 1094(E) (1980).
3. I. B. Mantz, D. O. Edwards, and V. U. Nayak, J. Phys. Colloq. **39**, C6-300 (1978).
4. W. M. Saslow and A. A. Kumar, Phys. Rev. B **30**, 6402 (1984).
5. S. A. Vasilyev, J. Järvinen, A. I. Safonov, and S. Jaakkola, Phys. Rev. A **69**, 023610 (2004).
6. In recent experiments (with the participation of the authors of this work) on the thermal compression of 2D H↓, a gas flow of H atoms along the surface of helium film was observed. The momentum transfer time from the hydrogen subsystem to ripplons and from ripplons to the substrate are the key words in the description of this flow. The material is prepared to publication. s12. Theoretical Physics. III. Quantum Mechanics.
7. A. F. Andreev and D. A. Kompaneets, Zh. Éksp. Teor. Fiz. **61**, 2459 (1972) [Sov. Phys. JETP **34**, 1316 (1972)].
8. W. F. Saam, Phys. Rev. A **8**, 1918 (1973).
9. P. Roche, M. Roger, and F. I. B. Williams, Phys. Rev. B **53**, 2225 (1996).
10. P. Roche, G. Deville, K. O. Keshishev, *et al.*, Phys. Rev. Lett. **75**, 3316 (1995).
11. M. W. Reynolds, I. D. Setija, and G. V. Shlyapnikov, Phys. Rev. B **46**, 575 (1992).
12. L. D. Landau and E. M. Lifshitz, *Course of Theoretical Physics*, Vol. 3: *Quantum Mechanics: Non-Relativistic Theory*, 4th ed. (Nauka, Moscow, 1989; Pergamon, New York, 1977).
13. D. O. Edwards and W. F. Saam, in *Progress in Low Temperature Physics*, Ed. by D. F. Brewer (North-Holland, Amsterdam, 1978), Vol. 7A, p. 283.
14. D. S. Zimmerman and A. J. Berlinsky, Can. J. Phys. **61**, 508 (1983).

Translated by V. Sakun

JETP Letters, Vol. 79, No. 6, 2004, p. 308.

Erratum: "Structural Transformations in Liquid, Crystalline and Glassy B_2O_3 under High Pressure" [JETP Lett. 78 (6), 393–397 (2003)]

V. V. Brazhkin, Y. Katayama, Y. Inamura, M. V. Kondrin, A. G. Lyapin, S. V. Popova, and R. N. Voloshin

PACS numbers: 64.70.Kb; 62.50.+p; 61.43.-j; 61.50.Ks; 99.10.Cd

The study of the chemical composition of borate glasses obtained in graphite ampoules under pressures of 3–7 GPa and at temperatures above 1700 K have shown the presence of a considerable (5–10 at. %) amount of calcium that enters the glass, most likely, from the pressure-transmitting medium. As a result, the physical properties and structural characteristics that were initially assigned to boron oxide glasses with oxygen nonstoichiometry (6th section in the article) relate in reality to triple glasses with a high calcium content.

0021-3640/04/7906-0308$26.00